A Search for Particles with Magnetic Charge Produced in e^+e^- Annihilations at $\sqrt{s} = 35$ GeV

Julian Shulman
Imperial College, London

A thesis submitted for the degree of
Doctor of Philosophy
at the University of London

August 1988

In loving memory of my parents

EVELYN

26 July 1928 - 24 January 1979

and

MAURICE

18 December 1924 - 16 February 1988

A Search for Particles with Magnetic Charge Produced in e^+e^- Annihilations at $\sqrt{s} = 35$ GeV

Julian Shulman
Imperial College, London

Abstract

A search has been made for magnetically charged particles produced in e^+e^- annihilations [1]. Using the hit information in z from the drift chamber of the TASSO detector, a search was made for tracks curving in the $s - z$ plane in two prong events. The curvature of these tracks is a possible indication of particles being accelerated along the flux lines of the 0.5 Tesla solenoid magnetic field of TASSO. No events of a nature that would uniquely identify an $e^+e^- \rightarrow M\overline{M}$ event were found, but cross-section limits were calculated for a mass range up to 17 GeV/c^2 and a magnetic charge range of $g = 10e$ to $g = 70e$ from the 110 pb^{-1} of data taken at a centre of mass energy of 35 GeV during 1986.

The multi-pulse performance of a test cell was also investigated, with regards to the spatial and dE/dx resolutions. The test cell was a representation of a single cell from the Central Track Detector of the future detector ZEUS on the $e^{\mp}p$ ring HERA. It was found that a two-pulse resolution of 2.15 mm was possible. It was also found that there was a negligible effect of the second pulse upon the first for pulse separations greater than 3.75 mm. Any effect of the first pulse upon the second was found to become negligible for pulse separations greater than 5.25 mm. The spatial resolutions were 60% worse than the single pulse resolutions for the worst affected first pulses and only 15% worse for the worst affected second pulses. dE/dx resolutions could be kept below 7% for all separations after corrections to the pulse sizes.

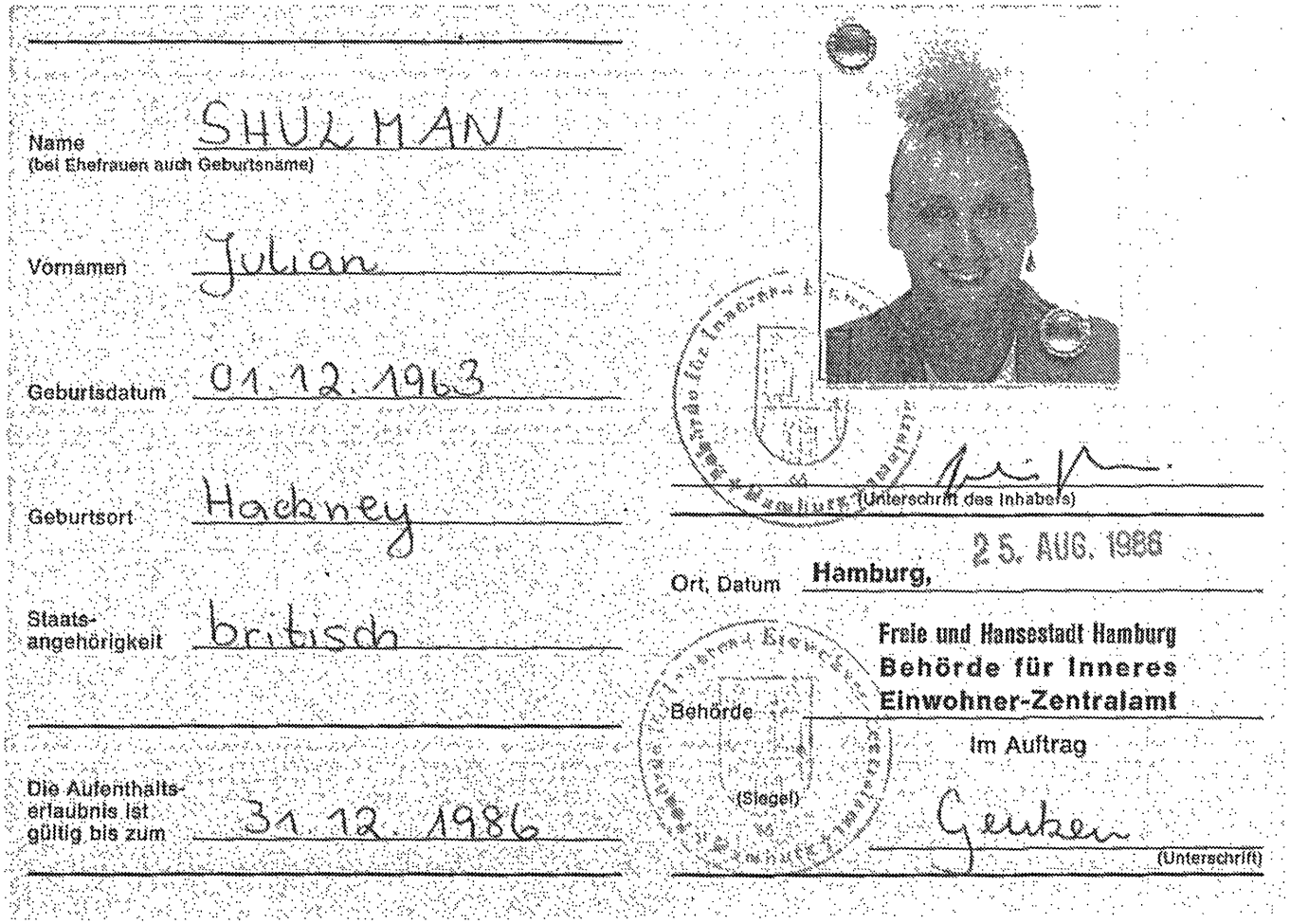


Figure .1: *Ever picked up a thesis and wondered what the author looked like at the time? Well...*

Acknowledgements

Thanks are owed to a great many people for the enjoyment I have had over the three years of my Ph.D., from both within and outside of physics.

I am most grateful to my supervisor, John Hassard, for his guidance, encouragement and enthusiasm.
I would like to express my thanks to the Imperial College High Energy Physics group with whom it has been a pleasure to work, and to Prof. David Binnie for allowing me the opportunity in the first place.
Thanks must also go to all my colleagues and friends out at DESY, not just within TASSO, but also JADE, CELLO, MARK J and ARGUS.
I would also like to thank David Saxon and Slawek Tkaczyk for their help and guidance with the ZEUS work.
I would like to thank Ann Heinson for reading through the thesis and spotting all (well I hope all!) of my spelling and grammatical errors.
Special thanks must go to my physics teacher at school, Walter Painz, who laid the foundations to this work, by his teaching of the 'O' and 'A' levels to me.
This work comes courtesy of the Great British taxpayer, via the Science and Engineering Research Council.

Away from physics I would like to thank Meike, Simone and Ulrike for taking my mind off physics whilst in Hamburg, and Cardiacs for taking my mind off everything!
I am grateful to Natalie for helping me get over my father's death and getting me back on my feet and to Delyth, a close and valued friend for the past four years.

This thesis is dedicated to my father, who died just as I had started writing up this thesis, and without whom nothing would have been possible in the first place.

Contents

I A Search For Particles With Magnetic Charge Produced in e^+e^- Annihilation at $\sqrt{s} = 35$ GeV 1

1 Introduction 3

1.1 In the Beginning... 3

1.2 Searches for Magnetically Charged Particles 6

1.3 The Search in TASSO 7

2 The Experimental Environment 11

2.1 PETRA 11

2.2 TASSO 16

2.2.1 The Vertex Detector (VXD) 16

2.2.2 The Cylindrical Proportional Chamber (CPC) 19

2.2.3 The Drift Chamber (DC) 19

2.2.4 The Inner Time of Flight Counters (ITOFs) 21

2.2.5 The Magnet Coil 22

2.3 Data Acquisition and Reduction 23

2.3.1 The Trigger 23

2.3.2 Data Acquisition 24

2.3.3 Data Reduction 26

3 Simulating Magnetically Charged Particles 29

3.1 The MONSTER Monte Carlo 29

3.2 Stepping the Particles 31

3.3 Matter Interactions of Monopoles 32

3.3.1 Ionization 32
3.3.2 Multiple Scattering 33
3.3.3 Bremsstrahlung 36
3.4 Optimizing the Stepping Routine 37
3.4.1 Smearing of dE/dx losses 37
3.5 Simulating the Detector Materials 40
3.6 Tuning the Monte Carlo to the 1986 Data 44
3.6.1 DC Sense Wire Residual Tuning 44
3.6.2 DC Sense Wire Efficiency Tuning 46
3.6.3 Event Vertex Tuning 48

4 Track Finding of Particles in Magnetic Fields 49
4.1 Motion of Particles Influenced by a Magnetic Field 49
4.1.1 Motion of a Particle with Electric Charge 50
4.1.2 Motion of a Non-Relativistic Particle Possessing Magnetic Charge 51
4.1.3 Motion of a Relativistic Particle Possessing Magnetic Charge . . 52
4.2 Track Finding using FELIX 54
4.2.1 Track Finding in $r-\phi$ 54
4.2.2 Track Finding in $s-z$ 55
4.2.3 Performance of Parabolic $s-z$ Track Finder on Particles without Magnetic Charge 56
4.2.4 Performance of Parabolic $s-z$ Track Finder on Particles with Magnetic Charge 58

5 Data Reduction 63
5.1 Cuts on Events Fitted Linearly in $s-z$ 64
5.2 Cuts on Events After Refitting in $s-z$ 65

6 Analysis and Results 67
6.1 Analysis of the Curvature Coefficients 67
6.1.1 Defining the Magnetic and Non-Magnetic Regions 69
6.2 Calculating the Monopole Detection Efficiencies 74

6.2.1 Effect of χ^2 Cuts on Efficiencies 74
6.2.2 Monopole Detection Efficiencies for 1986 75
6.3 Effects upon Detection Efficiencies 78
6.3.1 Intrinsic Electric Charge 78
6.3.2 Incoherent Noise 78
6.3.3 Smearing of $\langle dE/dx \rangle$ 80
6.3.4 Vertex Constraint in $s - z$ Fit 80
6.4 The Effects of High Energy δ-rays 82
6.4.1 What are δ-rays? 82
6.4.2 Why Could δ-rays be a Problem? 83
6.4.3 Simulating the Effect of δ-rays 84
6.4.4 Consequence of High Energy δ-ray Emission 84
6.5 Cross-Section Limits of Monopole Production 85

II Multi-Pulse Performance of a Test Drift Cell for Zeus 89

7 A Test Drift Cell for ZEUS 91
7.1 HERA and ZEUS 91
7.2 The Rectangular Cell Test Chamber 94
7.2.1 Chamber Construction 94
7.2.2 Chamber Electronics 94
7.2.3 Operating the Chamber 94
7.3 Chamber Pulses and Their Output from FADCs 96
7.3.1 Defining pulses in the FADC output 97
7.4 Determining Hit Positions and Spatial Resolutions 99
7.5 Determining the dE/dx Resolution 101

8 Multi-Pulse Performance of the Drift Cell 103
8.1 Adding Together the Pulses 104
8.2 Two-Pulse Resolution Efficiency 107

8.3 Two-Pulse Spatial Resolution 110
8.4 Two-Pulse dE/dx Resolution 114
8.5 Correcting the Timings and Pulse Sizes 118
8.5.1 Finding the Corrections 118
8.5.2 Effect of Corrections upon Timings 119
8.5.3 Effect of Corrections upon Pulse Sizes 128
8.6 Conclusions to Multi-Pulse Analysis 131

A TASSO Track Parameters **132**

B Calculating Hits for Track Finding **134**
B.1 Hits in the $r - \phi$ Plane 134
B.2 Hits in the $s - z$ Plane 135

List of Figures

.1 The author's *Aufenthaltserlaubnis* iv

1.1 Feynman diagram showing $M\overline{M}$ production from e^+e^- annihilation . . . 7

2.1 The DESY site 12

2.2 Monthly integrated luminosity collected by TASSO, 1979–1986 15

2.3 Monthly account of PETRA e^+e^- centre of mass energy, 1979–1986 . . 15

2.4 View of TASSO from the east end 17

2.5 View of TASSO from above 18

2.6 Layout of the DC as cut along the beam axis 20

2.7 Drift cell geometry in the DC 20

2.8 Configuration of 1986 TASSO data acquisition system 25

3.1 $\langle dE/dx \rangle$ losses by ionization in DC 34

3.2 Effect of β^2 term upon $\langle dP/dx \rangle$ 34

3.3 ⟨dE/dx⟩ losses in JADE jet chamber 35

3.4 Tuned dE/dx algorithm showing losses for JADE jet chamber and TASSO DC 35

3.5 Flowchart of stepping algorithm 38

3.6 Smeared dE/dx ionization losses in DC 39

3.7 Residual distributions for two DC0 layers and two DCα layers 45

3.8 Simulation of dead region in DCα layer 4 47

3.9 DC sense wire efficiencies found for 1986 data 47

4.1 Example of parabolic and straight line fits on straight tracks 57

4.2 Simulated monopole event with mass 11 GeV/c^2 and charge $g = 40e$ . . 59

4.3 Simulated monopole event with mass 7 GeV/c^2 and charge $g = \frac{137}{2}e$ . . 60

4.4 C distibutions from the parabolic fit in $s - z$ 61

6.1 Distribution of C_i against ΣC for the 1986 data and two Monte Carlo monopole data sets 68

6.2 Distribution in $|C_i|$ against ΔC where $C_1C_2 < 0$ for the 1986 data . . . 70

6.3 Distribution in $|C_i|$ against ΔC where $C_1C_2 > 0$ for the 1986 data . . . 71

6.4 Distributions of $|C_1| - \Delta C$ for the 1986 data 72

6.5 Distributions of $|C_1| - \Delta C$ with $C_1C_2 < 0$ for the 1986 data and two monopole data sets 72

6.6 Distributions in χ^2/n.d.f. for FOREST 76

6.7 Distributions in χ^2/n.d.f. for MILL 76

6.8 Efficiency plot for monopole detection 77

6.9 Effect of intrinsic electric charge on detection efficiencies 79

6.10 Effect of incoherent noise in the DC on detection efficiencies 79

6.11 Effect of smearing of $\langle dE/dx \rangle$ on detection efficiencies 81

6.12 Effect of vertex constraint in $s - z$ fit on detection efficiencies 81

6.13 The limits on $M\overline{M}$ production cross-section relative to the QED cross-section for the process $e^+e^- \rightarrow \mu^+\mu^-$ 86

6.14 Photographic evidence of the only Monopol(e) found in Hamburg 87

7.1 A segment of the ZEUS Central Track Detector 92

7.2 Geometry of chamber 95

7.3 FADC outputs for single track events 97

7.4 FADC output from a two-pulse event 98

8.1 FADC outputs before and after simulating double pulses 106

8.2 Efficiencies for finding two pulses as a function of pulse separation . . . 107

8.3 Two-pulse resolutions as a function of YCRITs 109

8.4 Two-pulse resolutions as a function of relative pulse sizes 109

8.5 Distribution of spatial resolutions as a function of pulse separation . . . 110

8.6 Distribution of dE/dx resolutions as a function of pulse separation . . . 115

8.7 Scaling factors used in dE/dx resolutions as a function of the separation of pulses 115

8.8 Distributions in⟨DELTT2⟩ and σ(DELTT2) using PIT→PEAK algorithm 120

8.9 Distributions in⟨DELTT2⟩ and σ(DELTT2) using BASELINE→PEAK algorithm 121

8.10 Distributions in⟨FACTP2⟩ and σ(FACTP2) using PIT→PEAK algorithm 122

8.11 Distributions in ⟨FACTP2⟩ and σ(FACTP2) using BASELINE→PEAK algorithm 123

8.12 Frequency distributions in the measured relative pulse sizes 124

8.13 Distributions in T2REAL−T2MEAS with corrections 125

8.14 Distribution of σ(DELTT2) as a function of measured pulse separation . 126

8.15 Effect of corrections upon the second pulse spatial resolution 126

8.16 Distribution of σ(DELTT2) with corrections using FACTP2 and DELTP2 parameterizations 127

8.17 Distributions in P2REAL/P2MEAS with corrections 129

8.18 Distribution of σ(FACTP2) as a function of measured pulse separation . 130

8.19 Effect of corrections upon the second pulse dE/dx resolution 130

A.1 TASSO track parameters 133

List of Tables

2.1 Sense wire geometry data for the DC 21

3.1 Materials in the VXD 40

3.2 Materials in the CPC 41

3.3 Materials in the DC 42

3.4 Atomic and nuclear properties of materials 43

3.5 DC sense wire resolutions tuned to 1986 data 46

3.6 DC sense wire efficiencies tuned to 1986 data 48

3.7 Vertex parameters tuned to 1986 data 48

4.1 Parabolic fit using least squares method 55

6.1 χ^2/n.d.f. cuts applied to data and Monte Carlo 75

8.1 Definitions of terms used in multi-pulse analysis 105

8.2 Characteristics of spatial and dE/dx resolution plots 111

8.3 Multi-pulse spatial resolution performance 111

8.4 Multi-pulse dE/dx resolution performance 116

Part I

A Search For Particles With Magnetic Charge Produced in e^+e^- Annihilation at $\sqrt{s} = 35$ GeV

Chapter 1

Introduction

1.1 In the Beginning...

When James Clerk Maxwell unified the forces of electricity and magnetism in the middle of the 19th century to establish the theory of electromagnetism, there appeared to be an intrinsic yet incomplete symmetry between the electric and magnetic quantities. This is clearly shown in Maxwell's equations:

$$\nabla \cdot \mathbf{D} = \rho_e \qquad \nabla \times \mathbf{H} = \frac{\partial \mathbf{D}}{\partial t} + \mathbf{j}_e \tag{1.1}$$

$$\nabla \cdot \mathbf{B} = 0 \qquad -\nabla \times \mathbf{E} = \frac{\partial \mathbf{B}}{\partial t} \tag{1.2}$$

where $\mathbf{D}$ is the electric flux density, $\mathbf{B}$ the magnetic flux density, $\mathbf{E}$ the electric field and $\mathbf{H}$ is the magnetic field. $\mathbf{j}_e$ and ρ_e are the electric current density and electric charge density respectively. The symmetry is incomplete due to the absence of $\mathbf{j}_m$ and ρ_m, the magnetic current density and magnetic charge density, from equations 1.2. This was because Maxwell's theory reflected the experimental position of the day, a position which so far has unaltered; whilst there are countless observations of electric field emerging from a single point, or source, there has never been any substantial evidence of the magnetic counterpart. Whenever a magnet is broken up there is always a north and a south pole attributable to the remaining parts; the magnetic flux lines are continuous and never appear to emerge from a single source. When it came to Dirac "inventing" a magnetically charged particle, or monopole [2], instead of predicting their existence, he assumed that they do exist and looked at the consequences of this.

If we add $\mathbf{j}_m$ and ρ_m to equations 1.2 so that they become

$$\nabla \cdot \mathbf{B} = \rho_m \qquad -\nabla \times \mathbf{E} = \frac{\partial \mathbf{B}}{\partial t} + \mathbf{j}_m \tag{1.3}$$

the symmetry is made complete. If we then make the following transformation through the real angle ξ:

$$\begin{array}{lcllcl} \mathbf{E} & = & \mathbf{E}'\cos\xi + \mathbf{H}'\sin\xi & \mathbf{D} & = & \mathbf{D}'\cos\xi + \mathbf{B}'\sin\xi \\ \mathbf{H} & = & -\mathbf{E}'\sin\xi + \mathbf{H}'\cos\xi & \mathbf{B} & = & -\mathbf{D}'\sin\xi + \mathbf{B}'\cos\xi \\ \rho_e & = & \rho'_e\cos\xi + \rho'_m\sin\xi & \mathbf{j}_e & = & \mathbf{j}'_e\cos\xi + \mathbf{j}'_m\sin\xi \\ \rho_m & = & -\rho'_e\sin\xi + \rho'_m\cos\xi & \mathbf{j}_m & = & -\mathbf{j}'_e\sin\xi + \mathbf{j}'_m\cos\xi \end{array} \tag{1.4}$$

we find that equations 1.1 and 1.3 are invariant under such a transformation. By choosing the ratio

$$\rho'_m/\rho'_e = \tan\xi \tag{1.5}$$

we can make a transformation so that $\mathbf{j}_m = 0$ and $\rho_m = 0$. This way equations 1.3 have been transformed back to the familiar equations 1.2, showing that it is simply a matter of convention to speak of a particle possessing electric charge, but not magnetic charge. So in actual fact Dirac's assumption was not so much that particles exist with magnetic charge, rather that there are particles that do not possess the universal ratio of electric to magnetic charge of equation 1.5.

To include monopoles within the framework of the recently formulated quantum mechanics, Dirac found that the magnetic field of a monopole was like that of an infinitely long thin solenoid that was, under certain circumstances, unobservable [3]. The argument went as follows. One way to observe the effect of a magnetic field of a solenoid is through the behaviour of electric charges passing through the field. Dirac was able to show that if the field of the solenoid was attributed to a magnetic charge at one end, the electric charge could not pass through the field and thereby render it observable for the following relationship between the electric charge e and magnetic charge g:

$$eg = \frac{1}{2}n\hbar c \qquad n = \pm 1, \pm 2, \pm 3, \ldots \tag{1.6}$$

In other words the unobservability of the monopole's "Dirac string", as it was later known, resulted in both electric and magnetic charges being quantized. Before this theory there had never been any sort of explanation of one of the most profound mysteries of the universe, why electric charge should be of a discrete nature. This theory showed that the existence of a monopole of magnetic charge $\frac{137}{2}e$, known as a Dirac monopole, would require all electric charges to be quantized in the units with which are found in

nature. As of yet there are still no other theories to explain the quantization of electric charge.

As well as simply possessing magnetic charge in the terms spoken of previously, there could also exist particles that possess both electric and magnetic charges (in different proportions to the universal ratio). These are known as dyons [4].

1.2 Searches for Magnetically Charged Particles

Owing to Dirac's theory and the fact that, at present, there appears to be no other explanation to why electric charge is quantized, there have been many searches for monopoles. Interest in monopoles was renewed in 1974 when they appeared to be a natural by-product of Grand Unified Theories or GUTs [5]. In these theories the mass of the monopole would be in the region of 10^{15} GeV/c^2. There is no theoretical reason, however, that there should not exist monopoles with much lower masses [6], accessible to particle accelerators.

As well as searches for GUT monopoles, there have been many searches at colliders for the existence of monopoles whose mass range is much lower and limited by the beam energy of the collider in question. For GUT monopoles the method of detection is to look for signals of particles passing through superconducting loops, known as SQUIDs, and which change the current in the loop by an amount expected for monopoles possessing the Dirac charge. If a normal magnetic dipole were the cause of the change in the current then when the opposite pole passes through the loop the current change would be reversed and the current level would revert to its original value. If a monopole were to pass through the loop there would be only one change in current. Such an experiment in Stanford in 1982 found what appeared to be a signal of a monopole [7], and in 1985, in a similar device at Imperial College, an unexplained event was recorded [8]. These have been the only two observations of what were, perhaps, GUT monopoles, despite the same team who found the signal in 1982 constructing a more sophisticated detector than the one originally used and obtaining no signals from the new detector [9]. Another way to search for monopoles and the method generally used at particle colliders, is to look for evidence of very heavily ionizing particles passing through sheets of plastic or kapton. Magnetically charged particles are expected to be very heavily ionizing [3], and so after the material is exposed to the interactions of many collisions, it is taken and etched. A scan is then made to see if there are any deep tracks passing straight through the material. Searches of this nature have been performed at the ISR [10], PEP [11], and PETRA [12]. In all cases the results have been negative. Searches of this sort have so far only been able to detect magnetically charged particles possessing magnetic charges greater than $30e \rightarrow 50e$. This sort of technique has also been applied to materials that may have been exposed to monopoles over a long period of time such as mica crystals found deep in the Earth, which have lain there for some 100 million years [13]. As in the other experiments no candidates for monopoles have been found.

1.3 The Search in TASSO

Another method with which to search for monopoles, which is an extension of the type III method of Amaldi *et al.* [14], is to look for tracks being curved by the magnetic field of a solenoid. This is the method employed in this analysis. It was first applied to an e^+e^- annihilation experiment by CLEO [15]. In e^+e^- annihilations, monopoles and dyons could possibly be produced via a single virtual photon as an $M\overline{M}$ pair, since magnetic charge is expected to be a conserved quantity. The Feynman diagram of such a process is shown in figure 1.1.

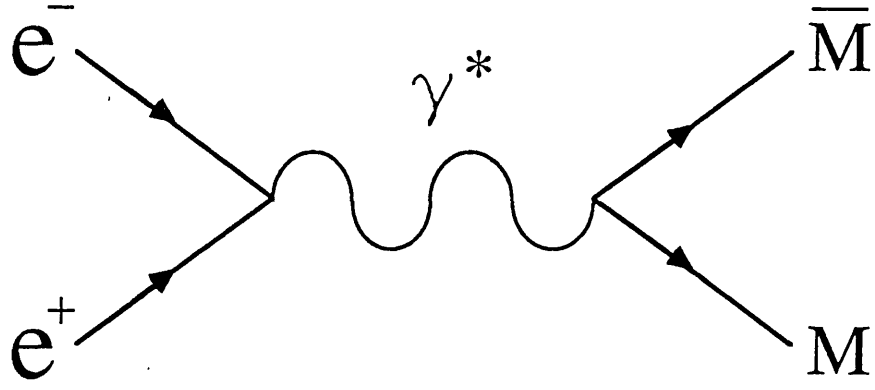


Figure 1.1: *Feynman diagram showing $M\overline{M}$ production from e^+e^- annihilation*

In the plane perpendicular to the beam and magnetic flux lines the $M\overline{M}$ pair will appear to be like any other two-prong event, the tracks being back-to-back in the absence of initial and final state bremsstrahlung. In the plane containing the magnetic flux lines the two particles will be accelerated by the magnetic field in opposite directions due to their opposite magnetic charges. An $M\overline{M}$ event will therefore be seen as a back-to-back two-prong event with tracks curving in opposite senses in this plane. In such an experiment a magnetically charged particle is simply defined as a particle that is accelerated along the flux lines of the magnetic field, a necessary requirement of such a particle. Such a technique for a search of magnetically charged particles is independent of the model of the interactions between the particles and the materials that make up the detector, provided the particles reach a triggering part of the experiment and leave an ionization trail.

In this, as well as any other search for magnetically charged particles, some assumptions have had to be made, as little is really known about the likely behaviour of such

particles. The coupling between magnetically charged particles and the photon has never been calculated, owing to the large (> 1) coupling constant expected for Dirac monopoles. Therefore cross-section limits calculated in the event of no magnetically charged particles being found cannot be compared with a theoretical calculation of the process $e^+e^- \rightarrow \gamma^* \rightarrow M\overline{M}$. The energy required to separate particles of opposite magnetic charge is also unknown, although Dirac did make a tentative prediction of 0.5 GeV for monopoles of a single Dirac charge [3]. Such a prediction would only have an effect on this analysis for particles heavier than ~ 15 GeV/c^2 for the 35 GeV centre of mass energy of the data used in this analysis. Since there are no other predictions the effect of the separation energy has been ignored. We have assumed that magnetically charged particles are purely electromagnetic and do not produce jets. Also, as we expect that the search is for the lightest of such particles, we have presupposed that they will not decay. The possibility of a dominant two-photon mechanism in the production of magnetically charged particles [16] has been ignored as the efficiencies of detecting such a process in TASSO would be much reduced.

The microscopic behaviour of magnetically charged particles interacting with matter is believed to be analogous to that of electrically charged particles, with the electric charge q replaced by $g\beta$ [17]. The β dependence is seen to be related to the $\mathbf{v} \times \mathbf{B}$ in the Lorentz equation for the motion of an electrically charged particle in a magnetic field B.

For such a model of magnetically charged particles interacting with matter, our search is found to be sensitive to a range of magnetic charge $10e < g < 70e$. For the CLEO experiment, the search was sensitive to $g < 10e$ and their mass limit was 5 GeV/c^2. They were restricted to such a low value of g because part of the trigger used was beyond the solenoid. This meant that magnetically charged particles with charges greater than $\sim 10e$ could not penetrate the coil to trigger the experiment. As the magnetic charges to which CLEO were sensitive to were so low, they employed a method of identification in which they compared the quality of the fit found using the standard linear fit for a track in the side view with that found using a parabolic fit on the same hits. As TASSO could trigger on particles with much larger magnetic charge, having all the necessary trigger components within the coil, we can identify magnetically charged particles using the curvature coefficients of the parabolic fits to the two tracks.

Since Dirac states that [3]

> *"The quantization of the equations of motion of charged particles and particles with [magnetic] poles is possible only provided the charges and poles are integral multiples of a unit charge* e_0 *and a unit pole* g_0 *satisfying* $e_0 g_0 = \frac{1}{2}\hbar c$."

it may be asked why we are searching for monopoles possessing sub-Dirac charges. Clearly the discovery of a monopole possessing the Dirac charge is necessary to confirm this statement, and would answer the great mystery of why electric charge should be quantized. (The next question that would then need answering would be about what fixes the values e_0 and g_0). On the other hand the quantization condition would be violated if a monopole were found with a magnetic charge that did not conform to the relationship of equation 1.6. It is just as viable to search for such monopoles so that, in Popperian terms, the theory may be falsified. After all, the non-observation of a Dirac monopole does not prove either way whether Dirac was correct or not, whereas the observation of a sub-Dirac charged monopole would disprove the theory. Although this analysis cannot actually determine the magnetic charge of any monopoles it may find, the curvature of a Dirac monopole is found, from Monte Carlo studies, to be very distinct from that of a monopole possessing a much lower magnetic charge.

The observation of a monopole or dyon would clearly be of importance in its own right, regardless of whether it possessed the Dirac charge or not.

Chapter 2

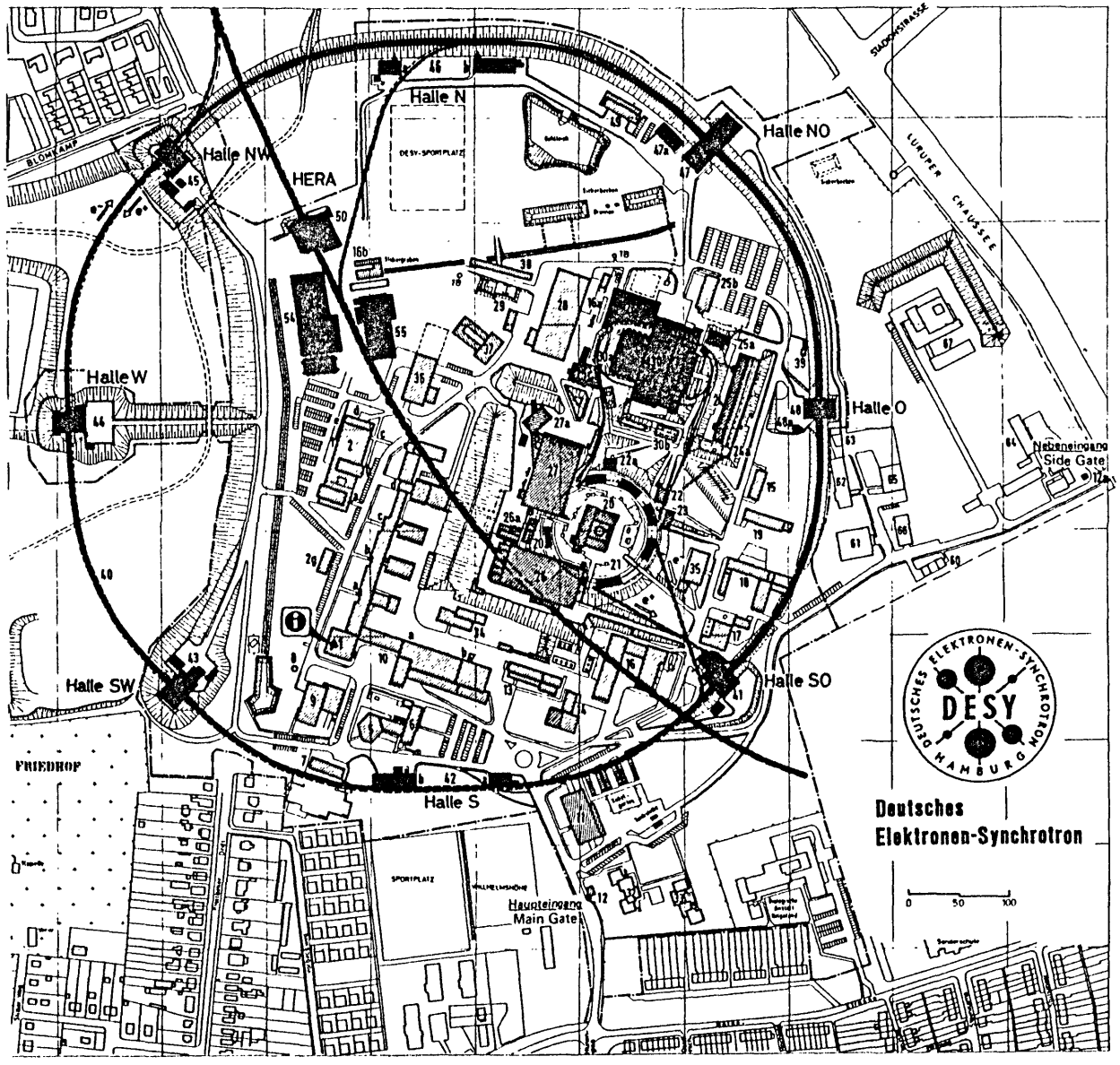
The Experimental Environment

The analysis was performed using data acquired by the TASSO (Twin Arm Spectrometer SOlenoid) detector which was situated in the south-east interaction region of the PETRA (Positron Electron Tandem Ring Accelerator) storage ring. It took data from e^+e^- interactions for the period of September 1978 to November 1986 with centre of mass energies ranging from 14 GeV to 46 GeV. PETRA is located in the DESY (Deutsches Elektronen-SYnchrotron) laboratory on the western side of the city of Hamburg, West Germany.

2.1 PETRA

The layout of the DESY site showing PETRA is shown in figure 2.1. TASSO was to be found on the ring in the position marked "Halle SO". In the interaction regions opposite and diagonal to TASSO were to be found the CELLO (Halle NO), JADE (Halle NW) and MARK J (Halle SW) detectors. In the eight curved sections of PETRA there were bending and focusing magnets, and in the four long straight sections there were radio frequency cavities used to accelerate the beams and compensate for the energy lost by synchrotron radiation.

Electron beams for the experiments were produced in LINAC I and accelerated to 50 MeV. They were then injected into the synchrotron DESY and accelerated up to 7 GeV before being injected into PETRA in the clockwise direction. Positrons were



Visitor Groups General Information

1	Laboratory 1
1a-1e	Entrances a-e
1c	DESY Directorate
1d	HERA Project Management
2	Laboratory 2
2a 2g	Entrances a-g
2a	Computer Center
5	Auditorium Entrance Building 6
6	Administration Building
7	Scientist's Guest House I
8,8a	Main Pump Station South/North
9	Cafeteria
10	Work Shop
10a,b	Entrances a,b
11	Purchasing Department
12	Gate Lodge Notkestraße
12a	Gate Lodge Luruper Chaussee
13	Liquifying Plant
14	Vacuum Laboratory
15	Scientist's Guest House IV
16	Power Station
16a,b	Power Station North/West
17	Heating Plant
18	Maintenance Building
19	Carpenter's Building
20	Main Building and Rectifying Plant
20a	NINA Hall
21	Synchrotron Ring Tunnel DESY
22	EMBL
22a	Vacuum Technic
23	220 MeV Linear Accelerator I
24	400 MeV Linear Accelerator II
24a	PIA
25	HASYLAB Experimental Hall
25a	EMBL
25b	HASYLAB Laboratory
25c	HASYLAB X-ray Wiggler Hall
26	Experimental Hall I
26a	Training Area
27	Experimental Hall II
27a	Test Transmitter Hall
28	Experimental Hall III
29	Iron Removal Plant
30	Storage Ring DORIS
30a	DORIS Surveying Station
32	Scientist's Guest House II
33	Scientist's Guest House III
34	Training Area
35	Safety and Inspection Group + Telephone Exchange
36	Preparation Hall
37	Assembly Hall
38	Test Hall HERA
40	Storage Ring PETRA
41,42 43,44 45,46 47,48	PETRA Halls
47a	Compressor Building
49	Cryotechnic
50	HERA Hall West
51 52 53	HERA Halls N,E,S (s. last page)
54	Cryotechnic
55	Magnet Measurement Hall
60-67	Hamburg University
60	Grounds Manager
61	Auditorium
62	Laboratories
63	Isotope Laboratory
64	Preparation Building
65	Work Shop
66	Pavilion
67	Cyclotron Plant

Besuchergruppen Allgemeine Information

1	Laborgebäude 1
1a-1e	Eingänge a-e
1c	DESY Direktorium
1d	HERA Projektleitung
2	Laborgebäude 2
2a-2g	Eingänge a-g
2a	DESY Rechenzentrum
5	DESY-Hörsaal Eing. Geb. 6
6	Verwaltungsgebäude
7	Gästehaus I
8,8a	Hauptpumpwerk Süd/Nord
9	Kantine
10	Werkstattgebäude
10a,b	Eingänge a,b
11	Warenwirtschaft
12	Pförtner Notkestraße
12a	Pförtner Luruper Chaussee
13	Verflüssigergebäude
14	Vakuumlabor
15	Gästehaus IV
16	Kraftstation
16a,b	Kraftstation Nord/West
17	Heizzentrale
18	Betriebshof
19	Tischlerei
20	Zentralgeb. und Gleichrichter
20a	NINA Halle
21	Synchrotron-Ringtunnel DESY
22	EMBL
22a	Vakuumtechnik
23	220 MeV-Linearbeschleuniger I
24	400 MeV-Linearbeschleuniger II
24a	Positronen-Intensitäts-Akkumulator PIA
25	HASYLAB Experimentierhalle
25a	EMBL
25b	HASYLAB Laborgebäude
25c	HASYLAB Röntgen Wiggler-Halle
26	Experimentierhalle I
26a	Ausbildung Elektro Berufe
27	Experimentierhalle II
27a	Test Sender Halle
28	Experimentierhalle III
29	Entsenesungs-Anlage
30	Speicherring DORIS
30a	DORIS Meßstation
32	Gästehaus II
33	Gästehaus III
34	Ausbildungswerkstatt
35	Technischer Notdienst + Fernmeldetechnik
36	Vorbereitungshalle
37	Betriebslagerhalle
38	Testhalle HERA
40	Speicherring PETRA
41,42 43,44 45,46 47,48	PETRA Hallen
47a	Kompressorhaus
49	Kryotechnik
50	HERA Halle West
51 52 53	HERA Hallen N,O,S (s. Rückseite)
54	Kaltetechnikhalle
55	Magnetmeßhalle
60-67	Physik, Institute der UNI Hamburg
60	Hausmeister
61	Hörsaal
62	Laborgebäude
63	Isotopenlabor
64	Vorbereitungsgebäude
65	Werkstatt
66	Pavillon
67	Zyklotronanlage

Figure 2.1: *The DESY site*

produced, via pair production, by bombarding a tungsten target with a low energy electron beam. They were then accelerated to 400 MeV using LINAC II after which they were stored in PIA (Positron Intensity Accumulator) until there were sufficient numbers to be injected into DESY to accelerate to 7 GeV before injection into PETRA in the anti-clockwise direction. PETRA operated with two bunches of electrons against two bunches of positrons with beam currents that were typically 10 mA for both electrons and positrons. Beam crossings occurred every 3.8 μs.

One key parameter in the performance of a colliding beam machine is expressed by the luminosity, L. The event rate of a process whose cross-section is σ is given by

$$\frac{dN}{dt} = L\sigma \tag{2.1}$$

A cross-section for a process is therefore calculated as

$$\sigma = \frac{N}{\int L(t)\, dt} \tag{2.2}$$

where N is the number of events of that process that are produced and $\int L(t)\, dt$ is the integrated luminosity. For an e^+e^- colliding beam machine with head-on collisions

$$L = \frac{n^+ n^- f}{4\pi\sigma_x\sigma_y} \tag{2.3}$$

where
$n^\pm$ = *no. of* $e^\pm$ *per bunch*
f = *beam collision frequency*
σ_x, σ_y = *r.m.s. beam widths in the horizontal and vertical*

As some of the above parameters cannot be measured accurately, measurement of the luminosity was calculated by each of the experiments using the Bhabha ($e^+e^- \rightarrow e^+e^-$) scattering rate at small angles to the beam axis, where the momentum transfer Q^2 is low. This scattering in TASSO was picked up by luminosity monitors [18,19] close to the beampipe beyond the main detector, with a systematic error smaller than 4%. The process has a very high cross-section which can be calculated very accurately using QED and a high event rate that can be measured with a small statistical error, so that the luminosity can be calculated very precisely using equation 2.1. The luminosity can be increased by narrowing the beams close to the interaction point, thereby reducing σ_x and σ_y in equation 2.3. For this purpose mini-β quadrupoles were installed at each of the experiments in 1983, improving the luminosity by a factor ~ 3 resulting in a peak luminosity of $\sim 1.7 \times 10^{31}$ cm^{-2}s^{-1} for beam energies of 17.5 GeV.

Figure 2.2 shows the monthly integrated luminosity collected by TASSO from start to finish of data-taking. Together with the distribution in the centre of mass energy, shown in figure 2.3 we get a picture of the performance of PETRA during its lifetime as an e^+e^- colliding beam machine. It was the high total luminosity taken during 1986 along with the attraction that it was all at one energy in clean running conditions that prompted this data-taking period to be employed in the search for magnetically charged particles.

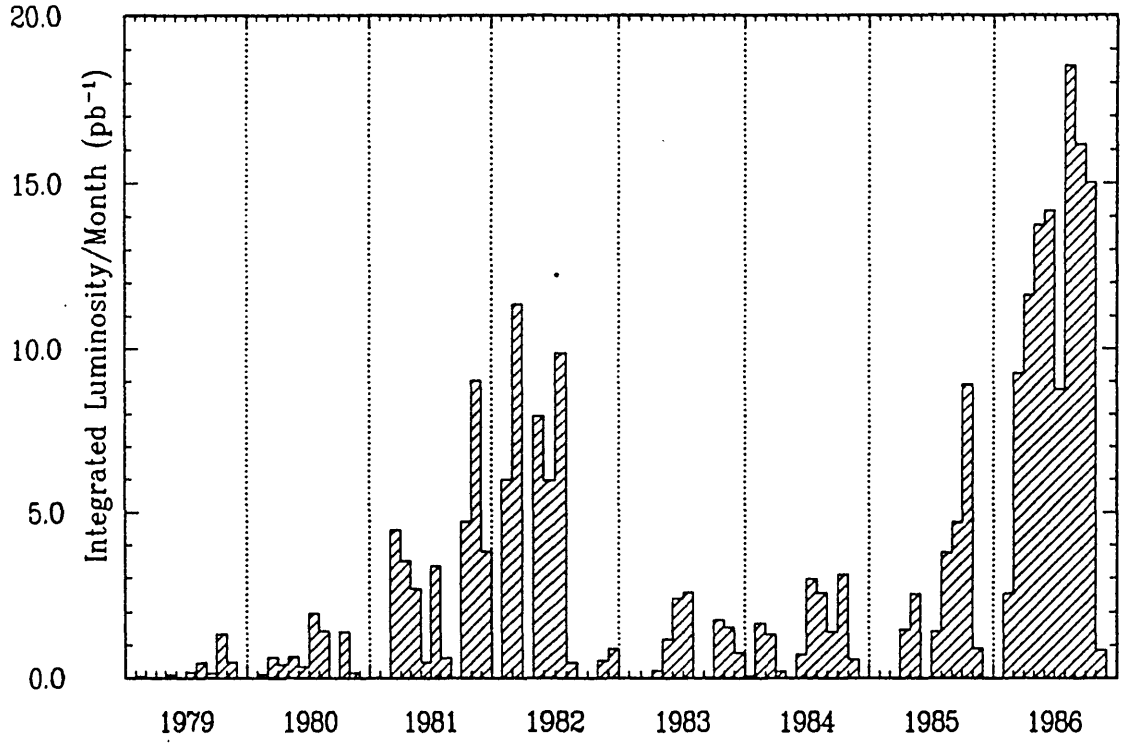


Figure 2.2: *Monthly integrated luminosity collected by TASSO, 1979-1986.*

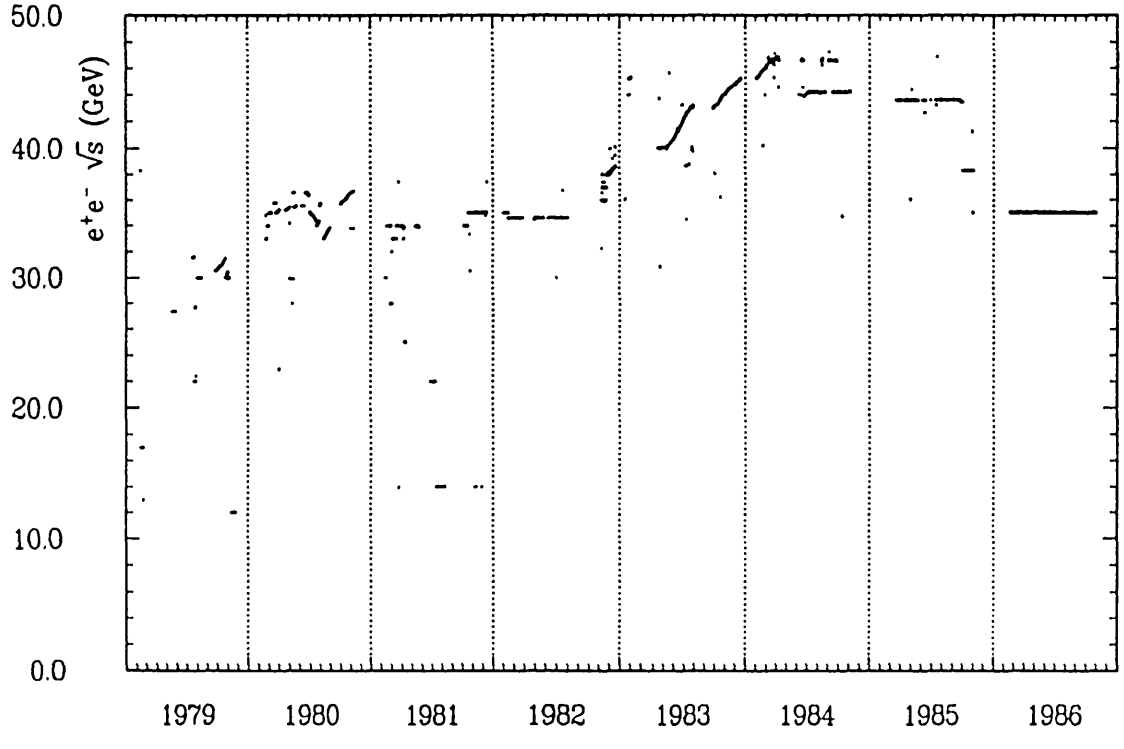


Figure 2.3: *Monthly account of PETRA e^+e^- centre of mass energy, 1979-1986.*

2.2 TASSO

The TASSO detector was designed as a general purpose experiment, with particular emphasis upon the tracking of charged particles by the central detector, the indentification of charged particles by the hadron arms and detection of neutral particles by liquid argon calorimeters. Views of TASSO are shown in figures 2.4 and 2.5. Only the central detector which comprises the vertex detector, cylindrical proportional chamber, drift chamber, inner time of flight counters and coil, were involved in this analysis and so no further consideration is made of the detectors outside of the coil, which are written up elsewhere [20,21,22,23,24]. The co-ordinate system and definitions used by the experiment and this analysis are to be found in appendix A.

2.2.1 The Vertex Detector (VXD)

The VXD [25], with its beryllium beampipe forming the inner casing at a radius of 6.5 cm from the interaction point, would have been the first component any particles produced in an e^+e^- annihilation would have encountered. It was designed and used as a small high precision drift chamber extending to an outer radius of 16.1 cm and with an active length of 57.2 cm. It consisted of 8 coaxial layers of drift cells with all wires laying parallel to the beam axis, and was inserted into TASSO in 1983. For measurements in z, charge division readings from layers 3,4,7 and 8 were originally envisaged, but owing to the poor spatial resolution achieved, they were not employed during the 1986 data-taking period. In this analysis, no hits from the VXD were used in track reconstruction, due to the enormous increase in computing required for negligible benefits. The only information required about the VXD for this analysis was its mechanical construction, so as to be included in the Monte Carlo when considering the matter interactions of the magnetically charged particles as they passed through each detector component (see section 3.5). The gas in the VXD was a mixture of 95% argon and 5% carbon dioxide. The chamber operated at a pressure of 3 atmospheres.

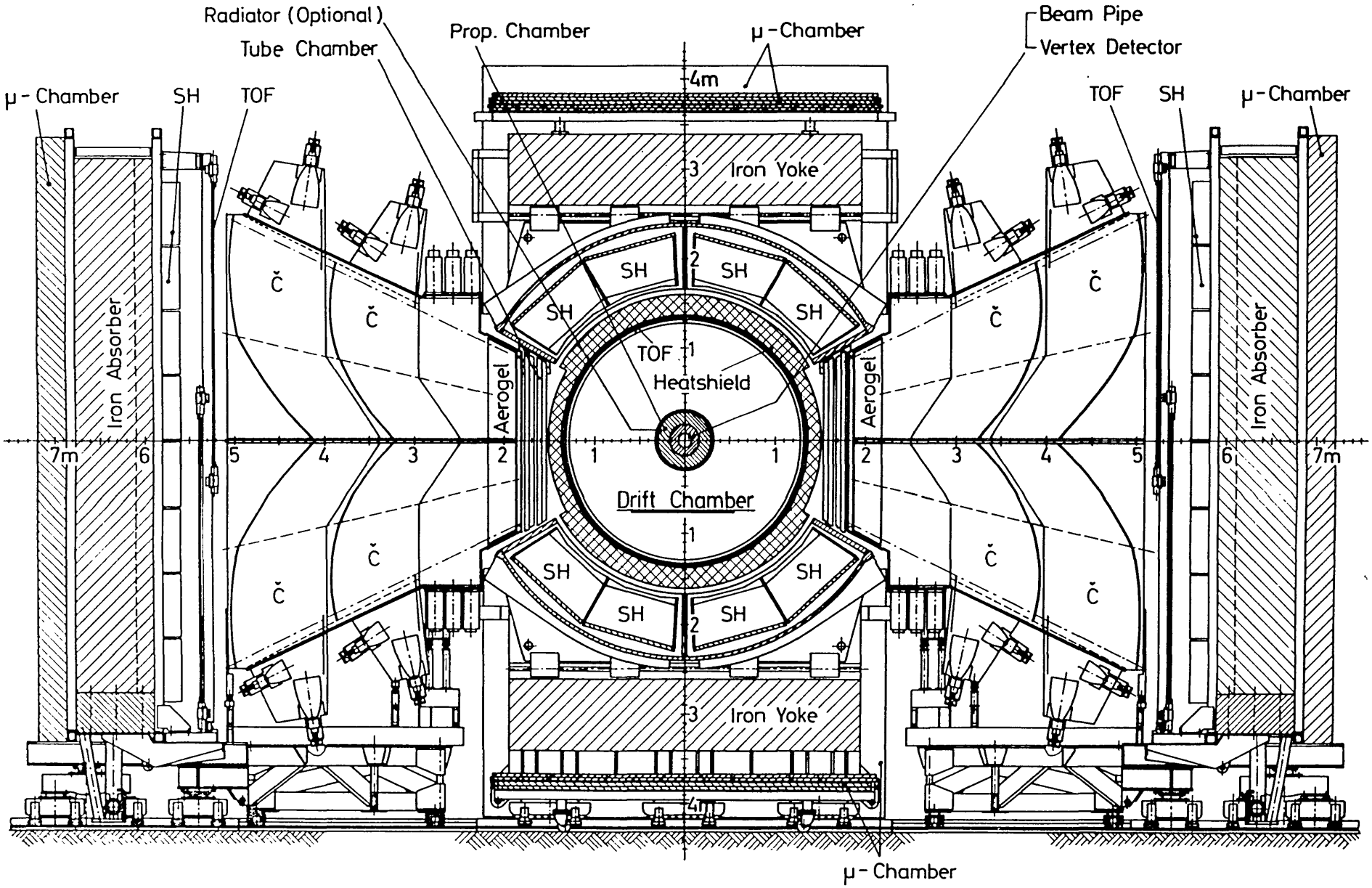


Figure 2.4: *View of TASSO from the east end*

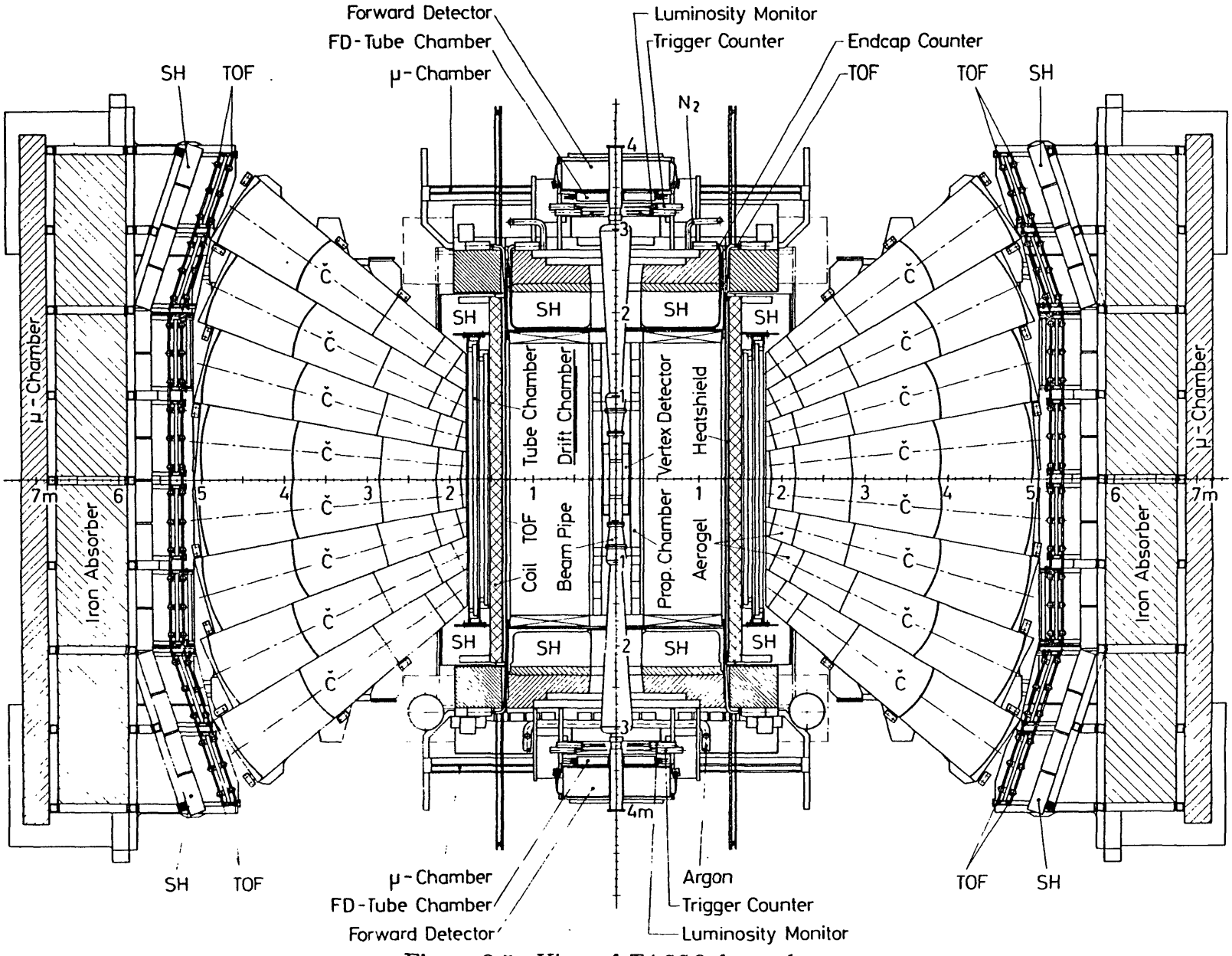


Figure 2.5: *View of TASSO from above*

2.2.2 The Cylindrical Proportional Chamber (CPC)

The CPC [26,27] was a multiwire proportional chamber situated between the radii of 16.8 cm and 29.8 cm with an active length of 144.0 cm. It contained 4 axial layers, each with 480 sense wires for measurement of $r-\phi$ hits which were used in the track reconstruction of this analysis. There were also 120 inner and 120 outer helix cathode strips with pitch angles $+36.5°$ and $-36.5°$ respectively. These were intended for z measurements but, like the VXD charge division layers, were not read out during the 1986 data-taking period. The gas in the chamber was 75% argon, 25% isobutane plus a small addition of freon, at atmospheric pressure. As well as providing tracking information, it was primarily part of TASSO's charged particle trigger in conjunction with the drift chamber and inner time of flight counters.

2.2.3 The Drift Chamber (DC)

The DC [28] provided most of the $r-\phi$ tracking information and all of the z tracking information for this analysis. It occupied the region between the radii of 32.0 cm and 128.0 cm, with an active length of 323.0 cm. The layout of the chamber is shown in figure 2.6. It consisted of 15 coaxial layers of 1.2 cm high drift cells with a maximum drift distance of 1.6 cm in the arrangement shown in figure 2.7. Nine of the layers were parallel to the beam axis and are referred to as the DC0 layers whilst the other six layers were at stereo angles to the beam axis ranging from 3.36° to 4.51°. These were the DCα layers. Hits from the DC0 layers were used in the reconstruction of tracks in the $r-\phi$ plane, whilst the DCα layers were used to reconstruct each track in $s-z$ with the aid of the $r-\phi$ track just found (see appendix B). The radii and stereo angles as well as the number of drift cells for each layer are shown in table 2.1. The chamber gas was a mixture of 50% argon and 50% ethane at atmospheric pressure. Using this gas mixture the drift velocity of the ionized electrons was ~ 50 μm/ns. The resolutions of the DC0 layers were between 220 - 270 μm depending upon the angle of entry of the track into the cell. For the DCα layers, the resolutions were the axial resolutions divided by $\tan\alpha$.

Pulses picked up on any sense wires from the ionization of particles traversing the drift cells were transmitted to Time to Digital Converters (TDCs) via twisted pair

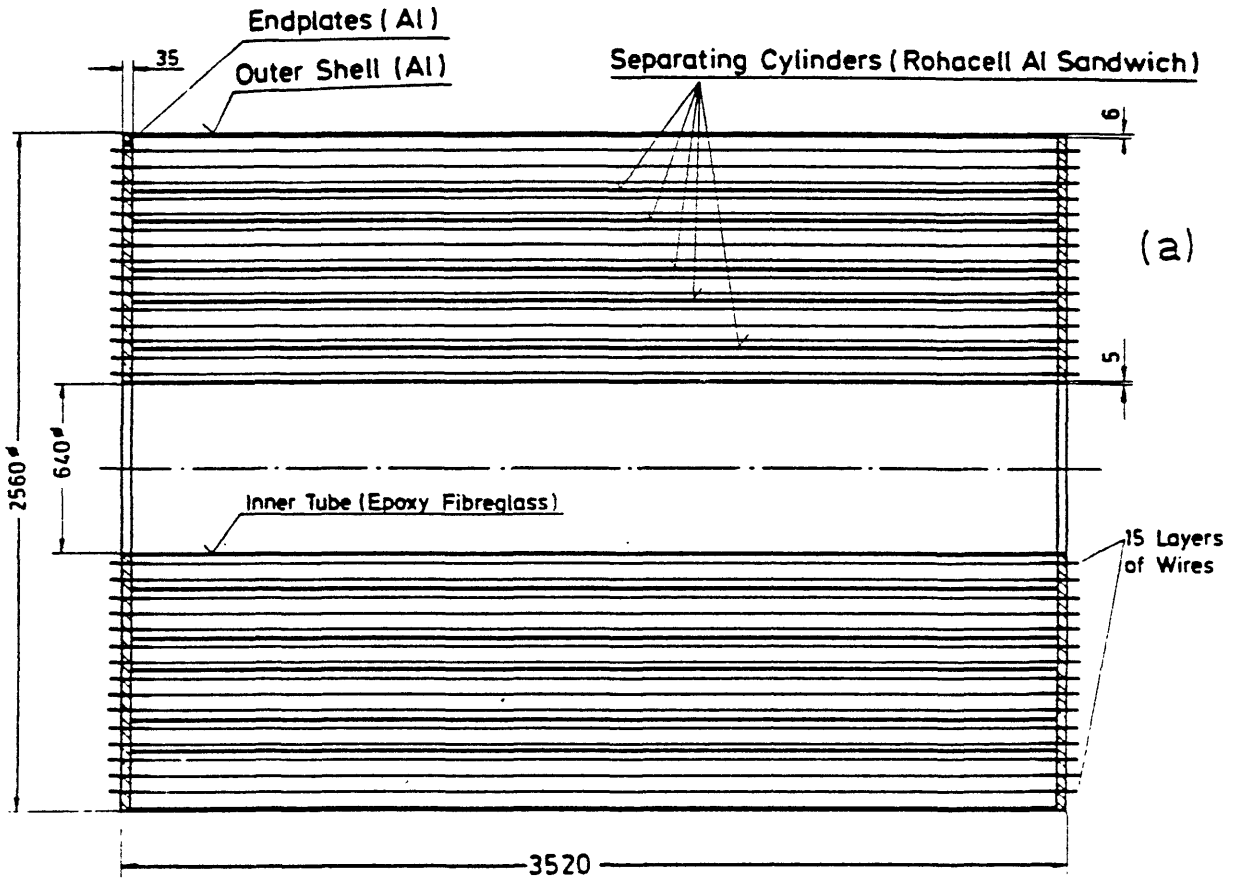


Figure 2.6: *Layout of the DC as cut along the beam axis. Dimensions are in mm.*

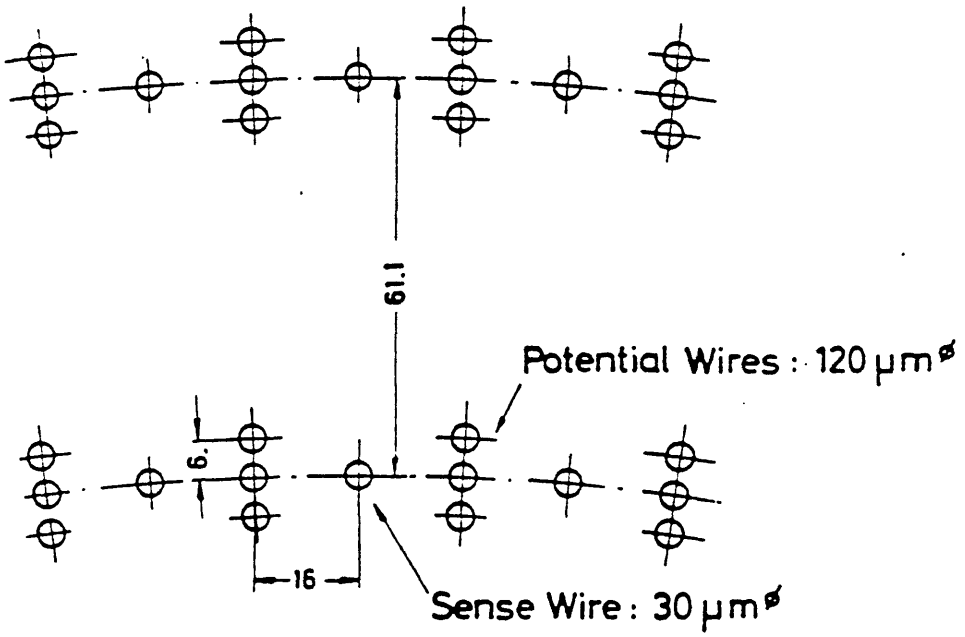


Figure 2.7: *Drift cell geometry in the DC. Dimensions are in mm.*

Layer	No. Drift Cells	Radius (cm)	Stereo Angle α
1	72	36.7	0°
2	84	42.8	+3.36°
3	96	48.9	0°
4	108	55.0	−3.37°
5	120	61.1	0°
6	132	67.2	0°
7	144	73.3	+3.94°
8	156	79.5	0°
9	168	85.6	−4.50°
10	180	91.7	0°
11	192	97.8	0°
12	204	103.9	+4.50°
13	216	110.0	0°
14	228	116.1	−4.51°
15	240	122.2	0°

Table 2.1: *Sense wire geometry data for the DC*

cables. The TDC started counting when the signal from the wire exceeded a predetermined level and ceased counting when stopped by a beam pickup signal delayed by $\sim$ 200 ns. The difference in the two counts, converted into a time, gave the drift time. The electronics used had only a single hit capability so that if more than one particle passed through a cell only a reading for the particle nearest the sense wire was registered. This reading, along with timing corrections for time of flight and signal propagation down the wire gave a drift time which was converted into a drift distance by using a corrected drift velocity for the cell [29]. The drift distance then gave us two hits, one either side of the wire, as the direction of drift was unknown before track reconstruction.

2.2.4 The Inner Time of Flight Counters (ITOFs)

The ITOFs [30] were situated just beyond the DC at a radius of 132.0 cm. They were used for triggering, particle indentification and cosmic ray event rejection. The ITOF system comprised 48 strips of plastic scintillator, each $390 \times 17 \times 2$ cm^3 arranged cylindrically around the DC. In conjunction with the CPC and DC they made up the charged particle trigger which limited the acceptance of triggering possible magnetic charged events to a maximum of 82% of 4π with a 98% trigger efficiency. In this analysis it was found to be greatly advantageous that they were inside the coil so that

events were triggered before the particles reached the coil. Particles with large magnetic charges would not have penetrated the coil due to their high rate of energy loss (see section 3.3).

2.2.5 The Magnet Coil

The solenoid magnet [20,31] within TASSO was used to bend the paths of charged particles so as to measure their momenta and in our case to accelerate magnetically charged particles in the direction of the beam axis. It was a warm water-cooled coil of length 440 cm with an inner radius of 135 cm. The coil was wound in 4 layers with a total of 336 windings. The maximum field strength during the 1986 data-taking period was 0.494 Tesla with a maximum field inhomogeneity along a track within the DC of $\sim 4\%$.

2.3 Data Acquisition and Reduction

For the detector to read out all its data and have it processed by the online computer took $\sim$ 50 ms. With beam crossings occurring every 3.84 μs it was clearly not possible to read out the results of every beam crossing. It was therefore necessary for the experiment to make quick decisions on which crossings had produced potentially interesting results. Many beam crossings resulted in low angle Bhabha scatters which were used to find the experiment's luminosity, but which did not enter the main detector. Crossings that resulted in Bhabha scattering, scattering of photons 'bremsstrahlunged' from the beams or the annihilation and creation of new particles were referred to as events. An event was of interest if it fell within the acceptance of the detector. As well as these events there were background processes which were not of interest, such as cosmic ray events and beam gas interactions. It was therefore desirable for the experiment to trigger the reading out of the data only for events that were of real interest as once a trigger decision had been made any interesting events within the following $\sim$ 50 ms would be missed. In reality the best that could be achieved was to reduce the number of background events that triggered the experiment to an acceptable level. The aim for the trigger was to keep the "dead time", caused when the detector was blind to events whilst reading out, as low as possible, whilst at the same time keeping the triggering efficiencies for various processes as high as possible. Raising this dead time resulted in lowering the integrated luminosity of the experiment.

2.3.1 The Trigger

TASSO was designed to investigate a large number of different events with different final states. Due to the high speed necessary in processing, the triggers relevant to this analysis dealt with events in the $r-\phi$ plane where magnetically charged particles would be indistinguishable from magnetically neutral particles (see section 4.1). The triggers of interest to this analysis were the two-prong triggers [32] as our events were expected to consist of two high momentum back-to-back tracks that would reach the ITOFs, ionization losses permitting. The two-prong trigger consisted of two components. The first involved just the CPC and ITOFs, looking for correlations between CPC trigger bits and fired ITOFs that indicated straight tracks from the vertex to within ± 1 sector,

there being a total of 48 azimuthal sectors, one per ITOF counter. If two such tracks were found then a trigger was set if there was a back-to-back correlation to within ± 2 sectors. This trigger component also involved the endcap TOFs, but due to the likely reduced efficiencies in triggering by highly ionizing magnetically charged particles and the reduction in z information for such events, we limited the search to those events triggered with the ITOFs. The other component of the two-prong trigger relied upon the additional trigger information from the six trigger layers of the DC. This involved 15 track masks corresponding to different values of $p_\perp$. A track was found if at least 5 out of the 6 wires along a mask had been hit along with the CPC trigger bit nearest to the innermost wire on the mask and an ITOF to within ± 1 sector of the extrapolated track. A trigger was then set if two such tracks were found to be back-to-back to within ± 3 ITOF counters, or, depending on the run conditions, if the innermost wires on the track masks were back-to-back to within ± 2 wires, ignoring the ITOF information. The two-prong trigger worked with 98% efficiency.

2.3.2 Data Acquisition

Each time there was a beam crossing a strobe was obtained from induced pulses on a beam pickup 7.1 m away from the collision point. This strobe set the gate timings and reset various electronic equipment. The data from most of the electronic channels were fed into fast "trigger processors" synchronized with the beam crossings.

The configuration of the TASSO data acquisition system for the 1986 data-taking period is shown in figure 2.8. When the main trigger supervisor, SIGH (**S**trobe **I**nterrupt **G**ate **H**andler) received a trigger signal from one or more of the trigger processors, communication with the front-end processor was made. If the data flow were not busy, the front-end processor would interrupt the SIGH and disable strobes and resets to equipment for subsequent beam crossings until all the relevant detector channels had been read out.

After a software programmed rejection of a small proportion of events within the front-end processor, most of the events were transferred to the online computer, a VAX 750. The events were then sent to one of a number of 370/E emulators to be partially processed before being sent to the DESY computer centre IBM for further processing.

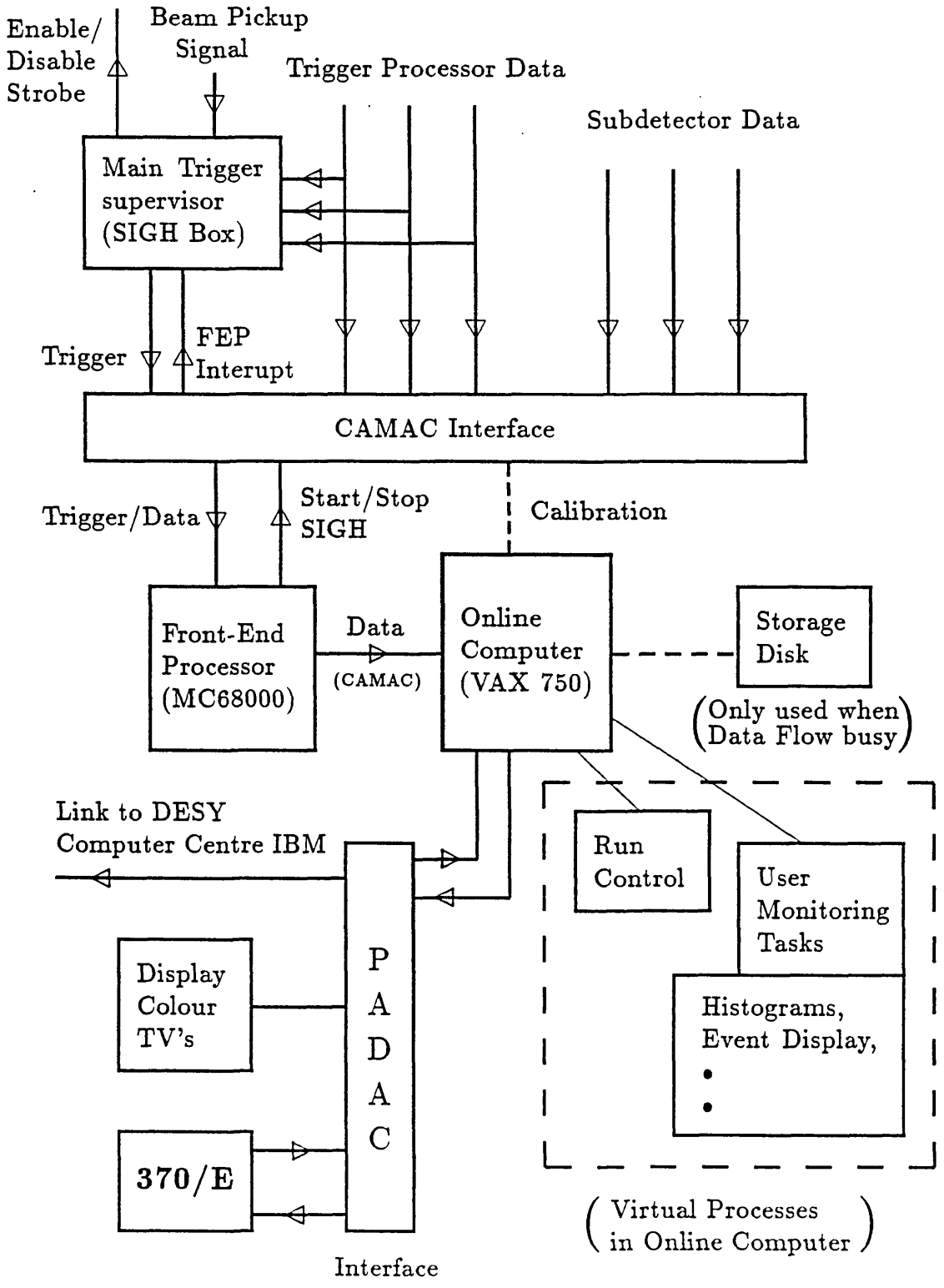


Figure 2.8: *Configuration of 1986 TASSO data acquisition system.*

The events were finally stored onto what were known as dumptapes. Some of the events were also copied into a user buffer for online monitoring processes. There was also a spare disk available for temporary storage when data transfer was busy or for when the IBM or its link were down.

2.3.3 Data Reduction

Whilst in the emulator and on the IBM, the data from each event had up to two track reconstruction programs applied to it. The first, FOREST [33] was a track finder based on a minimum spanning tree algorithm. Tracks in $r-\phi$ were found using DC0 hits with the assumption of a linear space-time drift relation. For each track successfully fitted in $r-\phi$, an attempt was made to reconstruct the track linearly in $s-z$ using the DCα hits. FOREST was applied to all events. From the tracks found by FOREST, a decision was made whether to then apply the MILL track finder. If an event passed the following criterion relevant to the process being searched for in this analysis then MILL was applied to it:

- There were ≥ 2 tracks reconstructed in $r-\phi$ and ≥ 1 track reconstructed in three dimensions with $|d_0| < 2.5$ cm and $|z_0| < 8.0$ cm.

MILL was basically the same track finder as FOREST except it was more exhaustive in its search and used non-linear drift time corrections, thereby being more efficient in its track finding and producing a better quality of track with lower χ^2/n.d.f.

The reconstructed events, whether by FOREST or MILL, were stored on dumptapes which were copied onto PASS 1 tapes with no data reduction, so that PASS 1 tapes contained all the events that had been triggered.

As so many events got written to PASS 1 tapes, the majority of which were not of interest to physics analysis, there existed a data reduction chain to remove background processes and poorly reconstructed events and allow events of interest such as multi-hadronics, Bhabhas and muon pairs to pass through with high efficiency. Unfortunately the first selection criterion that would involve events of interest to us was identical to

that used in deciding whether an event should have MILL applied to it or not. As will be explained in chapter 5 this resulted in many events of interest to us not passing onto the PASS 2 tapes and so the analysis was performed using the PASS 1 tapes. Any further passes down the data reduction chain to other PASS tapes are of no relevance to this analysis and so are not considered.

Chapter 3

Simulating Magnetically Charged Particles

To determine with what efficiencies monopoles of various masses and magnetic charge can be detected, we must be able to simulate what happens when $M\overline{M}$ pairs are produced and go through the TASSO central detector up to the ITOFs. At this point an event can be triggered. Included in the simulation must be interaction effects between the monopoles and magnetic field, and the monopoles and the materials that make up the detector components. Also the individual performance of important components must be tuned to recreate their performance during the period of data taking.

3.1 The MONSTER Monte Carlo

To simulate the monopoles going through the detector we used the MONSTER [34] Monte Carlo that explicitly steps each particle through the detector allowing us to make changes to the trajectory due to energy losses, multiple scattering and the magnetic field at each step. Our events were generated using a $\mu^+\mu^-$ generator adapted to produce particles of a given mass isotropically without radiative corrections, the magnetic charge being relevant only when passing through the detector. We allowed the Monte Carlo to take the particles up to the ITOFs where the event, in reality, would be triggered. If a particle exited through the endcaps of either the VXD, CPC or DC we stopped the stepping and went on to the next particle or event. After an event was completed the Monte Carlo decided which wires would have signals on them and the drift distance to

the wires. As there was no z information from either the VXD or CPC in the 1986 data, the charge division layers and cathode strips were not read out in the simulation.

3.2 Stepping the Particles

In classical electrodynamics the Lorentz-invariant equation of motion of a particle possessing both electric and magnetic charge in a magnetic field is

$$\frac{d\mathrm{p}}{dt} = g\mathrm{B} + q\mathrm{p} \times \mathrm{B}/\gamma m \tag{3.1}$$

where q is the electric charge, g is the magnetic charge and m the rest mass of the particle. For a uniform magnetic field B in z, the components of motion become

$$\begin{aligned} \frac{dp_x}{dt} &= qp_yB/\gamma m \\ \frac{dp_y}{dt} &= qp_xB/\gamma m \\ \frac{dp_z}{dt} &= gB \end{aligned} \tag{3.2}$$

Clearly for a monopole, which possesses no electric charge, $q = 0$.

To calculate the position and momentum components at each step, the Euler method was employed to calculate the following equations:
For $\mathrm{X} = x, y, z$

$$\mathrm{X}^{n+1} = \mathrm{X}^n + \left(\frac{p_\mathrm{x}^n}{\gamma m}\right)\Delta t \tag{3.3}$$

where n is the time step, and

$$p_\mathrm{x}^{n+1} = p_\mathrm{x}^n + \left(\frac{dp_\mathrm{x}}{dt}\right)\Delta t - \left(\frac{dp_\mathrm{x}}{d\mathrm{X}}\right)\Delta \mathrm{X} \tag{3.4}$$

where $\left(\frac{dp_\mathrm{x}}{dt}\right)$ is the motion component and $\left(\frac{dp_\mathrm{x}}{d\mathrm{X}}\right)$ is the momentum change from dE/dx losses due to ionization and bremsstrahlung.

3.3 Matter Interactions of Monopoles

It is believed that particles such as monopoles and dyons interact with matter quite substantially [3]. So to get a reliable measurement of the efficiencies for detecting monopoles it is important to include the interactions of magnetically charged particles with the matter that they may traverse. Whilst interactions of electrically charged particles in matter are very well understood, this is not the case with magnetically charged particles. So, following the method in reference [17], we have assumed that the microscopic behaviour of monopole interactions can be calculated using the symmetrized Maxwell's equations 1.1 and 1.3. Effectively, the electric charge q is replaced by $g\beta$. Important in our studies are the effects of ionization, bremsstrahlung and multiple scattering.

3.3.1 Ionization

When a particle of electric charge q passes through a medium it will lose energy principally via Coulomb interactions with the medium's electrons. The mean energy loss per unit length is given by the Bethe-Bloch equation [35,36]:

$$\left\langle \frac{dE}{dx} \right\rangle_{BB} = \frac{DZ\rho}{A} \left(\frac{q}{e\beta} \right)^2 \left[\ln \left(\frac{2m_e\gamma^2\beta^2c^2}{I} \right) - \beta^2 - \frac{\delta}{2} - \frac{C}{Z} \right] \{1 + \nu\} \qquad (3.5)$$

where $D = 4\pi N_A r_e^2 m_e c^2 = 0.3070$ MeV cm^2/g. Z and A are the charge and mass numbers of the medium; I, δ, C, and ν are phenomenological functions. Frequently the values of δ, C and ν are negligibly small; I characterizes the binding of the electrons of the medium and can be approximated as $I \cong 16Z^{0.9}$ eV for $Z > 1$.

For monopoles and dyons this mean value for unit electric charge is modified by the factor $g^2\beta^2/e^2$ so that

$$\left\langle \frac{dE}{dx} \right\rangle = \left(\frac{g^2\beta^2 + q^2}{e^2} \right) \left\langle \frac{dE}{dx} \right\rangle_{BB} \qquad (3.6)$$

where $q = 0$ for monopoles. This scaling of the energy loss is due to an increase in the number of interactions per unit length, rather than an increase in the energy transfer per interaction which is constrained by two-body relativistic kinematics.

Figure 3.1 shows the dE/dx losses we would expect in the DC gas for various masses of monopole with unit magnetic charge. As can be seen from equation 3.6 the losses scale as $g^2\beta^2$ so that they will be considerably greater for monopoles of charge g. The reason for the drop in dE/dx for low momentum monopoles where normally there is a rise for electrically charged particles is the effect of the additional β^2 term. This can be seen in figure 3.2 where the fractional momentum loss due to ionization is plotted as a function of the momentum. This β^2 term also means that the fractional momentum loss decreases as the monopole mass increases for the whole momentum spectrum, as figure 3.2 clearly shows. Note also that for the complete mass range, $\langle dP/dx \rangle / P$ drops as the momentum increases above about 10 GeV/c. This effect is important as the monopoles are found to gain in total energy due to the magnetic field, so that our fractional momentum losses actually get less in the same medium the further we move through the detector.

Tuning the Equation used for Ionization Losses

As the ionization losses are crucial to this analysis it is important that the algorithm used is 'tuned' so that the losses match those expected for ordinary electrically charged particles in the range we are interested in (P $>$ 1.0 GeV/c). To do this we used the measured dE/dx in the JADE jet chamber [37], and compared this to our simulation with the correct gas mixture and pressure. Figure 3.3 shows the dE/dx in the JADE jet chamber and figure 3.4 shows our tuned algorithm with the dE/dx losses for both the JADE jet chamber and the TASSO DC. The main reason for the TASSO curve being lower than JADE's is that the DC was at 1 atmosphere whilst the jet chamber operated at 4 atmospheres.

3.3.2 Multiple Scattering

When traversing matter, a charged particle will interact with nuclei from the medium as well as electrons, and be scattered with a distribution given by the Rutherford scattering formula. A large number of scatters will give rise, via a random walk, to a mean square deflection $\langle \phi^2 \rangle$, which may be expressed as a function of the distance, dx, travelled

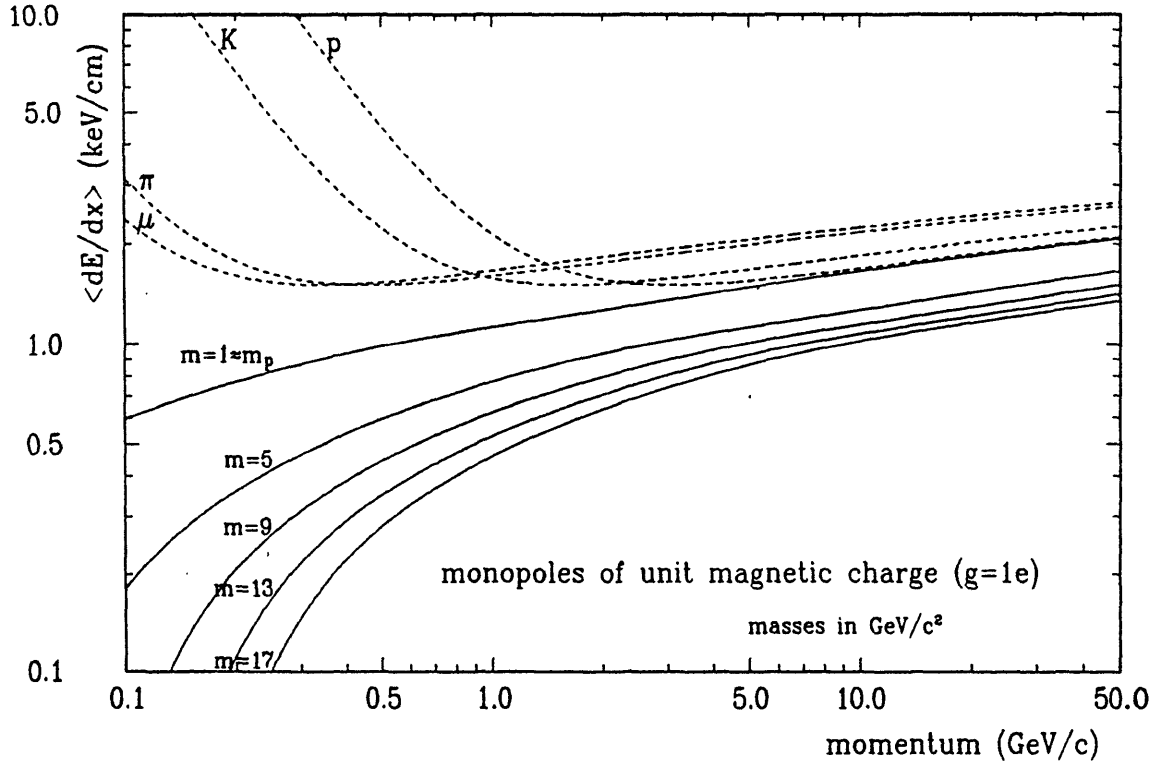


Figure 3.1: $\langle dE/dx \rangle$ *losses by ionization in DC for monopoles of unit magnetic charge.*

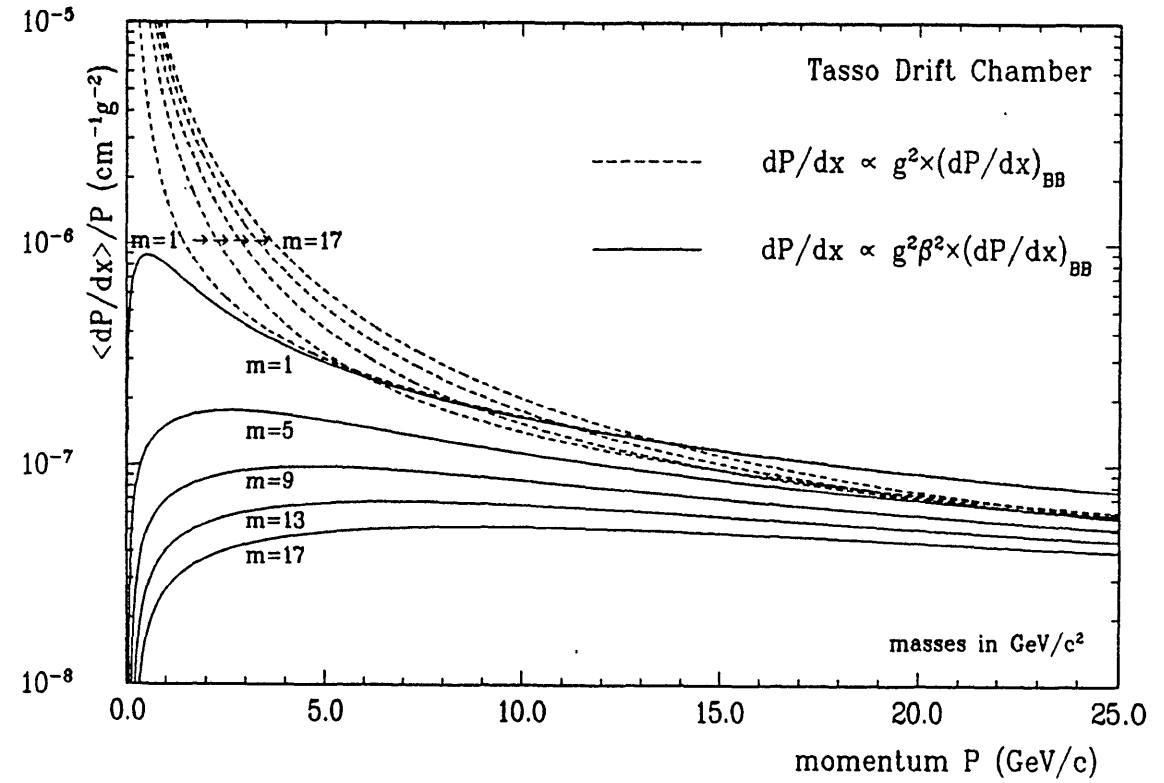


Figure 3.2: *Effect of* β^2 *term upon* $\langle dP/dx \rangle$ *for monopoles of unit magnetic charge.*

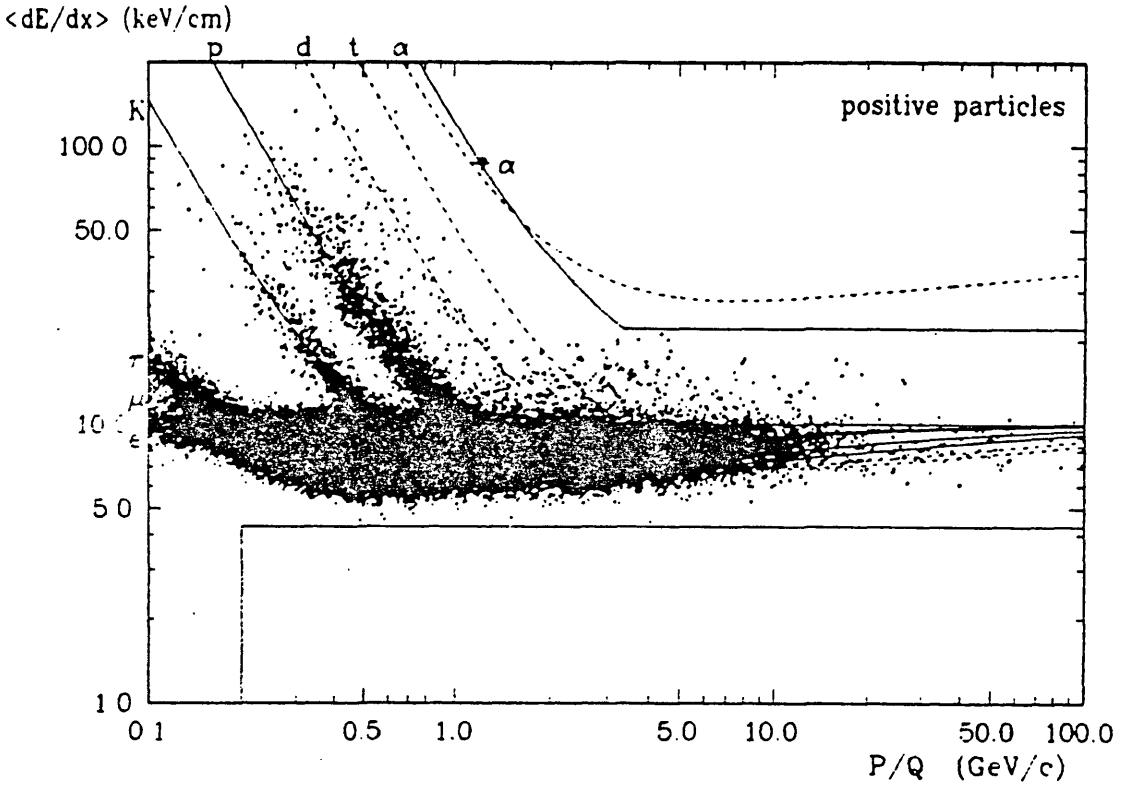


Figure 3.3: $\langle dE/dx \rangle$ *losses in* JADE *jet chamber.*

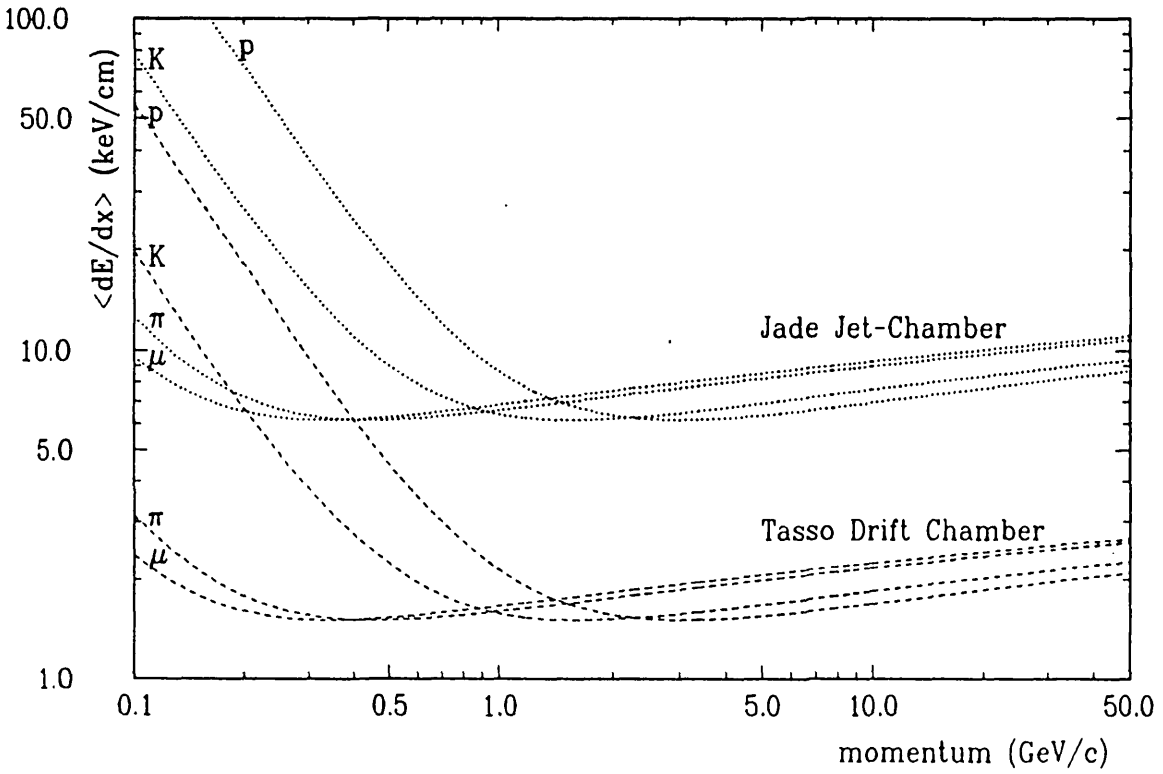


Figure 3.4: *Tuned dE/dx algorithm showing losses for* JADE *jet chamber and* TASSO DC.

through the medium [38]:

$$\left\langle \phi^2 \right\rangle_{q=ze} = \frac{dx}{X_0} \left(\frac{qE_s}{pe\beta c} \right)^2 \tag{3.7}$$

where $E_s = 21$ MeV and X_0 is the radiation length of the medium. Again, for magnetically charged particles, this is modified by a factor $g^2\beta^2/e^2$ [39] so that

$$\left\langle \phi^2 \right\rangle = \left(\frac{g^2\beta^2 + q^2}{e^2} \right) \left\langle \phi^2 \right\rangle_{q=1e} \tag{3.8}$$

Multiple scattering was performed by rotating the track vector at the end of each step by an angle from a positive Gaussian distribution of width $\langle \phi^2 \rangle$, the direction of rotation being random.

3.3.3 Bremsstrahlung

As well as interactions with the media's nuclei causing multiple scattering, the accelerations due to the scattering are expected to cause the monopoles to emit bremsstrahlung. By once again following the semi-classical approach of substituting q by $g\beta$ we expect that the energy radiated by a monopole of mass m is given by

$$\frac{dE}{dx}_{brem} = \frac{E}{X_0} \left(\frac{g^2\beta^2}{e^2} \right)^2 \left(\frac{m_e}{m} \right)^2 \tag{3.9}$$

In comparison to ionization losses, the effect of bremsstrahlung is in most cases small, despite the g^4 dependence. This is because for the monopoles we are simulating $m \gg m_e$.

3.4 Optimizing the Stepping Routine

As each new monopole position and momentum is calculated in discrete steps using equations 3.3 and 3.4 it is necessary that a single step should not have $\left(\frac{dp_x}{dX}\right)\Delta X$ too large otherwise this will destabilize the algorithm. Fortunately as this term is linear with ΔX all we need to do is alter the size of ΔX. However we would like to optimize the process to take as few iterations as possible whilst having ΔX as large as possible. Figure 3.5 shows a flowchart of how this is achieved. Each step is initialized to be $1\text{cm}/\beta$ in time and the total fractional momentum loss, $\langle dP/dx\rangle / P$, for both ionization losses and bremsstrahlung is integrated over all media which that step traverses. If $\langle dP/dx\rangle / P$ is found to be more than 0.25%, then if more than one medium was traversed ΔX is adjusted so just the first medium is traversed and $\langle dP/dx\rangle / P$ is recalculated. If this is still greater than 0.25% or only one medium was traversed initially then

$$\Delta X_{i+1} = \frac{\langle dP/dx\rangle \times 0.0025}{P_i}$$

so that the fractional loss is next calculated to be 0.25%. This way it never takes more than two iterations of ΔX to calculate a $\left(\frac{dp_x}{dX}\right)\Delta X$ small enough to keep the stepping algorithm stable. The fractional momentum loss is then subtracted from each of the old momentum components along with the change in momentum due to the magnetic field to calculate the new momentum components.

3.4.1 Smearing of dE/dx losses

Although there are theories for the average value of the energy loss due to ionization and bremsstrahlung (sections 3.3.1 and 3.3.3), there are none for the shape of the energy loss distributions. To find out, assuming a Gaussian energy loss distribution, whether the width of that Gaussian affects our monopole detection efficiencies (see section 6.3.3) we allowed our average dE/dx losses to be smeared by Gaussians of widths that were arbitrary but appreciable fractions of the average loss. Figure 3.6 shows a graphical representation of the result of this on the dE/dx losses by ionization.

An initial problem encountered was how to make the step size alteration, without biasing the dE/dx distribution by allowing large energy losses only when the step size

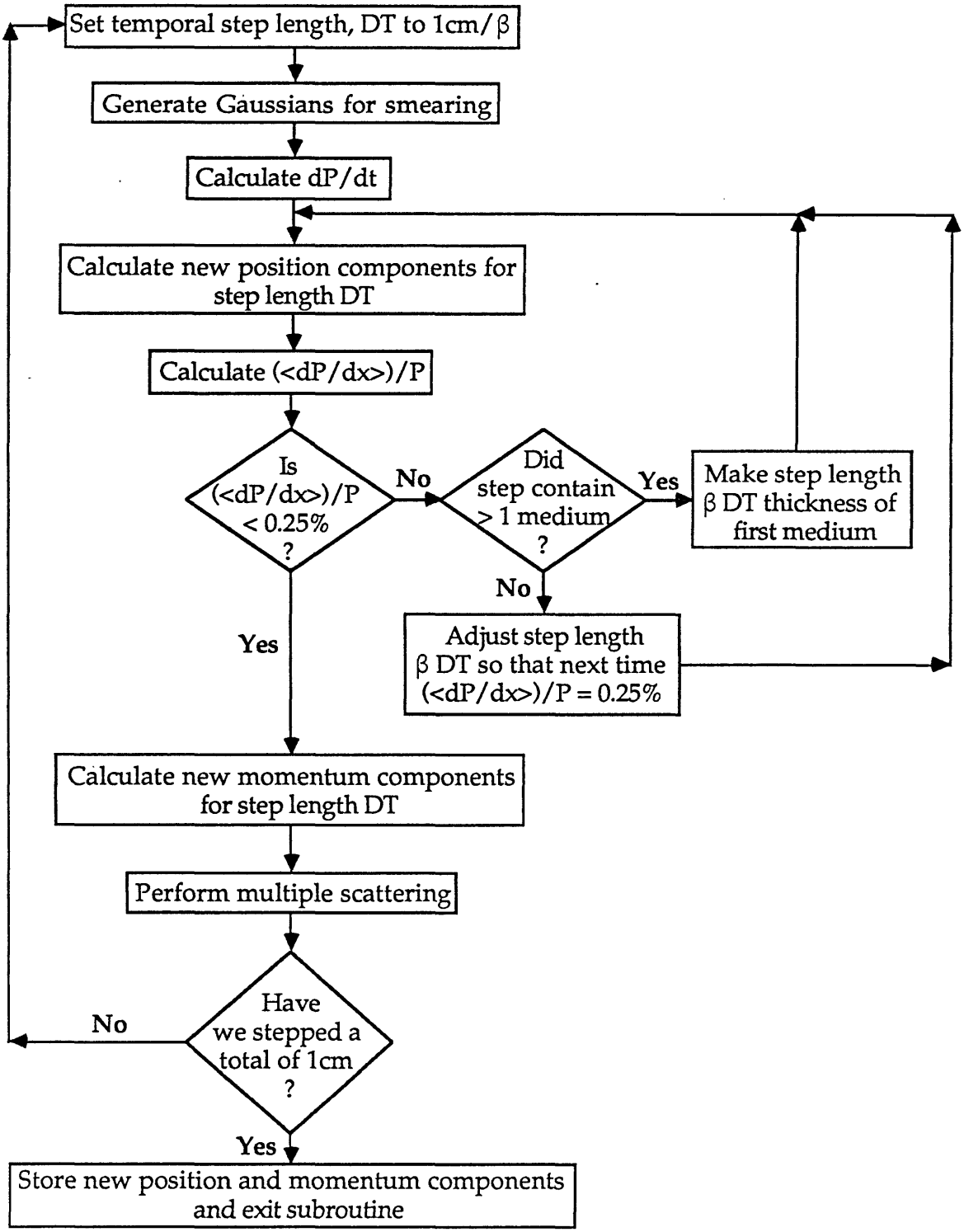


Figure 3.5: *Flowchart of stepping algorithm.*

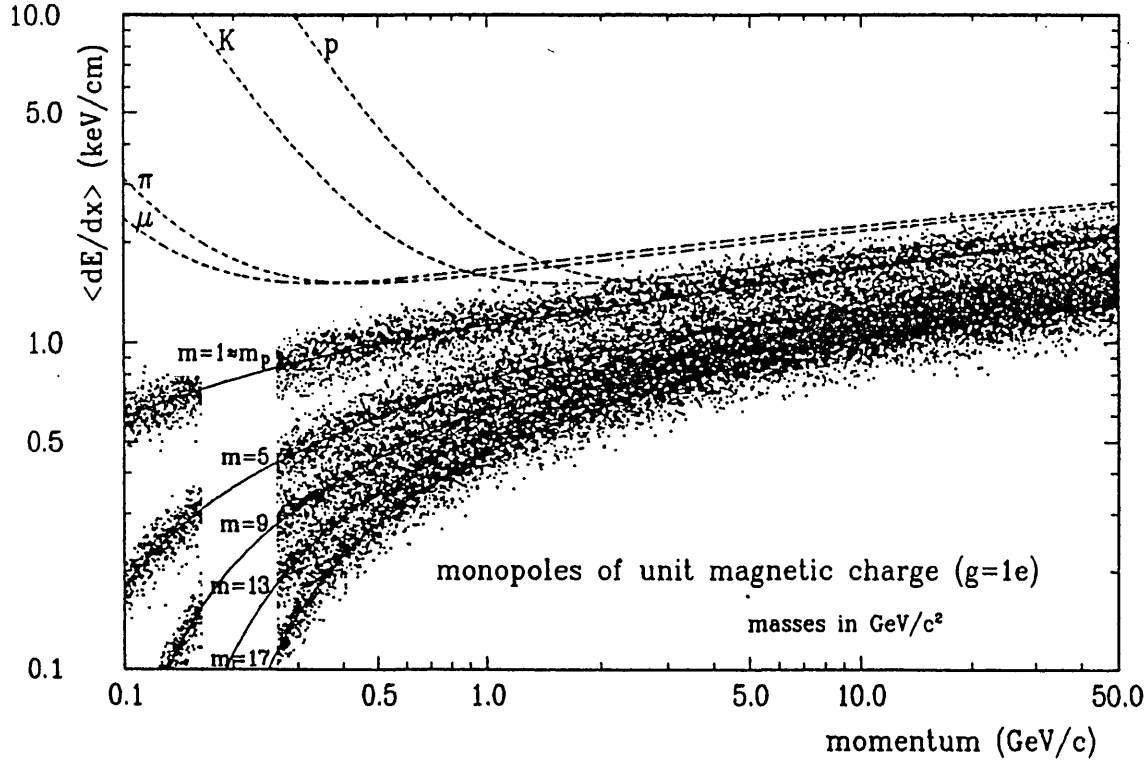


Figure 3.6: *Smeared dE/dx ionization losses in DC.*

was small enough whilst allowing small energy losses for any step size. This was solved by making the cut dependent upon the *average* fractional momentum loss rather than upon the *actual* fractional momentum loss, with a new Gaussian width being generated after each completion of a step (see figure 3.5). By including the Gaussian in our dE/dx losses, the *actual* fractional momentum loss will frequently be larger than the *average* fractional momentum loss upon which we are making the cut (section 3.4). To prevent the instabilities occurring now, we made our cut on the *average* fractional momentum loss small enough to account for this.

3.5 Simulating the Detector Materials

As the equations for the matter interactions of monopoles (equations 3.5, 3.7 and 3.9) are dependent on the atomic and nuclear properties of the materials the particle traverses, we need to know what materials make up the detectors the monopoles are likely to pass through before triggering.

Tables 3.1, 3.2 and 3.3 give a list of the materials to be found in the VXD [27], CPC [40] and DC [28] along with the inner radii at which they start and their radial lengths. In simulating TASSO's inner detector we have treated everything as being radially symmetrical. Beyond the outer layer of air in table 3.3 are the ITOFs which trigger the event when the monopoles reach them, so to speed things up they have not been included amongst the materials in the central detector.

Material	Inner Radius (cm)	Radial Length (cm)
Vacuum	0.0	6.6665
Copper	6.6665	0.0015
Beryllium	6.668	0.18
VXD Gas	6.848	0.648
Mylar	7.496	0.0125
Aluminium	7.5085	0.005
VXD Gas	7.5135	7.8865
Copper	15.4	0.003
Mylar	15.403	0.0125
Air	15.4155	0.5345
Aluminium	15.95	0.15
Air	16.1	0.69

Table 3.1: *Materials in the VXD.*

Material	Inner Radius (cm)	Radial Length (cm)
Aluminium	16.79	0.015
Polystyrene	16.805	1.19
Epoxy Resin	17.995	0.0215
Mylar	18.0165	0.2835
Copper	18.3	0.003
CPC Gas	18.303	1.1
Copper	19.403	0.003
Mylar	19.406	0.0135
Epoxy Resin	19.4195	0.0185
Polystyrene	19.438	1.19
Epoxy Resin	20.628	0.0185
Mylar	20.6465	0.0135
Copper	20.66	0.003
CPC Gas	20.663	1.796
Copper	22.459	0.003
Mylar	22.462	0.0135
Epoxy Resin	22.4755	0.0185
Polystyrene	22.494	1.19
Epoxy Resin	23.684	0.0185
Mylar	23.7025	0.0135
Copper	23.716	0.003
CPC Gas	23.719	1.796
Copper	25.515	0.003
Mylar	25.518	0.0135
Epoxy Resin	25.5315	0.0185
Polystyrene	25.55	1.19
Epoxy Resin	26.74	0.0185
Mylar	26.7585	0.0135
Copper	26.772	0.003
CPC Gas	26.775	1.7953
Copper	28.5703	0.003
Mylar	28.5733	0.0137
Epoxy Resin	28.587	0.0185
Polystyrene	28.6055	1.19
Epoxy Resin	29.7955	0.0185
Mylar	29.814	0.0135
Air	29.8275	2.1725

Table 3.2: *Materials in the CPC.*

Material	Inner Radius (cm)	Radial Length (cm)
Fibre Glass	32.0	0.5
DC Gas	32.5	13.149
Aluminium	45.649	0.001
Rohacell	45.65	0.4
Aluminium	46.05	0.001
DC Gas	46.051	17.898
Aluminium	63.949	0.001
Rohacell	63.95	0.4
Aluminium	64.35	0.001
DC Gas	64.351	11.848
Aluminium	76.199	0.001
Rohacell	76.2	0.4
Aluminium	76.6	0.001
DC gas	76.601	17.6472
Aluminium	94.2482	0.0008
Mylar	94.249	0.001
Rohacell	94.25	1.0
Mylar	95.25	0.001
Aluminium	95.251	0.0008
DC Gas	95.2518	11.1964
Aluminium	106.4482	0.0008
Mylar	106.449	0.001
Rohacell	106.45	1.0
Mylar	107.45	0.001
Aluminium	107.451	0.0008
DC Gas	107.4518	19.9482
Aluminium	127.4	0.6
Air	128.0	4.0

Table 3.3: *Materials in the DC.*

Table 3.4 gives the values for density, radiation length (X_0), atomic number (Z) and atomic weight (A) taken from [36], for all materials to be found in the central detector. For composite media, average values for Z and A were calculated by:

$$A = \sum_{i=1}^{n} \textit{fraction of species } i \textit{ in compound} \times \textit{atomic weight of species } i \tag{3.10}$$

$$Z = \sum_{i=1}^{n} \textit{fraction of species } i \textit{ in compound} \times \textit{atomic number of species } i \tag{3.11}$$

To calculate the radiation length of composite media the following prescription was used [41]:

$$\frac{1}{X_0} = \sum_{i=1}^{n} \frac{\textit{fraction of species } i \textit{ in compound}}{X_0 \textit{ of species } i} \tag{3.12}$$

Here X_0 is in g/cm^2 so that it is independent of the state of the material. For our purposes X_0 is converted to cm by multiplying by the density of the material in the state that it is in the detector.

Material	Density (g/cm^3)	Radiation Length (cm)	Atomic No. (Z)	Atomic Wt. (A)
Air	1.20×10^{-3}	3.04×10^4	7.36	14.78
Aluminium	2.70	8.89	13.0	26.98
Beryllium	1.85	35.3	4.0	9.01
Copper	8.96	1.43	29.0	63.54
Epoxy Resin	1.20	33.33	3.5	6.51
Fibre Glass	1.70	19.4	7.4	14.62
VXD Gas	5.34×10^{-3}	3.74×10^3	17.47	38.69
CPC Gas	2.00×10^{-3}	1.14×10^4	14.12	31.0
DC Gas	1.57×10^{-3}	1.84×10^4	10.12	21.86
Mylar	1.39	28.7	4.55	8.74
Polystyrene	1.88×10^{-2}	2.33×10^3	3.5	6.5
Rohacell	3.00×10^{-2}	2.00×10^3	2.67	4.67
Vacuum	0.0	0.0	0.0	0.0

Table 3.4: *Atomic and nuclear properties of materials found in central detector*

3.6 Tuning the Monte Carlo to the 1986 Data

As well as tracking the particles as they traverse the detector, the Monte Carlo must be able to simulate the performance of the components that are involved in the data taking for this analysis. It is therefore necessary to have these components 'tuned' in the Monte Carlo to the same level of performance as pertained during the data taking period of 1986. For our data we relied almost entirely on hits in the DC and so the tuning of the detector is confined to the performance of the DC sense wires. To get a picture of the general performance of the DC over the data-taking period of 1986, we took two-prong events from runs spread across the whole period and tuned the Monte Carlo to them.

3.6.1 DC Sense Wire Residual Tuning

When liberated electrons from an ionizing particle drift to a sense wire there will be a spread in the arrival time registered and therefore in the assigned hit position. This is a function of many things such as the drift time in the chamber gas, electronics, angle of track to cell and so on. It will manifest itself as a width to an approximate Gaussian distribution when plotting residuals. A residual is the difference between the assigned hit position and fitted track along the drift path. The Monte Carlo simulates this by multiplying the drift distance it calculates with a Gaussian distribution of a tuneable width so as to get the residuals to match those of the data. We tuned these widths to the 1986 data by simply plotting the residual distribution for each layer and altering the Gaussian widths until the distributions were found to match for each layer.

Table 3.5 shows the widths in cm that were used in the Monte Carlo. The resolutions for the DC axial layers are quoted as 0.022 – 0.027 cm or 220 – 270 μm [28]. Actual resolutions for DCα layers are found by dividing the axial resolution by the tangent of the stereo angle. Figure 3.7 shows the residuals for 1986 Bhabha events and the tuned Monte Carlo for two DC0 layers and two DCα layers. It is not possible to take the resolution directly from the distributions as the effects of the track finding are folded into these distributions. Although this is not a precise way to find the chamber's resolutions, the method is accurate enough for our purposes.

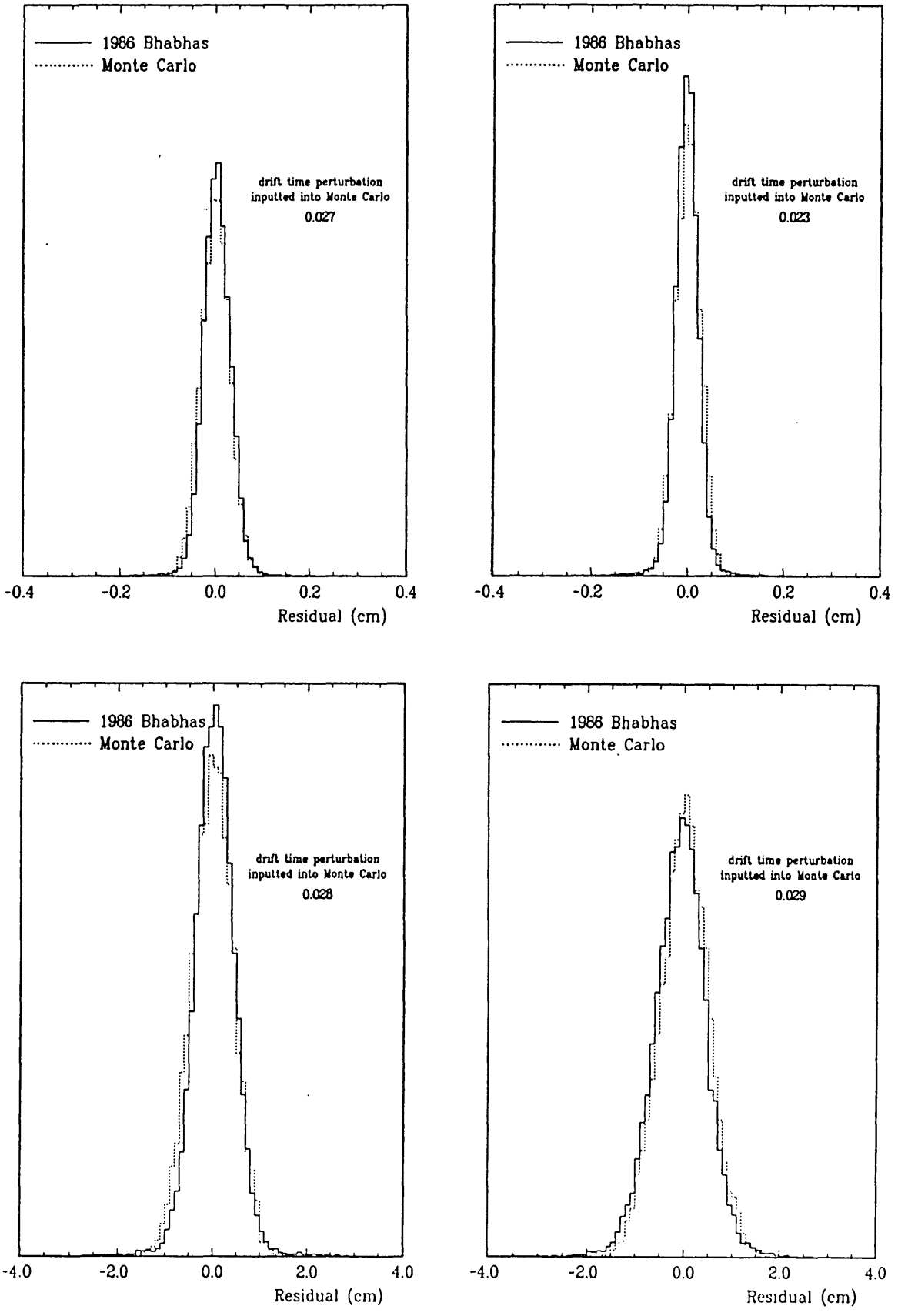


Figure 3.7: *Residual distributions for two DC0 layers and two DCα layers. From left-to-right and top-to-bottom the layers are: DC0 4, DC0 7, DCα 4, DCα 5.*

Layer	DC0 1	DC0 2	DC0 3	DC0 4	DC0 5	DC0 6	DC0 7	DC0 8	DC0 9
MC input	0.022	0.023	0.027	0.028	0.026	0.026	0.023	0.024	0.023

Layer	DCα 1	DCα 2	DCα 3	DCα 4	DCα 5	DCα 6
MC input	0.022	0.026	0.025	0.028	0.029	0.028

Table 3.5: *DC sense wire resolutions tuned to 1986 data*

3.6.2 DC Sense Wire Efficiency Tuning

It is important that we can simulate the efficiencies of the DC sense wires during the data taking period as inefficiencies in any layers will affect the track finding and therefore our ability to detect monopoles.

Efficiencies for each DC layer were found by studying Bhabha tracks that exited through the barrel of the DC, so that we knew the particle passed through each DC layer, and seeing whether a hit on the track had been attributed to that layer. To unfold the track finding efficiency, we analysed Monte Carlo two-prong events with 100% hit efficiency in exactly the same way and took the efficiency of the layer to be

$$\frac{\textit{fraction of Bhabha tracks with hit on track}}{\textit{fraction of 100\% efficiency Monte Carlo tracks with hit on track}}$$

which was then included in the Monte Carlo. During the 1986 data taking runs DCα layer 4 was found to be particularly inefficient and upon investigation, it was found that a large region of this layer was dead for most of the year. This was simulated by killing off the corresponding wires in the Monte Carlo. This is shown in figure 3.8 which clearly shows the dead region when comparing DCα layers 3 and 4. Any discrepancy between the real data and Monte Carlo for this layer (such as the fact that there is some data to be found in the region we have simulated as dead, possibly from runs early in the year) is compensated by the value that is found for inclusion in the Monte Carlo.

Table 3.6 shows the values we found for the 1986 Bhabhas and 100% efficiency Monte Carlo, as well as the efficiency values included in the Monte Carlo. Looking at this table we see, for instance, that for DC0 layer 9, the poor efficiency seen in the Bhabhas was due to track finding inefficiencies whilst for DC0 layer 8, the layer is seen to be truly inefficient. Also, we see that outside the dead region, DCα layer 4 is as efficient as any of the others. Figure 3.9 shows the efficiencies found from Monte Carlo events after putting in the values of table 3.6 and we see how well these match the 1986 Bhabha data.

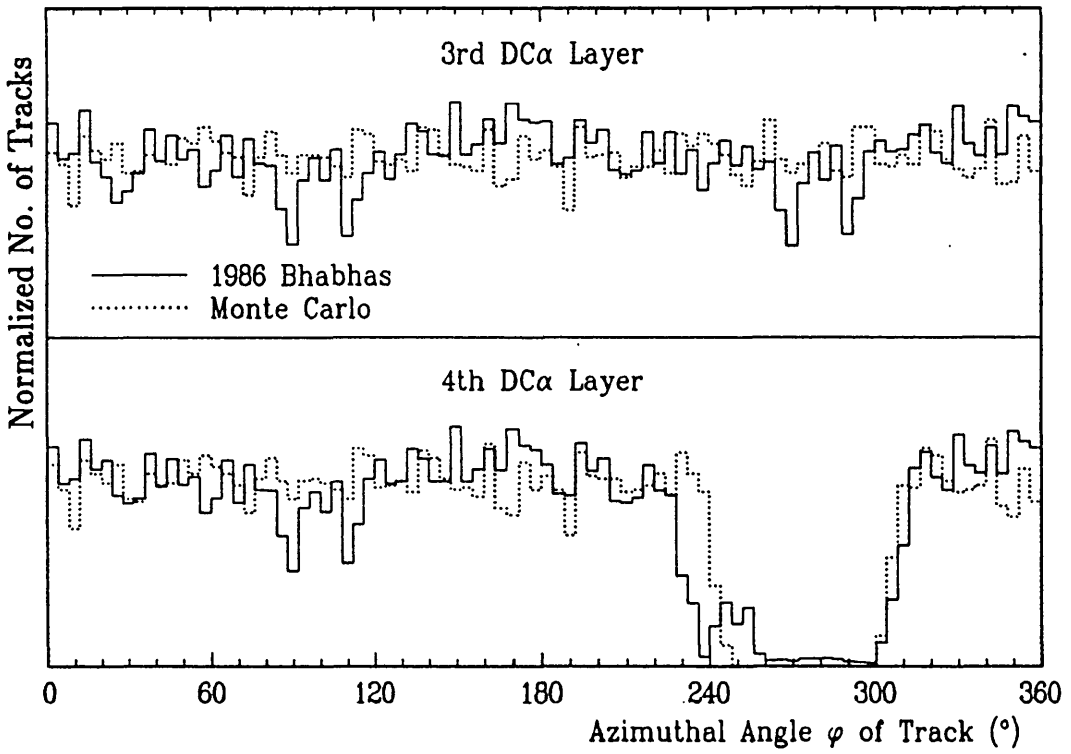


Figure 3.8: *Simulation of dead region in DCα layer 4.*

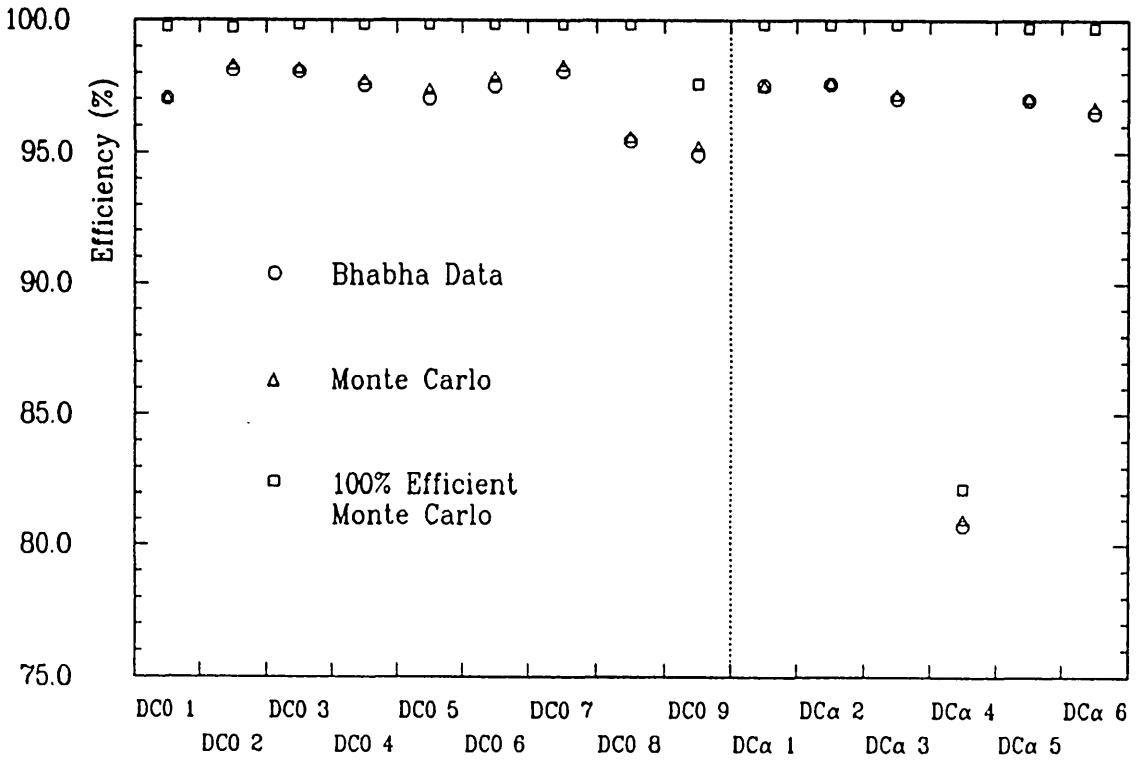


Figure 3.9: *DC sense wire efficiencies found for 1986 data.*

Layer	DC0 1	DC0 2	DC0 3	DC0 4	DC0 5	DC0 6	DC0 7	DC0 8	DC0 9
Bhabhas	0.970	0.981	0.980	0.975	0.970	0.975	0.980	0.954	0.949
MC 100%	0.997	0.997	0.998	0.998	0.998	0.998	0.998	0.998	0.975
MC input	0.973	0.984	0.982	0.977	0.972	0.977	0.982	0.956	0.974

Layer	DCα 1	DCα 2	DCα 3	DCα 4	DCα 5	DCα 6
Bhabhas	0.975	0.975	0.970	0.807	0.970	0.965
MC 100%	0.999	0.998	0.998	0.822	0.997	0.997
MC input	0.976	0.977	0.972	0.982	0.973	0.968

Table 3.6: *DC sense wire efficiencies tuned to 1986 data*

3.6.3 Event Vertex Tuning

Although not a component of the detector, the spread and position of the event vertex are experimental parameters arising from the performance of PETRA itself during the 1986 data taking period. The event vertex is important in calculating our detection efficiencies as we make vertex cuts in our data reduction and so it also needs to be tuned to monitor the effect of these cuts. The values used in the Monte Carlo generation stage are shown in table 3.7 and were in fact obtained from an analysis of the beamspot at TASSO for the 1986 data taking period [42]. Note that $d_0 = \sqrt{d_x^2 + d_y^2}$. It was found that varying the value of σ_z had little effect on the z_0 distribution of the Monte Carlo tracks. This was mainly due to the size of the hit resolution in the $s - z$ view, and the fact that there were no z hits between the DC and interaction point, which would swamp the effect of the width of the z vertex position in the track finding. As such we did not attempt to tune rigorously this parameter.

σ_x (cm)	σ_y (cm)	σ_z (cm)
0.0325	0.0086	0.5

d_x (cm)	d_y (cm)
0.6	0.12

Table 3.7: *Vertex parameters tuned to 1986 data*

Chapter 4

Track Finding of Particles in Magnetic Fields

As magnetically charged particles are accelerated in the magnetic field of TASSO, their trajectories are going to be different to those of non-magnetic particles. This means that the standard track finders used in TASSO will be inadequate for finding the tracks left by magnetically charged particles. To be able to adapt a track finder to our purpose we need to know the trajectories that magnetically charged particles are likely to take.

4.1 Motion of Particles Influenced by a Magnetic Field

Let us begin by looking at the general motion of a particle influenced by a magnetic field. As already explained in section 3.2 the general equation of motion for a particle possessing both electric and magnetic charge in a magnetic field is

$$\frac{d\mathbf{p}}{dt} = g\mathbf{B} + q\mathbf{p} \times \mathbf{B}/\gamma m \tag{4.1}$$

In the case of TASSO where we can assume a uniform magnetic field B in z, the components of motion become

$$\begin{aligned} \frac{dp_x}{dt} &= qp_yB/\gamma m \\ \frac{dp_y}{dt} &= qp_xB/\gamma m \\ \frac{dp_z}{dt} &= gB \end{aligned} \tag{4.2}$$

We see that for this case, regardless of any force on the particle in z, the magnitude of the tranverse momentum component $p_\perp^2$ in the $r-\phi$ plane is constant, where $p_\perp^2 = p_x^2 + p_y^2$, as

$$\frac{dp_\perp^2}{dt} = 2\left(p_x\frac{dp_x}{dt} + p_y\frac{dp_y}{dt}\right) = 0$$

The consequence of this for track finding is that a circle fit is used when searching in the $r-\phi$ plane, irrespective of whether the particle possesses electric and/or magnetic charge.

4.1.1 Motion of a Particle with Electric Charge

For a particle possessing just electric charge the Lorentz equation of motion is simply (compare with equation 4.1)

$$\frac{d\mathbf{p}}{dt} = q\mathbf{p} \times \mathbf{B}/\gamma m \tag{4.3}$$

As the magnetic field does not act on the particle in its axial plane, $dp_z/dt = 0$, resulting in the distance travelled in z being directly proportional to time t, so that

$$z = z_0 + v_{z_0}t \tag{4.4}$$

where γ remains constant. Equations 4.2 are satisfied by a solution of the form

$$\begin{aligned} x &= R\sin\omega t \\ y &= R\cos\omega t \end{aligned} \tag{4.5}$$

This means that the trajectory of an electrically charged particle in a solenoidal magnetic field is a helix [36] with pitch angle λ, radius R, and angular velocity ω where

$$p(\mathrm{GeV/c})\cos\lambda = 0.299979qB(\mathrm{Tesla})R(\mathrm{m}) \tag{4.6}$$

and

$$\omega(\mathrm{rad\ sec^{-1}}) = \frac{8.98755\times 10^7 qB(\mathrm{Tesla})}{E(\mathrm{GeV})} \tag{4.7}$$

For the solution given by equations 4.5, ω is related to the distance travelled in the $r-\phi$ plane, $s = \int\sqrt{dx^2+dy^2}$, by

$$\frac{ds}{dt} = \omega R \tag{4.8}$$

By defining

$$p_\perp = \gamma m\frac{ds}{dt} \tag{4.9}$$

and

$$p_{z_0} = \gamma m v_{z_0} \tag{4.10}$$

we calculate that the $s - z$ parameterization of the trajectory from equation 4.4 is

$$z = z_0 + s \tan\lambda \tag{4.11}$$

where

$$\tan\lambda = \frac{p_{z_0}}{p_\perp} \tag{4.12}$$

This is the standard linear relationship used in fitting tracks in $s - z$.

4.1.2 Motion of a Non-Relativistic Particle Possessing Magnetic Charge

For the non-relativistic limit, since $\gamma \to 1$, there is no coupling between the transverse and axial components of equations 4.2. This means that the transverse motion of the particle in the $r - \phi$ plane has the same solutions (equations 4.5) as for the purely electrically charged particle. In the case of monopoles which possess no electric charge we can see from equation 4.6 that the trajectory is that of a circle with an infinite radius - a straight line. This is clearly correct when we consider that the magnetic field does not act transversely on a monopole, thereby exerting no force to accelerate the monopole in this plane. For a dyon, possessing both electric and magnetic charges, the consequence is that it is indistinguishable from an electrically charged particle when tracked in this plane.

In the z direction there is now an acceleration caused by the force of the magnetic field on the magnetic charge:

$$\frac{dv_z}{dt} = gB/m \tag{4.13}$$

With this additional force the analogous form of equation 4.4 becomes

$$z = z_0 + v_{z_0} t + \frac{1}{2}\frac{gB}{m} t^2 \tag{4.14}$$

Again using the definitions of equations 4.9 and 4.10 where $\gamma \to 1$, we now find that the $s - z$ parameterization becomes

$$z = z_0 + s \tan\lambda + s^2 C \tag{4.15}$$

where $\tan\lambda$ is as before in equation 4.12 and

$$C = \frac{mgB}{2p_\perp^2} \tag{4.16}$$

The trajectory has now become that of a parabola.

4.1.3 Motion of a Relativistic Particle Possessing Magnetic Charge

In the case of where we are dealing with relativistic particles, the $s-z$ parameterization becomes more complicated as γ can no longer be treated as being constant. Despite this, as already explained, $p_\perp$ does remain constant so that the $r-\phi$ trajectory is still that of a circle.

To find the $s-z$ parameterization [43] we need to solve the equations

$$\frac{ds}{dt} = \frac{p_\perp}{\gamma m} \tag{4.17}$$

$$\frac{dz}{dt} = \frac{p_z}{\gamma m} \tag{4.18}$$

where γ is defined as

$$\gamma = \sqrt{1 + \frac{p^2}{m^2}} \tag{4.19}$$

Integrating the z component of equations 4.2, substituting into equation 4.18 and integrating this, we get

$$z = a\sqrt{1 + \frac{t_1^2}{a^2}} - ad \tag{4.20}$$

where

$$a = \frac{\sqrt{m^2 + p_\perp^2}}{gb} \qquad d = \sqrt{1 + \frac{p_z^2}{m^2 + p_\perp^2}} \qquad t_1 = t + \frac{p_{z_0}}{gb}$$

and

$$b = \frac{p_\perp}{gB}$$

Substituting the other components of equations 4.2 in the form of $p_\perp$ into equation 4.18 and integrating gives

$$s = b \ln\left(\frac{t_1/a + \sqrt{1 + t_1^2/a^2}}{D}\right) \tag{4.21}$$

where in addition

$$D = d + \sqrt{(d^2 - 1)}$$

Eliminating t_1 from equations 4.20 and 4.21 we get an $s-z$ parameterization for relativistic monopoles and dyons:

$$e^{s/b} = \frac{\sqrt{(z/a + d)^2 - 1} + z/a + d}{D} \tag{4.22}$$

In practice this takes no account of the matter interactions described in section 3.3 which result in deviations from the parameterization of equation 4.22 and in fact the non-relativistic parameterization of equation 4.15 is found to be adequate in finding $s - z$ tracks from monopoles as will be shown in section 4.2.4

4.2 Track Finding using FELIX

The track finder adapted to search for parabolic tracks in $s-z$ was FELIX [27], which employs the backtracking method [44] to find tracks that pass through the VXD, CPC and DC. The backtracking method is briefly described below for finding tracks in the $r-\phi$ and $s-z$ projections. For a more complete description see reference [27].

4.2.1 Track Finding in $r-\phi$

A track is firstly searched for in the $r-\phi$ plane by taking all hits in the outermost layers to be candidates for the first hit in the track. Appendix B explains how the co-ordinates for these hits are calculated. Each hit is taken sequentially and placed in a partial track array. Hits from the next layer are then taken in turn and a circle fit is made from all the hits in the partial track array. If the fitted track passes various criteria then the track is extrapolated into the next sense wire plane and hits found within a certain distance of the extrapolated track are stored as possible next hit candidates. If no hits are found or none or these hits pass the criteria when fitted with a circle, then the last hit in the partial track array is removed, and another candidate from that layer is used instead to extrapolate the track into the next layer. If all the candidate hits from a particular layer have been exhausted then the partial track is shortened and the search proceeds from the previous layer. A track is found when the innermost layer is reached and the fitted track passes all the criteria for the track. These criteria are to be found in reference [27]. Once a track has been found in the $r-\phi$ plane all the hits belonging to that track and their mirror hits are masked out, so that the search can carry on finding further tracks in $r-\phi$ amongst the remaining hits.

Hits from the 9 axial layers of the DC and the 4 sense wire layers of the CPC were used in the reconstruction of $r-\phi$ tracks. Hits from the 8 sense wire layers of the VXD were not used in this analysis as it was found from Monte Carlo studies that it gave no benefit to the analysis and was very time consuming.

4.2.2 Track Finding in $s-z$

Once a track has been found in $r-\phi$ the projection of this track in $s-z$ is searched for. The s and z co-ordinates for all DCα hits that may belong to the track are calculated as outlined in appendix B and stored. The finding of the track is very much the same as for $r-\phi$ except that instead of a circle fit being performed, a parabolic fit is made instead. As explained in section 4.1.1, a linear fit is normally made in $s-z$. This is done using a least squares method, to find the parameters of the fitted straight line from the input hit co-ordinates. The parabolic fit was done using a more complicated least squares method, which is shown in table 4.1.

$$z = z_0 + s\tan\lambda + s^2 C$$

$$\begin{aligned} z_0 &= V_{11}\Sigma y + V_{12}\Sigma xy + V_{13}\Sigma x^2 y \\ \tan\lambda &= V_{21}\Sigma y + V_{22}\Sigma xy + V_{23}\Sigma x^2 y \\ C &= V_{31}\Sigma y + V_{32}\Sigma xy + V_{33}\Sigma x^2 y \end{aligned}$$

where

$$\begin{aligned} V_{11} &= (\Sigma x^4\Sigma x^2 - \Sigma x^3\Sigma x^3)/D \\ V_{12} = V_{21} &= (\Sigma x^2\Sigma x^3 - \Sigma x^4\Sigma x)/D \\ V_{13} = V_{31} &= (\Sigma x^3\Sigma x - \Sigma x^2\Sigma x^2)/D \\ V_{22} &= (\Sigma x^4\Sigma - \Sigma x^2\Sigma x^2)/D \\ V_{23} = V_{32} &= (\Sigma x^2\Sigma x - \Sigma x^3\Sigma)/D \\ V_{33} &= (\Sigma x^2\Sigma - \Sigma x\Sigma x)/D \end{aligned}$$

and

$$\begin{aligned} \Sigma &= \textstyle\sum_{i=1}^{n} 1/\sigma_i^2 \\ \Sigma x &= \textstyle\sum_{i=1}^{n} s_i/\sigma_i^2 \\ \Sigma y &= \textstyle\sum_{i=1}^{n} z_i/\sigma_i^2 \\ \Sigma x^2 &= \textstyle\sum_{i=1}^{n} s_i^2/\sigma_i^2 \\ \Sigma xy &= \textstyle\sum_{i=1}^{n} s_i z_i/\sigma_i^2 \\ \Sigma x^3 &= \textstyle\sum_{i=1}^{n} s_i^3/\sigma_i^2 \\ \Sigma x^2 y &= \textstyle\sum_{i=1}^{n} s_i^2 z_i/\sigma_i^2 \\ \Sigma x^4 &= \textstyle\sum_{i=1}^{n} s_i^4/\sigma_i^2 \\ D &= \Sigma x^4(\Sigma x^2\Sigma - \Sigma x\Sigma x) + 2\Sigma x^3\Sigma x^2\Sigma x - \Sigma x^3\Sigma x^3\Sigma - \Sigma x^2\Sigma x^2\Sigma x^2 \\ \sigma_i &= \text{resolution of hit } i \end{aligned}$$

Table 4.1: *Parabolic fit using least squares method*

As at least three points are required to define a parabola, the nominal event vertex was used in the fit when starting the search using hits from the two outermost layers. With the event vertex included at this point we can fit a parabola that can be extrapolated into the next DCα layer so as to search for the next candidate hit. As the search is for

the $s-z$ projection of the $r-\phi$ track already found, only one track is searched for, and once found the track finding returns to the $r-\phi$ search to find the next track.

Inclusion of Nominal Event Vertex in Fit

Only the hits from the DCα layers were used when reconstructing tracks in $s-z$ as information from the CPC cathode strips and the VXD charge division layers was not available during the 1986 data-taking period. With no hit information in this projection from $r = 0 \rightarrow r = 43$ cm, about a third of the total track length in the inner detector, it was found to be desirable to include the nominal event vertex throughout the fit as it was found that without it the z_0 distribution was flat. With the vertex included the z_0 distribution became approximately a Gaussian centred at $z = 0$.

4.2.3 Performance of Parabolic $s-z$ Track Finder on Particles without Magnetic Charge

The track finder was run on Bhabhas and muons taken during 1986 to see how the parabolic fitting would perform on straight tracks taken with the detector as configured for the analysis. Figures 4.1 show examples of the parabolic fit being applied to straight tracks in $s-z$, compared with a straight line fit on the same tracks. As well as the z_0 distribution being an approximate Gaussian, the distribution of the curvature coefficient C, (see equations 4.15 and 4.16) was also found to approximate a Gaussian centred at $z = 0$ (shown in figure 4.4). The $\tan\lambda$ values were found to be equal and opposite in each two-prong event indicating that the tracks were back-to-back.

Effect of Event Vertex Weighting in Fit

A study of the effect of varying the vertex weighting was made upon the muon data. It was found that the width of the z_0 distribution decreased as the vertex weighting increased. The distribution in C was found to decrease to a minimum as the weighting increased, remaining at that value as the weighting was increased further. This indicated that by including the vertex we were not producing the undesirable effect of causing

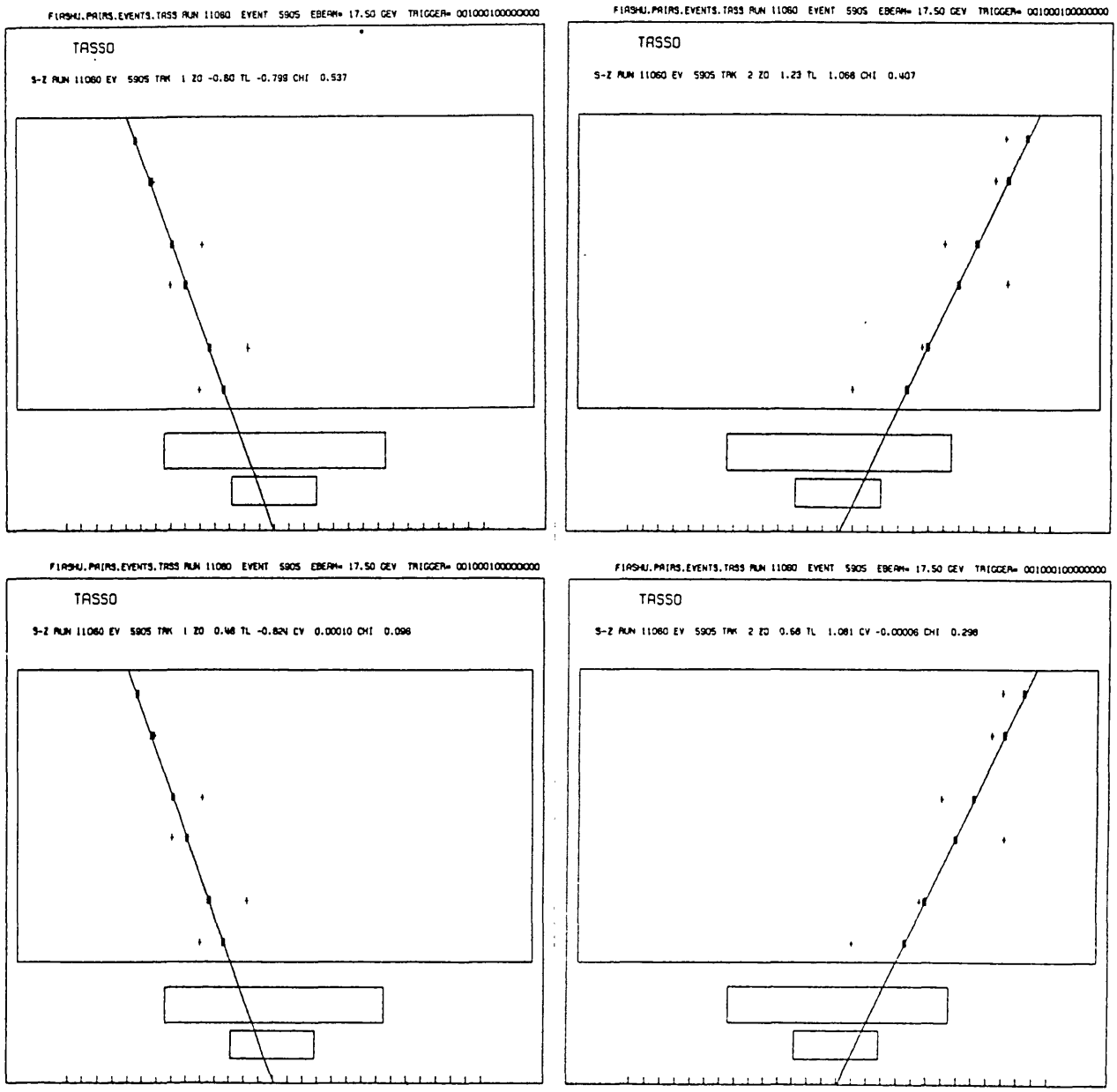


Figure 4.1: *Example of parabolic and straight line fits on straight tracks. The upper examples are the straight line fits and the lower examples the parabolic fits to the same tracks. The bold points are hits that have been fitted to the tracks shown, whilst the other points are the mirror hits associated with the track hits.*

straight tracks to appear curved, for two-prong events produced in TASSO during the 1986 runs. A weighting corresponding to a resolution of the vertex of 1.85 cm was chosen. The effect of varying the vertex constraint upon the efficiency with which we were able to detect monopole events is examined in section 6.3.4

4.2.4 Performance of Parabolic $s-z$ Track Finder on Particles with Magnetic Charge

The track finder was tested on simulated monopoles of various mass and magnetic charge combinations to see how effective the parabolic fit is. Figures 4.2 and 4.3 show examples of the track finding in both the $r-\phi$ and $s-z$ projections. In $r-\phi$ we can clearly see that in both cases the tracks are straight, as expected. In $s-z$ where the parabolic fit is an approximation of the trajectory we see that for the lower charged monopoles the tracks have been well fitted as indicated by the χ^2/n.d.f. values of the fit, 'CHI'. For the higher charged monopole, which is in fact a Dirac monopole, the performance of the fit is not so good, as indicated by the χ^2/n.d.f. value. Although the track does not fit the hits too well, it has done well enough for the tracks to be clearly identified. The probable reason for the parabolic fit being so robust even in the cases where the particles are deviating quite appreciably from a parabola is that the fit is only to a limited number of points, six plus the vertex. This allows the fit to pick up most curving trajectories of a quadratic nature, whether they are actually parabolic or not.

The z_0 distributions were found to be approximate Gaussians, as expected. The $\tan\lambda$ values were found to be equal and opposite in each event as was the case in the non-magnetic events indicating that the tracks were emitted from the vertex back-to-back, as $\tan\lambda$ in the parabolic parameterization is the angle of emission at the event vertex. The C values were found to also be roughly equal and opposite indicating that the particles were being curved in opposite senses as their magnetic charges were opposite in sign. The C distributions for two sets of simulated monopoles are shown in figure 4.4 along with the C distribution for the 1986 Bhabhas for comparison. As can be seen from figure 4.4 the curvature coefficients of magnetically charged particles depend on their mass – magnetic charge combinations, and so whilst some combinations will have high values of C relative to the magnetically neutral background others will have values that will merge into the C distribution of the background.

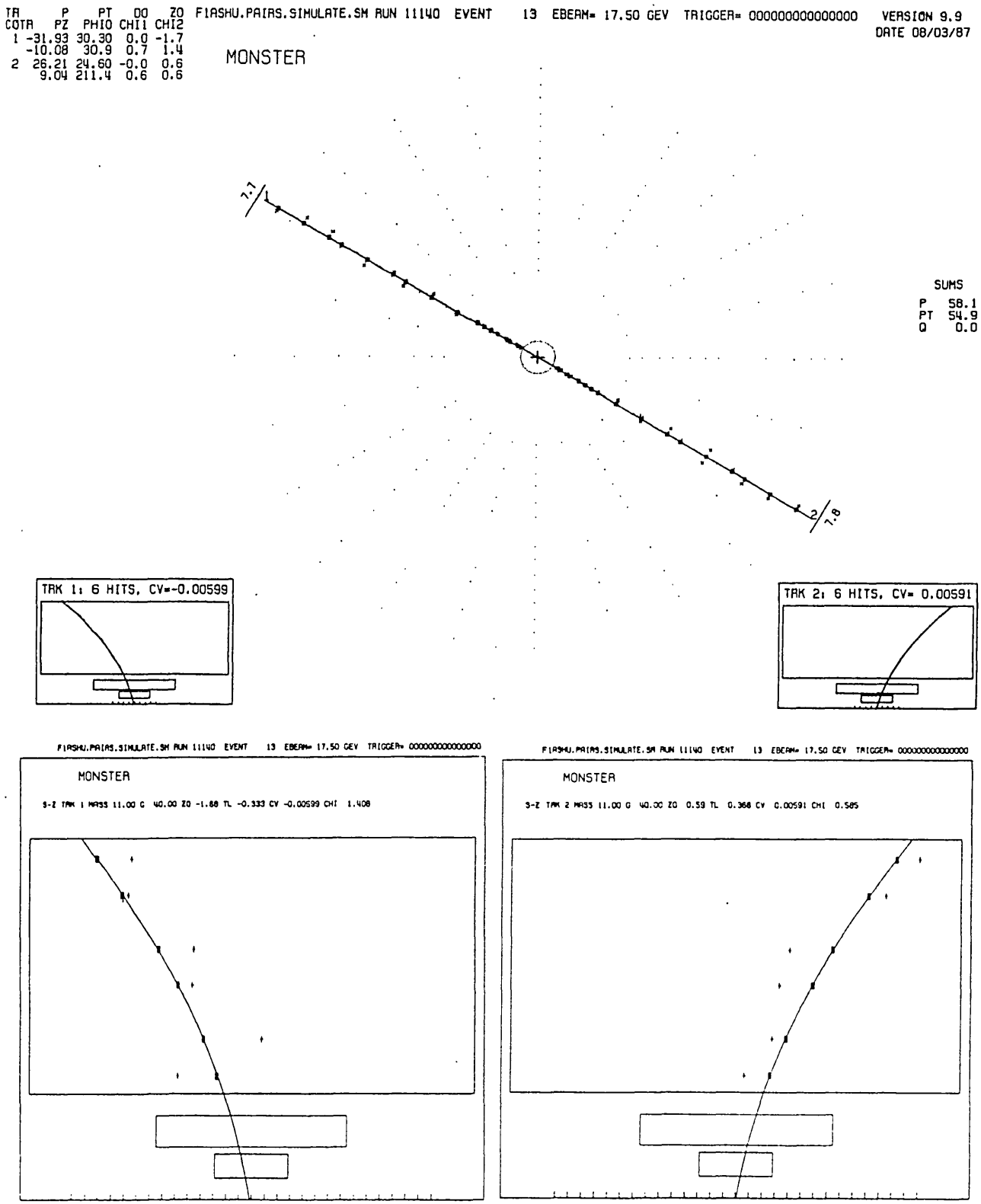


Figure 4.2: *Simulated monopole event with mass 11 GeV/c^2 and charge $g = 40e$. At the top we show the $r - \phi$ view and below the $s - z$ views of the two tracks as fitted with parabolæ where z is horizontal. In the $r - \phi$ view, only the DC0° hits are shown.*

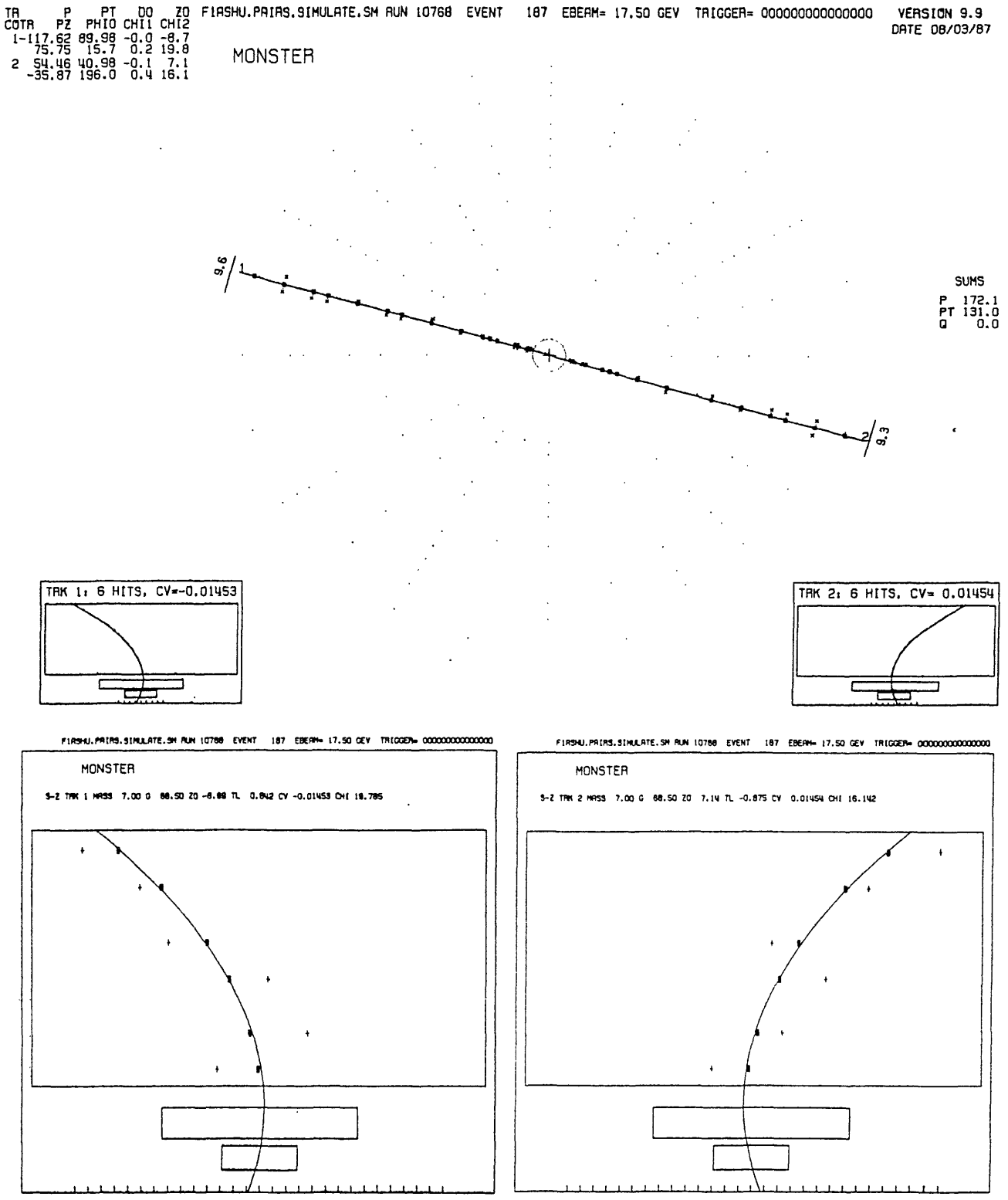


Figure 4.3: *Simulated monopole event with mass 7 GeV/c^2 and charge $g = \frac{137}{2}e$, a Dirac monopole.*

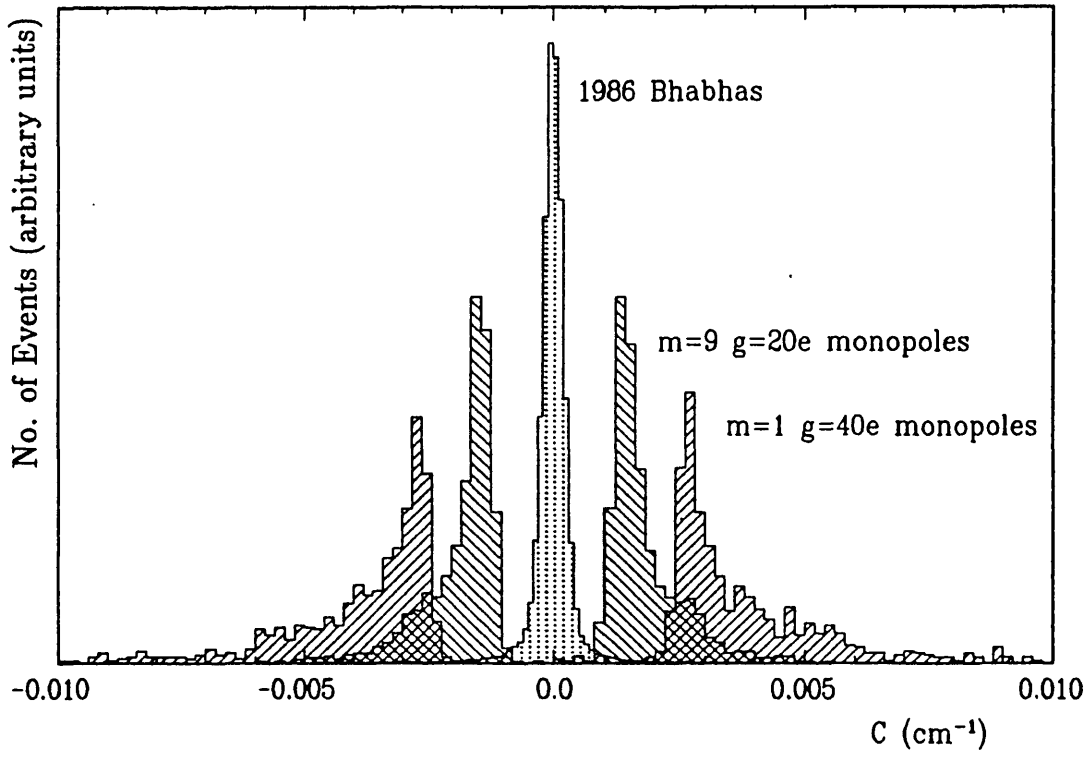


Figure 4.4: *C distributions from the parabolic fit in $s-z$ for the 1986 Bhabhas and two sets of simulated monopoles.*

In conclusion it can be seen that the parabolic track finder in $s-z$ is adequate to find tracks produced by both magnetically charged and magnetically neutral particles, with the indication that these classes of events are distinguishable by the comparison of the magnitude and direction of the curvature coefficients C of the tracks in an event.

Chapter 5

Data Reduction

In 1986 TASSO obtained 110 pb^{-1} of data, amounting to 40 million triggers written to 1650 PASS 1 tapes, with tracks fitted linearly in the $s-z$ view. As explained in section 2.3.3, for a two-prong event to get written to a PASS 2 tape in the data reduction chain it had to have at least one track fully reconstucted in $r-\phi$ and $s-z$ with $|z_0| < 8$ cm. From Monte Carlo studies it was clear that for a large fraction of mass - magnetic charge combinations, most events of interest to us would not pass this minimum requirement and so we needed to begin our search at the PASS 1 stage. The reason for their failing this minimum requirement was that in many cases the curvature in $s-z$ was too great for a linear track finder to find a parabolic track. Even if a track was found it usually resulted in $|z_0|$ being far greater than 8 cm as usually only 3 or 4 of the DCα were included in the found track and obviously the linear track finder could not take into account the bending away from the vertex of the real track.

Many of the events on PASS 1 could be regarded as being of no interest to us by considering their multiplicities alone. Furthermore in the two-prong events there was not much point refitting well reconstructed muons and Bhabhas where the linear fit in $s-z$ had performed well, as refitting was time consuming and these events when refitted were likely to have low curvatures, that would class then as linear tracks anyway. So cuts were made to reduce the data to be fitted with the adapted track finder. After refitting, further cuts were made on our data sample to remove events poorly described by the parabolic fit in $s-z$ since these were unlikely to be distinctive monopole or dyon candidates.

5.1 Cuts on Events Fitted Linearly in $s - z$

The following cuts were made on the data before refitting was performed. Events were only accepted for refitting if:

1. There were exactly 2 tracks with apparent momentum > 4.0 GeV/c and no other tracks greater than 0.3 GeV/c.
2. The two high momentum tracks were back-to-back in $r - \phi$ to within 10°.
3. The nearest point in $r - \phi$ of each track to the interaction, d_0 was less than 1.0 cm.
4. The $r - \phi$ fit was good ($\chi^2_{r-\phi}$/n.d.f. < 3.0).
5. The difference in TOF between the two high momentum tracks was less than 5 ns and both the TOF values were between -3 and 25 ns.
6. Both high momentum tracks either had ≤ 4 DCα hits in $s-z$ or χ^2_{s-z}/n.d.f. > 1.0.

The first four cuts ensured that two-prong events were found with good track reconstruction in the $r-\phi$ plane, with the first cut removing nearly all of the $\gamma\gamma$ background. The first cut also extracted events containing any particles with high electric charge which might have imitated magnetically charged particles by having inhomogeneities in the magnetic field cause them to curve in the $s-z$ plane. With an apparent momentum cut of 4 GeV/c, and using equation 4.6 the radius of curvature of an electric particle in $s - z$ would have to be greater than 2.6×10^3 cm, the curvature produced by the maximum value of the field of the TASSO solenoid. The angle of 10° in the second cut allowed for multiple scattering and most initial and final state bremsstrahlung. The fifth cut removed the great majority of cosmic ray events close to the event vertex that had not been removed by the third cut, as well as events out of time with the beam crossings. The sixth cut removed most of the two-prong events where the C values from a parabolic fit were likely to be too low to classify them as anything other than linear tracks. This was done by only accepting events where the linear fit in $s - z$ had not described the tracks very well, by either missing some of the hits in the track, or having a relatively poor χ^2 value.

These cuts reduced the initial 40 million triggers to 18,199 PASS 1 events which were then reconstructed from scratch using the adapted FELIX.

5.2 Cuts on Events After Refitting in $s-z$

After having their tracks refitted, further cuts were made to ensure that we were only left with two-prong back-to-back events that had been well reconstructed in $s-z$. Events were therefore only accepted as possible monopole candidates if:

1. Both high momentum tracks had at least five DCα hits (or four if the track passed through the dead region in the fourth DCα layer).

2. The two high momentum tracks were back-to-back at the vertex in $s-z$ to within 20°.

The second cut also reduced further any remaining $\gamma\gamma$ background. This left us with 14,135 events which required the study of their curvatures in $s-z$.

Chapter 6

Analysis and Results

We now needed to see whether there were any candidates from the remaining 14,135 events that we could unambiguously call monopoles or dyon events. To do this we required an analysis of the curvature coefficients from the parabolic fits to these events. In the case of no events being found we needed to know the efficiency with which we could have detected monopoles as functions of their mass and magnetic charge. These are the two major variables affecting the curvatures of the particles; the mass determining their initial velocity and acceleration by the magnetic field (see equation 4.14) and the magnetic charge determining the magnitude of the coupling to the magnetic field. From the efficiencies of detection we may calculate the cross-section limits of production for the process $e^+e^- \rightarrow \gamma^* \rightarrow M\overline{M}$ as functions of mass and magnetic charge.

6.1 Analysis of the Curvature Coefficients

From the curvature coefficients C_i of the two high momentum tracks, we define the quantities C_1, C_2, ΣC and ΔC where

$$|C_1| < |C_2| \tag{6.1}$$

$$\Sigma C = C_1 + C_2 \tag{6.2}$$

$$\Delta C = |C_2| - |C_1| \tag{6.3}$$

It is informative to look at the distribution of C_i against ΣC, comparing what is obtained for the 1986 data which have passed all the cuts of chapter 5, with Monte Carlo data sets of monopoles with mass – magnetic charge combinations of mass = 1 GeV/c^2, g = 40e and mass = 7 GeV/c^2, g = 68.5e. This is shown in figure 6.1. Each high momentum track in an event contributes a point in this plot. For the monopole data sets chosen we see that distinct clusters have formed away the from $C_i = 0$ axis, but close to the $\Sigma C = 0$ axis. Although this is a clear signal for these monopoles this will not be the case for all mass – magnetic charge combinations. For example smaller curvatures of monopoles will cause them to overlap with the region occupied by the 1986 data.

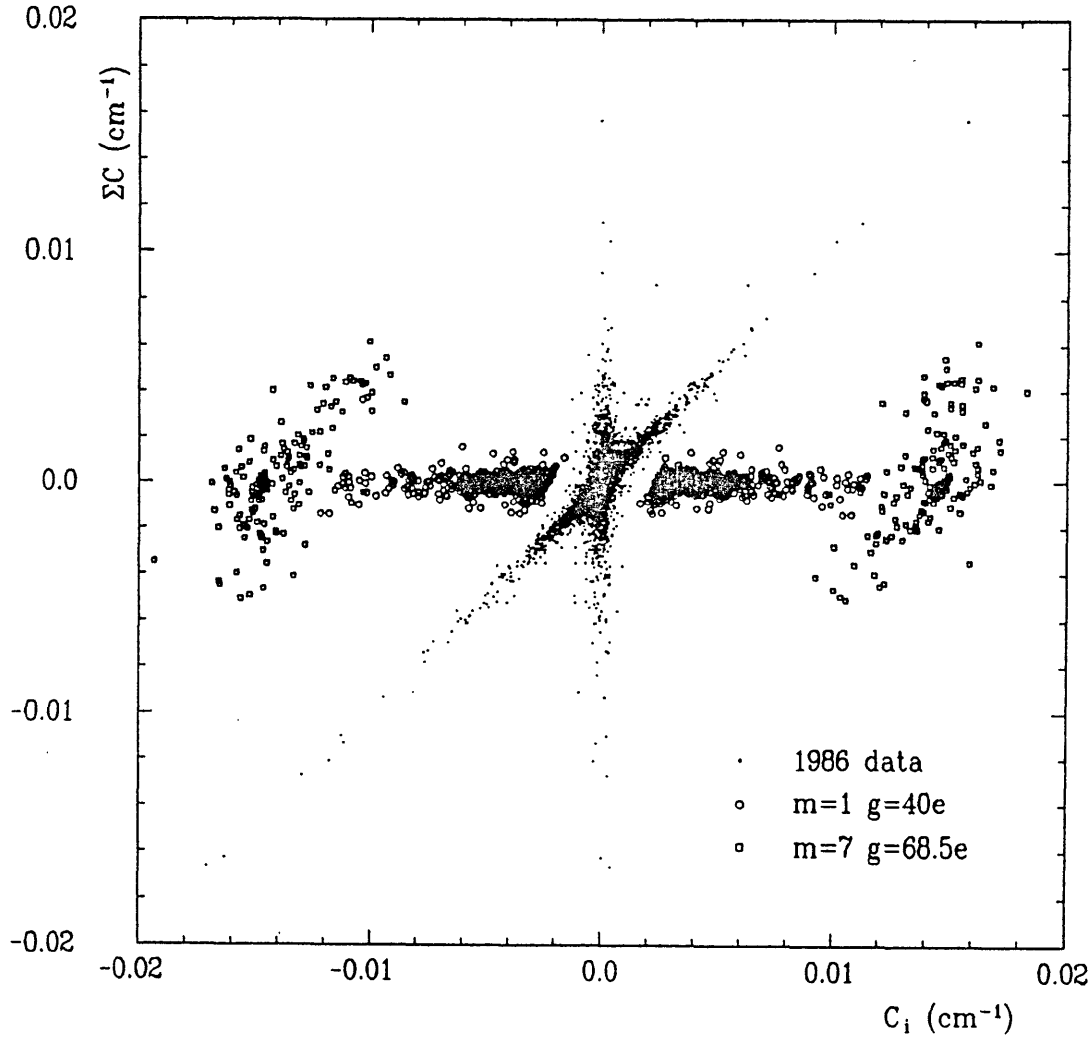


Figure 6.1: *Distribution of C_i against ΣC for the 1986 data and two Monte Carlo monopole data sets.*

To determine the cut to be made on curvatures to separate magnetic charge events from non-magnetic charge events for the 1986 configuration of TASSO we chose a

combination of variables that would produce two distinct distributions: One in which monopole events could lay and the other in which no well-reconstructed monopole events will be found. It was mentioned in section 4.2.4 that monopole events are found to have tracks with opposite curvatures, or equivalently, $C_1C_2 < 0$. If, instead of plotting C_i against ΣC, we plot $|C_i|$ against ΔC then we find that we can separate these into plots for $C_1C_2 < 0$ where identifiable monopoles may appear and $C_1C_2 > 0$, events where the tracks possess the same direction of curvature and so should be free of identifiable monopoles. The plots are shown in figures 6.2 and 6.3. As in figure 6.1, each high momentum track in an event contributes a point to a plot. For these distributions we would expect monopoles to have high values of $|C_i|$ and low values of ΔC for $C_1C_2 < 0$ as they will be required to have curvatures of similar magnitudes, which also need to be large to distinguish them from the non-magnetic background. At first glance it would appear that we determine whether there are any monopoles by comparing figures 6.2 and 6.3. Unfortunately we found that there was an asymmetry between the number of events with $C_1C_2 < 0$ and $C_1C_2 > 0$, there being 6043 of the former and 8092 of the latter. The reason for this is unknown. Fortunately the shapes of the distributions are similar so that we may still use the $C_1C_2 > 0$ distribution to guide us.

A distinct feature of these plots is the arm along $|C_i| = \Delta C$ where one track was found to have a large curvature whilst the other was found to be straight. By projecting these plots onto the axis perpendicular to this arm and plotting just C_1 we obtained the distributions of $|C_1| - \Delta C$ shown in figure 6.4. For $C_1C_2 < 0$ we see no evidence in the distribution that suggests the presence of $M\overline{M}$ events. This distribution has a very similar shape to that of the distribution of events with $C_1C_2 > 0$.

6.1.1 Defining the Magnetic and Non-Magnetic Regions

As no $M\overline{M}$ events have been found we use the distribution of figure 6.4 to define the cut that separates the region of non-magnetic events from that of magnetic events for the 1986 data, and the configuration of TASSO during this period. The cut made was

$$|C_1| - \Delta C > 0.0011 \quad for \quad C_1C_2 < 0 \tag{6.4}$$

defining the region that would be unambiguously populated by $M\overline{M}$ events. In figure 6.5 is shown the $C_1C_2 < 0$ distribution for the 1986 data once again, but this time with the

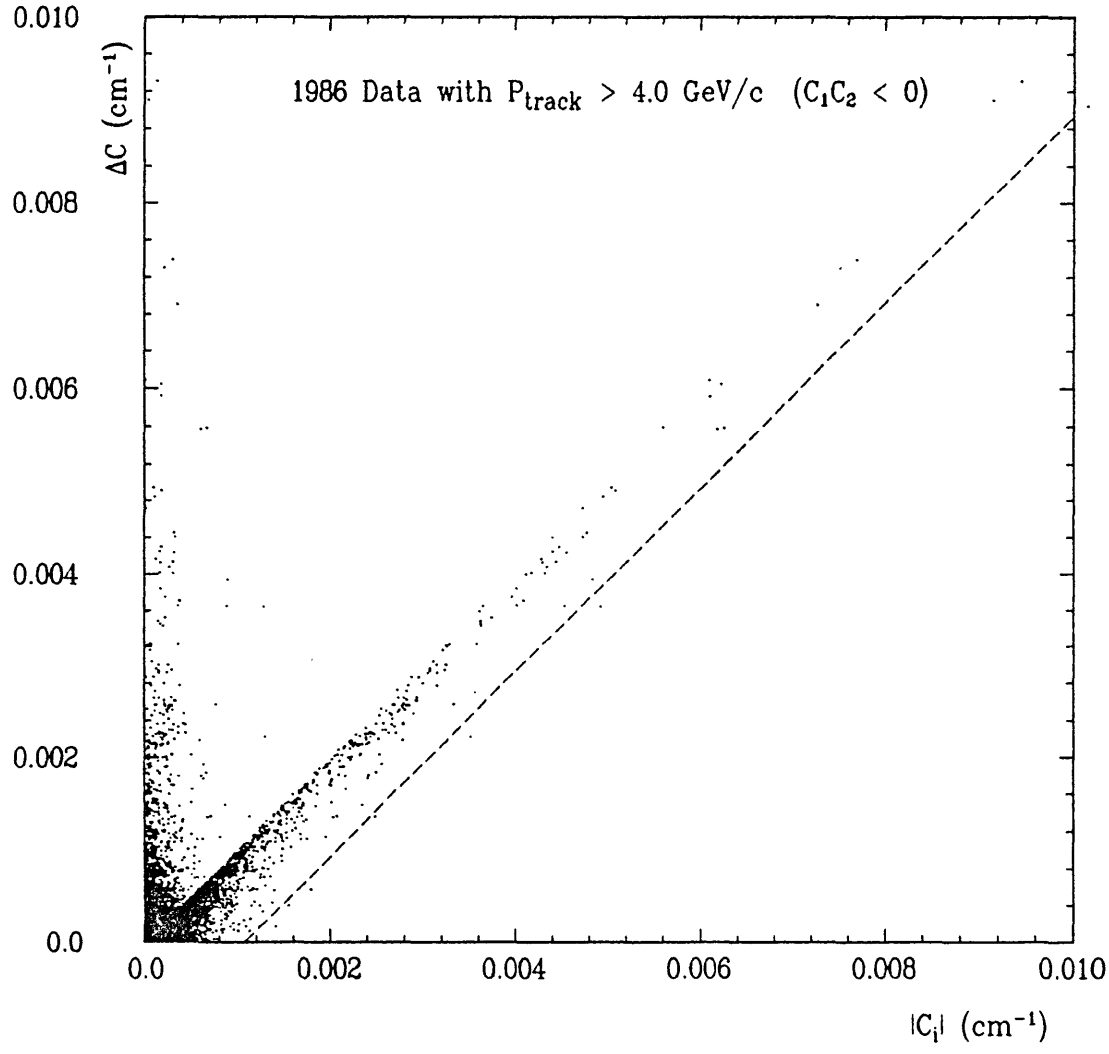


Figure 6.2: *Distribution in $|C_i|$ against ΔC where $C_1C_2 < 0$ for the 1986 data after data reduction.*

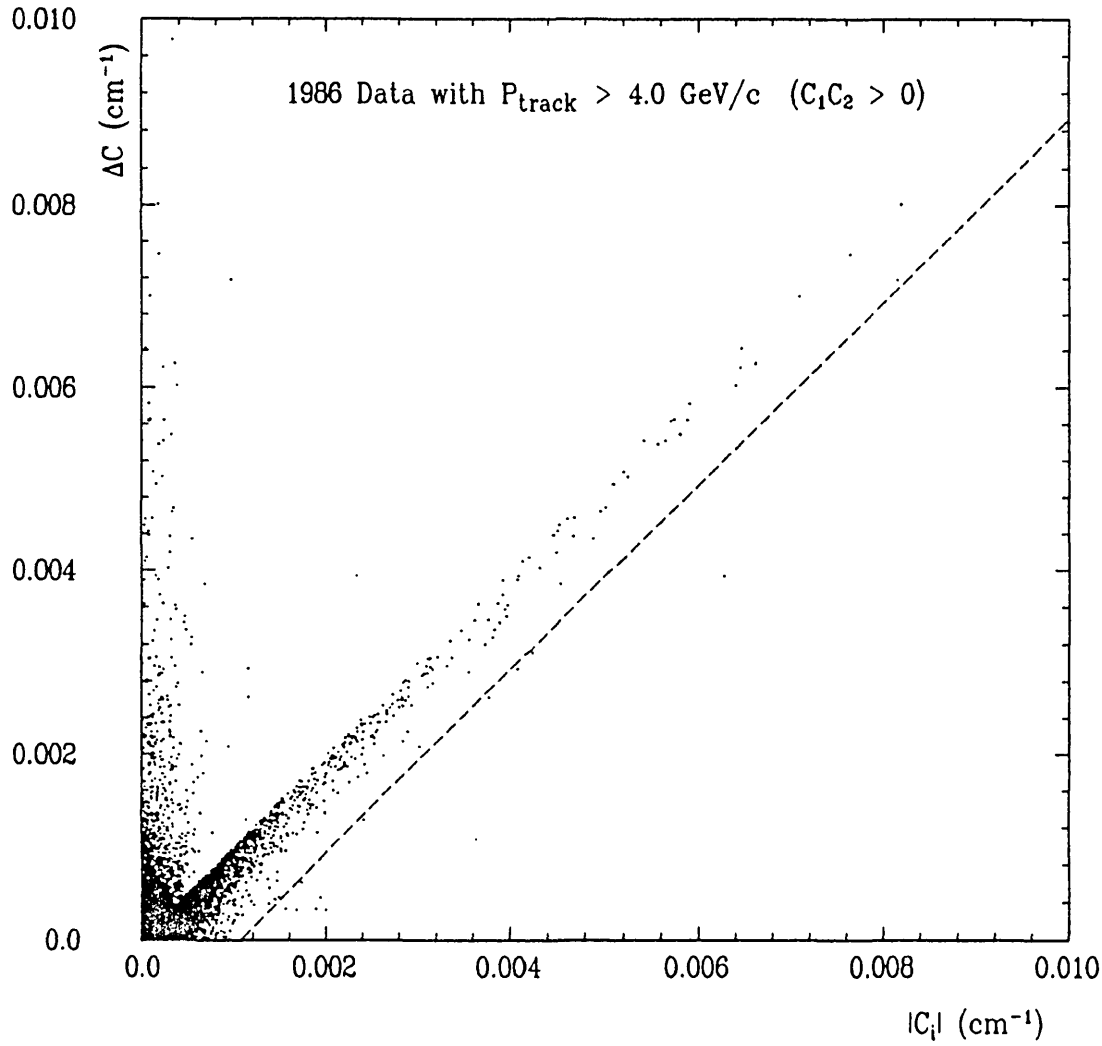


Figure 6.3: *Distribution in* $|C_i|$ *against* ΔC *where* $C_1C_2 > 0$ *for the 1986 data after data reduction.*

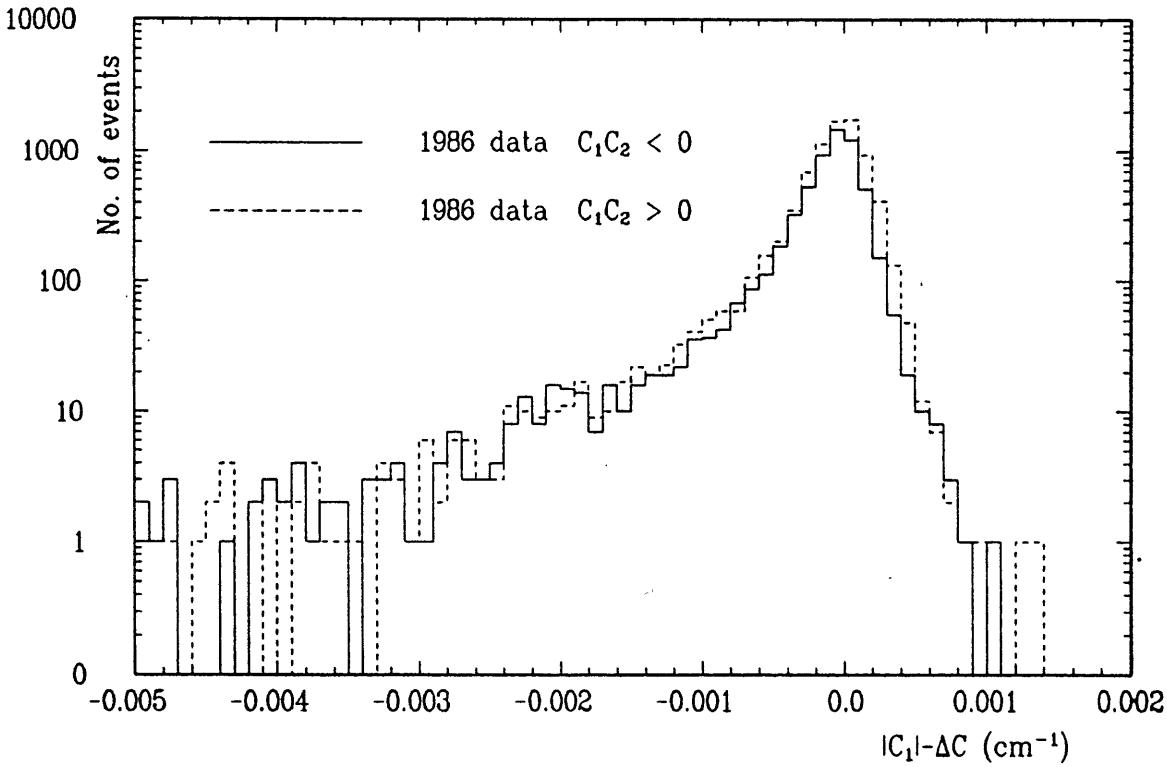


Figure 6.4: *Distributions of* $|C_1| - \Delta C$ *for the 1986 data after data reduction.*

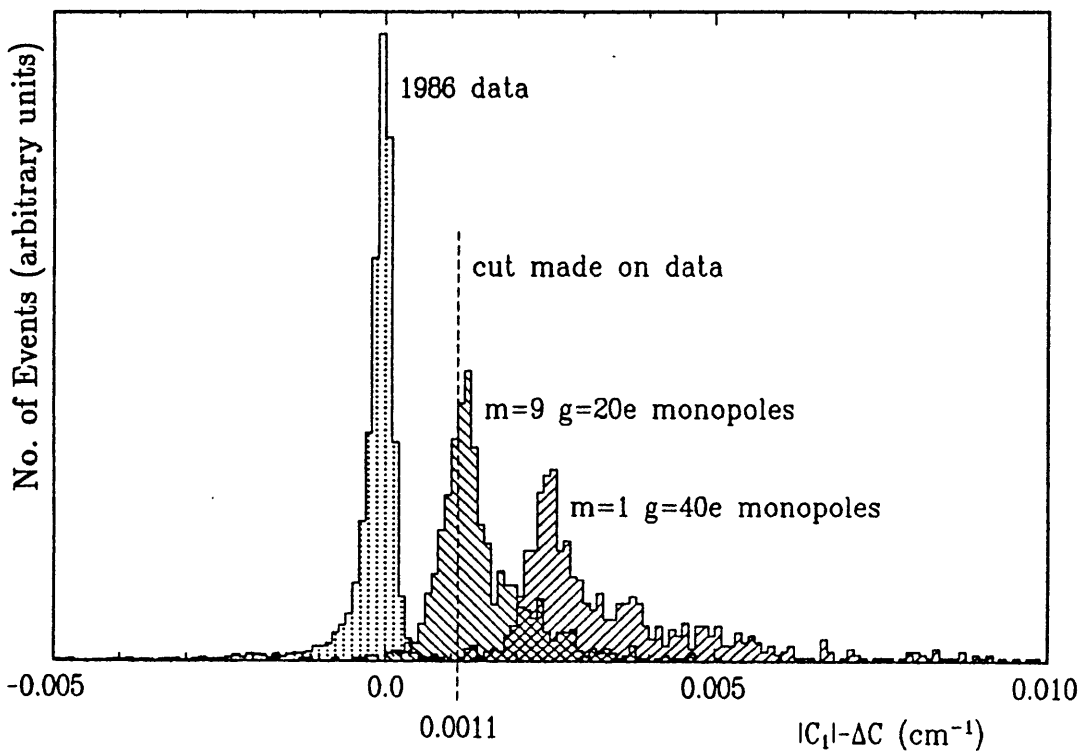


Figure 6.5: *Distributions of* $|C_1| - \Delta C$ *with* $C_1C_2 < 0$ *for the 1986 data and two simulated monopole data sets after data reduction.*

simulated monopole data sets shown in the C distribution of figure 4.4, after the cuts of chapter 5 have been applied. The applied cut of the inequality 6.4 is also shown and we see that for one of the monopole data sets a large fraction of events are lost as their curvatures are too low to distinguish them from the non-magnetic 1986 data. For the other data set though we see that the distinction between them and the 1986 data is a good one indicating that this analysis performs very well in detecting monopoles of certain mass and magnetic charge combinations.

6.2 Calculating the Monopole Detection Efficiencies

As no events with magnetic charge were discovered we had to find which combinations of mass and magnetic charge the experiment and analysis were sensitive to and the efficiencies with which we could detect these monopoles. To do this we went through the following procedure for each combination of mass and magnetic charge chosen:

1. Generate isotropically distributed data sets of monopoles of given mass and magnetic charge.
2. Fit all the events with the FOREST track finder.
3. Apply the MILL track finder to all the events that pass the requirements.
4. Fit all the events with the FELIX track finder using the parabolic track finder in $s-z$ and a z vertex constraint of 1.85 cm.
5. Apply the cuts of chapter 5 and a geometric trigger cut.
6. Apply the cut of the inequality 6.4.

The efficiency of detection is then defined as

$$\frac{number\ of\ events\ surviving\ after\ final\ cut}{number\ of\ events\ generated}$$

The maximum possible efficiency is constrained by the solid angle covered by the triggering components of the two-prong trigger outlined in section 2.3.1 and so is 82%.

6.2.1 Effect of χ^2 Cuts on Efficiencies

The maximum efficiency we obtained was lower due to problems with the χ^2 cuts made in both $r-\phi$ and $s-z$. It was found that the distributions in χ^2 were very different between the Bhabhas from the 1986 data and Monte Carlo Bhabhas, and very much more so for tracks fitted with FOREST than for those fitted with MILL. These differences can be seen in figures 6.6 and 6.7. This problem was only discovered after all the 1986 data had been reduced. As our simulated monopoles were fitted with either track finder

depending upon whether the event passed the MILLing criteria, it was decided the best way to determine how the cuts affected our efficiencies was to use χ^2 cuts corresponding to the ones used on the data, calculated on a "fraction of events lost" basis. This was done by fitting the 1986 Bhabhas with both FOREST and MILL tracks and then studying the χ^2 distributions to see what fraction of events were lost by each of the cuts, $\chi^2_{r-\phi}/\text{n.d.f.} > 3.0$ and $\chi^2_{s-z}/\text{n.d.f.} < 1.0$. The cuts chosen to be used on the Monte Carlo data were then those that resulted in the same fraction of events being lost. The cuts obtained by this method are given in table 6.1 with the distributions that determined these cuts shown in figures 6.6 and 6.7. The cuts applied to the data had been chosen after studies of two-prong events fitted with MILL.

Track Finder	View	χ^2 Cut on Data	Fraction of Events Lost	χ^2 Cut on MC
FOREST	$r-\phi$	3.0	0.1240	0.65
	$s-z$	1.0	0.4996	0.45
MILL	$r-\phi$	3.0	0.0009	2.10
	$s-z$	1.0	0.3107	0.65

Table 6.1: *χ^2/n.d.f. cuts applied to data and Monte Carlo*

6.2.2 Monopole Detection Efficiencies for 1986

Once efficiencies had been obtained for sufficient mass and magnetic charge combinations, it was possible to plot a contour map of the efficiencies in the mass – magnetic charge plane. The resulting plot is shown in figure 6.8. The peak efficiency obtained was just over 60%. It was found that the problem of the χ^2 cut affected us mostly for monopoles of high charge or mass as these curved sufficiently to fail the criterion to apply MILL. This in a sense evened out the efficiencies as the events that had MILL applied to them and therefore were not so badly affected by the χ^2 cut were also the events with straighter $s-z$ tracks. These were consequently lost by the final curvature cut of the inequality 6.4. The loss of low mass monopoles was due to their high momenta leading to low curvatures. For the low charge monopoles the coupling to the field was too weak to cause a significant curvature. In both cases the straightness of the tracks caused them to merge into the non-magnetic background. On the other end of the scale the highly charged and heavy monopoles were lost because they were either pulled out of the central chamber before the event could be triggered, or the ionization loss was too great for them to escape from the 6 mm of aluminium surrounding the DC, so that once again the event would not be triggered.

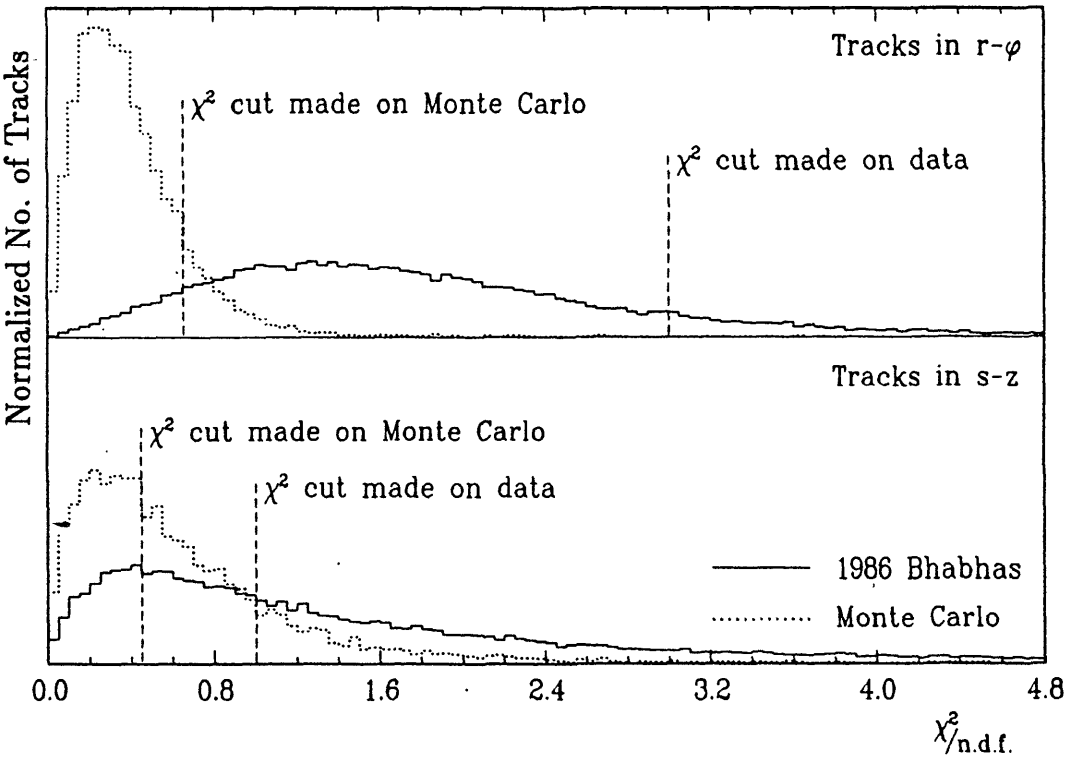


Figure 6.6: *Distributions in χ^2/n.d.f. for FOREST.*

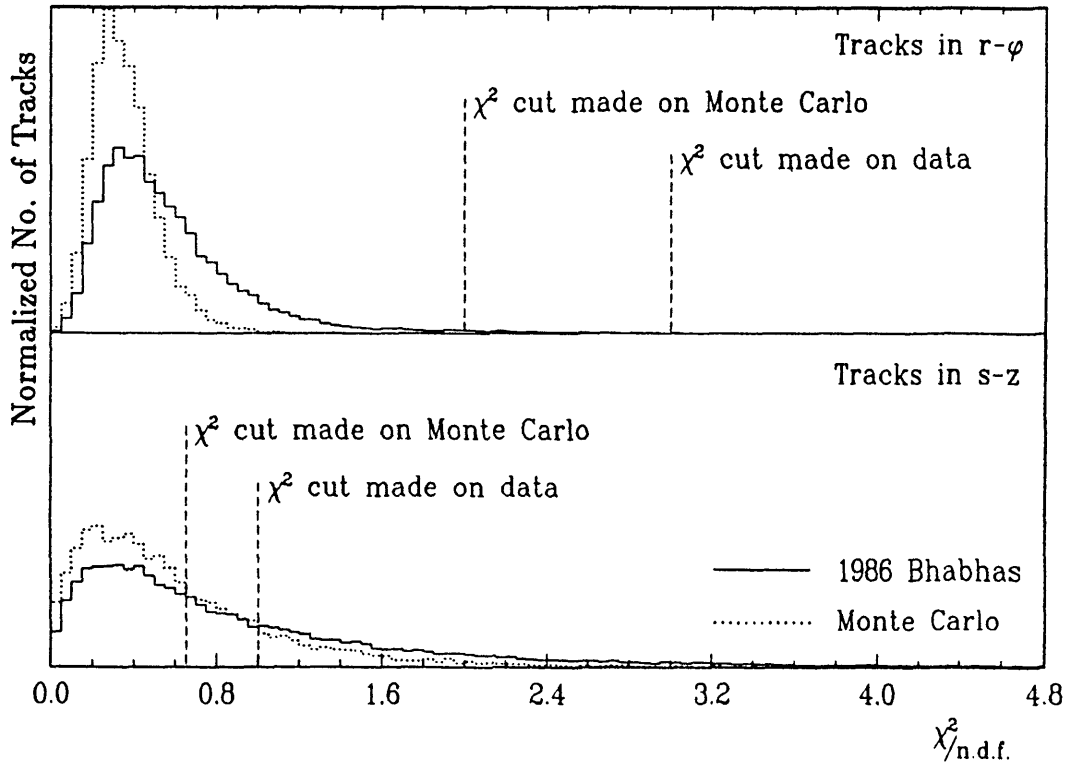


Figure 6.7: *Distributions in χ^2/n.d.f. for MILL.*

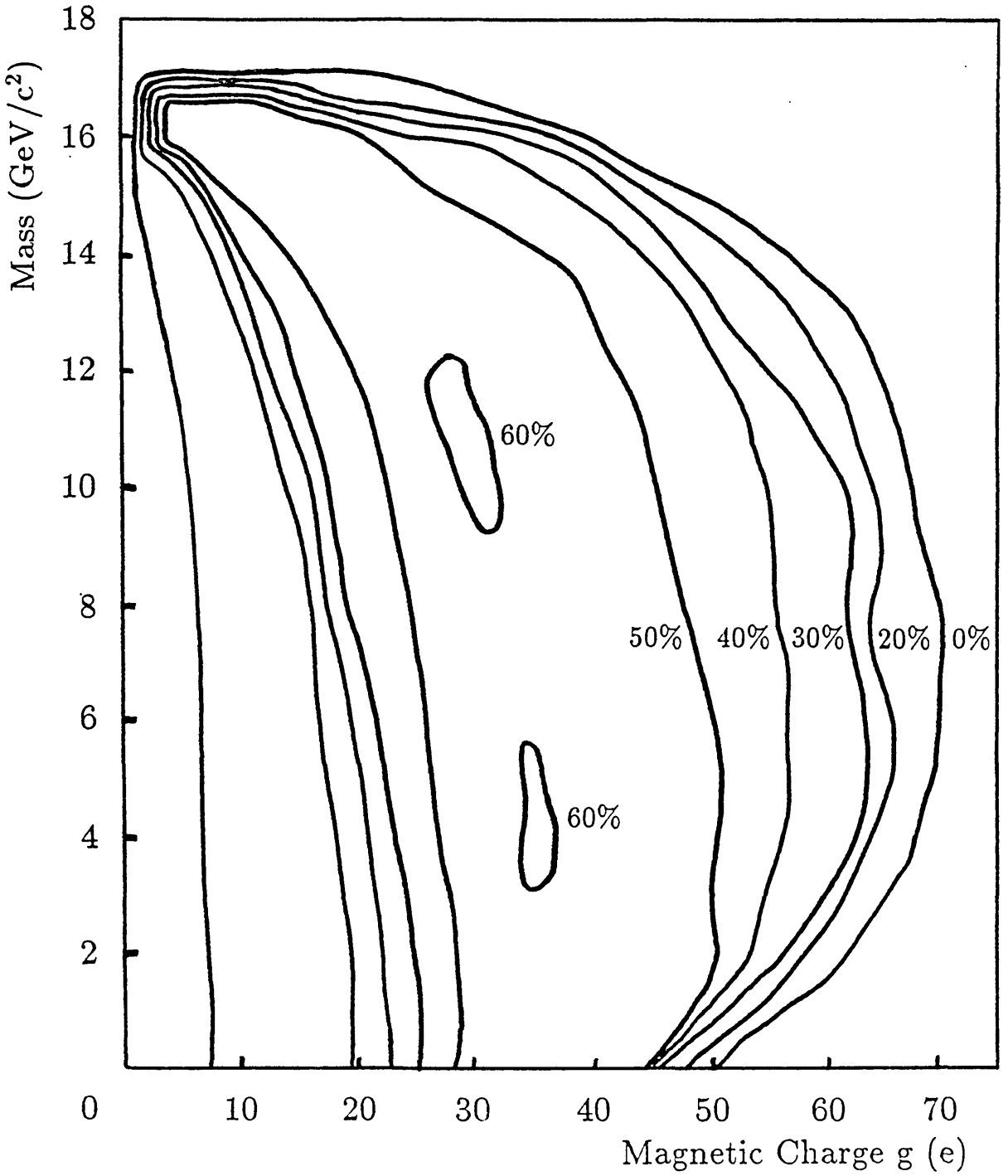


Figure 6.8: *Efficiency plot for monopole detection in TASSO as configured in 1986.*

6.3 Effects upon Detection Efficiencies

Studies were made on the effect various experimental and physical parameters had upon our detection efficiencies. Using representative monopole data sets from various points in the mass – magnetic charge plane, effects on efficiencies due to variations in intrinsic electric charge, incoherent noise, smearing of $\langle dE/dx \rangle$ and the vertex constraint in the $s-z$ fit were examined.

6.3.1 Intrinsic Electric Charge

To study the efficiencies of dyon detection we added electric charge to the particles when generating them, the sign of the electric charge being uncorrelated with that of the magnetic charge. It would be expected that the efficiencies would drop relative to their monopole conterparts, due to increases in energy loss and path length. The results are shown in figure 6.9. As can be seen, efficiencies for dyons of unit electric charge appear to be no lower than those of monopoles, but as the electric charge increases the efficiencies drop off rapidly. This is due almost entirely to the effect of the cut made on apparent momentum, as the apparent momentum decreases as the electric charge increases. Being indistinguishable from monopoles, due to the accuracy of the momentum measurements from the curvature in $r-\phi$, dyons with the fractional electric charges of quarks would have efficiencies that were the same as monopoles or unit charged dyons.

6.3.2 Incoherent Noise

The effect of incoherent noise was studied by adding random noise hits to the DC. The results are shown in figure 6.10. This mainly affects the reconstruction and as may be expected, in a high noise environment the efficiencies drop as noise hits are misidentified in the track reconstruction. For the 1986 data-taking period there were on average of about 10 hits in the DC not attributed to tracks in Bhabha events with an average of one of these occurring in an $s-z$ projection of one of the tracks. The effect of coherent noise in the form of δ-rays is examined in section 6.4.

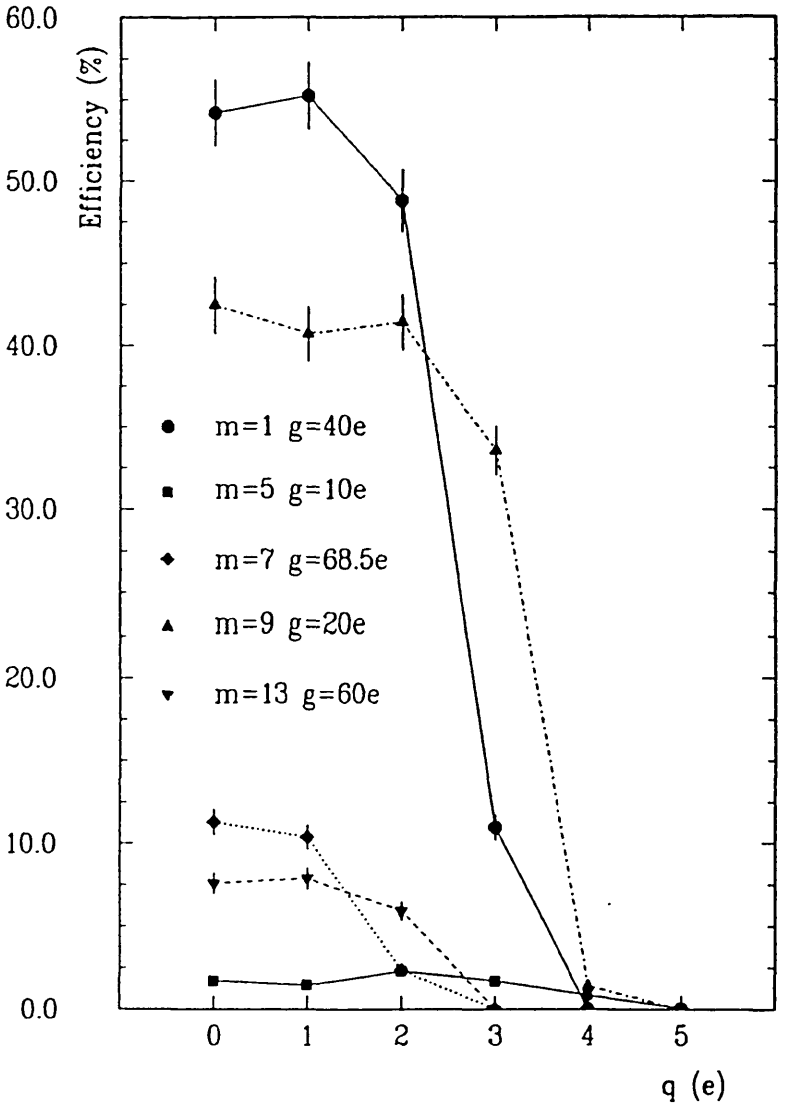


Figure 6.9: *Effect of intrinsic electric charge on detection efficiencies.*

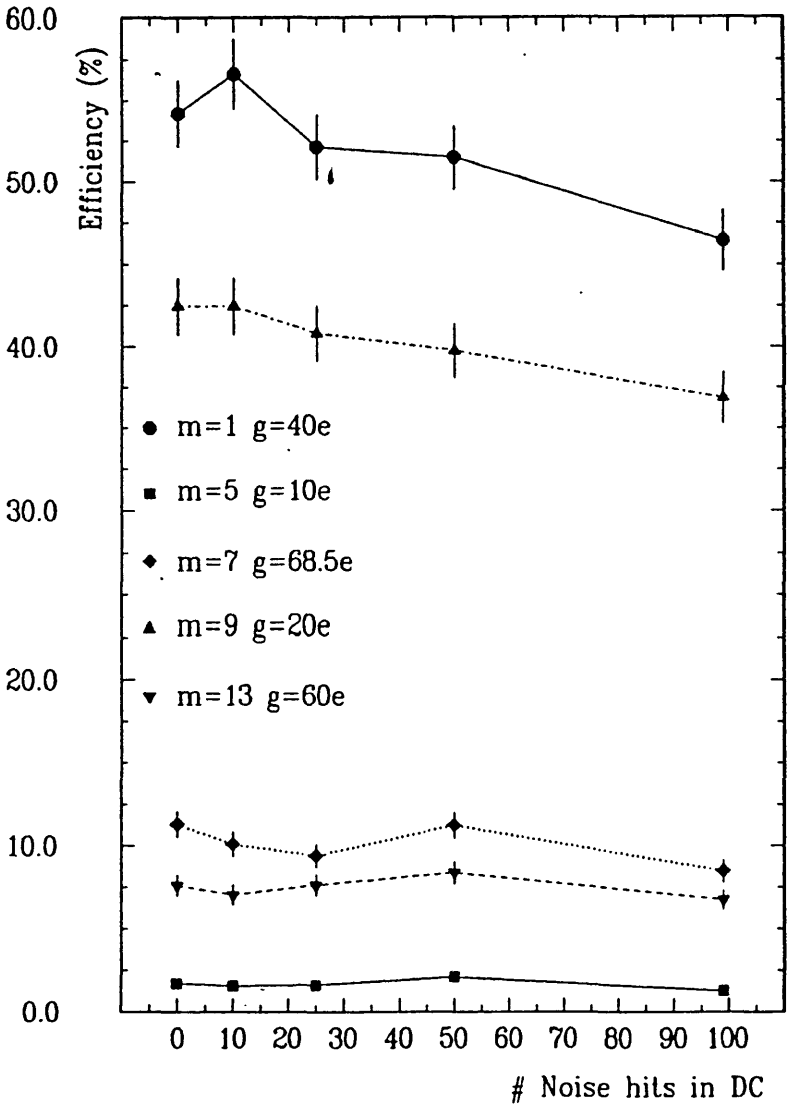


Figure 6.10: *Effect of incoherent noise in the DC on detection efficiencies.*

6.3.3 Smearing of ⟨dE/dx⟩

Although there are theoretical predictions for the average energy lost by a magnetically charged particle, there are no such predictions for the shape or width of the distribution. It is not even certain that monopoles would produce the Landau distribution that is characteristic of magnetically neutral particles, as the tail of such a distribution is due to high energy δ-rays (described in more detail in section 6.4) produced by magnetically neutral particles via 'head-on' collisions with the electrons in the matter traversed. For monopoles the forces are transverse rather than longitudinal [17] giving a cross-section for head on collisions that tends to zero and so it is not unreasonable to assume that high energy δ-rays might not even be produced, thereby resulting in a Gaussian distribution for the energy loss. Consequently, in the Monte Carlo we smeared the average dE/dx losses, calculated for each step, by Gaussians of widths which were appreciable fractions of the average dE/dx loss.

Figure 6.11 shows the result of smearing the average value of dE/dx by up to 25% in each detector medium. We see that this had no measurable impact on our efficiencies and so we can conclude that for widths up to 25% the distribution of energy loss is unimportant in this analysis.

6.3.4 Vertex Constraint in $s - z$ Fit

To assess the effect of the vertex constraint upon our detection efficiencies we refitted our representative monopole data sets with various vertex constraints and calculated their efficiencies with the assumption that the cut of the inequality 6.4 had not altered. Refitting all the data for each constraint and calculating a new curvature cut each time would have been impractical. Although the method is not exact we see from figure 6.12 that the efficiencies calculated this way do not vary too much and overall we appeared to pick a constraint that retained good efficiencies over most of the mass – magnetic charge plane in comparison to the other constraints.

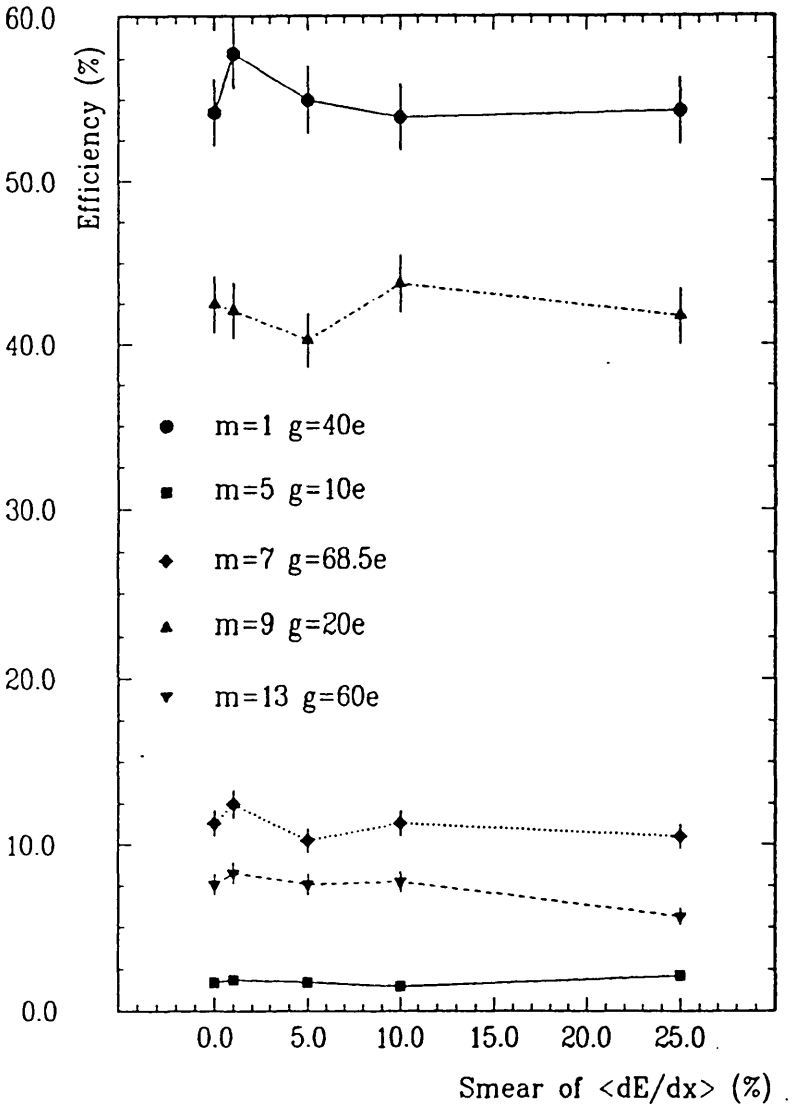


Figure 6.11: *Effect of smearing of $\langle dE/dx \rangle$ on detection efficiencies.*

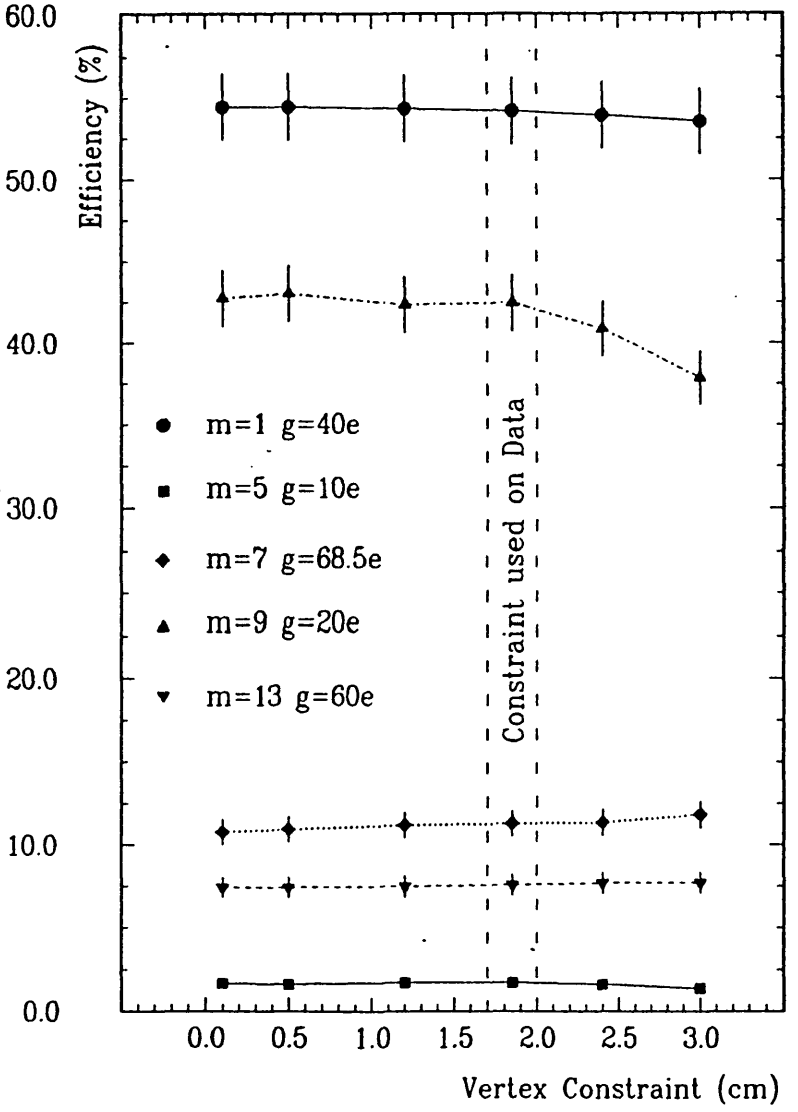


Figure 6.12: *Effect of vertex constraint in $s-z$ fit on detection efficiencies.*

6.4 The Effects of High Energy δ-rays

As already mentioned in section 6.3.3 it is not entirely clear that monopoles would even produce high energy δ-rays. Even so, a study was made of the effect they would have on our detection efficiencies if they were produced.

6.4.1 What are δ-rays?

The ionization loss of a particle traversing a medium is due to Coulomb interactions between that particle and the electrons in the medium. In these collisions the energy transfer can be anything up to the maximum allowed value E_M constrained by two-body relativistic kinematics:

$$E_M = \frac{2mc^2\beta^2}{1-\beta^2} \tag{6.5}$$

This is for a head-on collision for which the question of whether monopoles produce high energy δ-rays arises in the first place. The probability of an electron receiving energy E is given by [45]

$$P(E)\,dE \quad = \quad \frac{DZ\rho}{A}\left(\frac{q}{e\beta}\right)^2 \frac{x}{E^2}dE \quad = \quad \frac{W}{E^2}dE \tag{6.6}$$

which corresponds essentially to the first term of the Bethe-Bloch equation (equation 3.5). Here, x is in g/cm^2. 'δ-ray' is the term given to an electron receiving enough energy to be ejected with an energy above a few keV, but essentially we can treat all ionization loss as manifesting itself in δ-rays across the whole energy spectrum up to E_M.

Integrating equation 6.6 gives an expression for the number of δ-rays per unit length having energy $E \geq E_0$:

$$N(E \geq E_0) \quad = \quad \int_{E_0}^{E_M} P(E)\,dE \quad = \quad W\left(\frac{1}{E_0} - \frac{1}{E_M}\right) \tag{6.7}$$

If monopoles are to lose $g^2\beta^2/e^2$ times more energy per unit length than magnetically neutral particles as assumed in section 3.3.1 and the maximum energy loss is constrained by kinematics then we would expect that there are $g^2\beta^2/e^2$ times more interactions per

unit length to account for this energy loss. Assuming that the energy spectrum is the same, the number of δ-rays liberated per unit length for monopoles will be

$$N(E \geq E_0) = \frac{g^2\beta^2}{e^2} W \left(\frac{1}{E_0} - \frac{1}{E_M}\right) \tag{6.8}$$

The angle of emission of a δ-ray of energy E is given in a free-electron approximation by [45]

$$\cos^2\theta = \frac{E}{E_M} \tag{6.9}$$

6.4.2 Why Could δ-rays be a Problem?

If a δ-ray is emitted in the DC with sufficient energy, then it will produce its own ionization path. If this path crosses a drift cell, it will cause a hit to be registered by the chamber. This is coherent noise related to the monopole. As the chamber electronics was only designed for single hits, track hits will be misplaced if the δ-ray ionization reaches the same wire before that from the monopole. This will adversely affect the track recognition by worsening the χ^2 of the fit and altering the curvature of the $s-z$ fit. If enough noise hits are generated they may prevent the track from being recognised at all.

At first glance the situation appears serious as $g^2\beta^2/e^2$ times more δ-rays will be produced. However, there are a number of factors that lessen the effect and work in our favour:

- From equation 6.9 we can see that the most energetic δ-rays will be emitted parallel to the monopole's path, thereby minimizing the possible displacement of the hit that they might cause.
- δ-rays will be randomly emitted in the plane perpendicular to the monopole's path so that many of them will be ejected on the far side of the monopole to the sense wire so that the monopole's ionization will register first.
- The magnetic field in the chamber will cause the less energetic δ-rays to curl up with a radius of curvature

$$R(\mathrm{m}) = 3.33 p_\perp(\mathrm{GeV/c})/B(\mathrm{Tesla}) \tag{6.10}$$

where $p_\perp$ is the momentum of the δ-ray in the $r-\phi$ plane. Using the relationship

$$p^2c^2 = T\left(T + 2mc^2\right) \tag{6.11}$$

where T is the kinetic energy of the δ-ray, we find that for an energy of 150 keV the radius of curvature with which the δ-rays curls up is 280 μm, the spatial resolution of the chamber, so that we consider only δ-rays with an energy larger than this will adversely affect the track recognition.

6.4.3 Simulating the Effect of δ-rays

This was done outside the framework of the other Monte Carlo studies performed in this analysis. For single monopole tracks of a given mass and magnetic charge the number of δ-rays that would be emitted was calculated along with their angles of emission using equations 6.8 and 6.9. From these we looked at the probability of the emitted δ-rays adversely effecting our track finding by their ionization reaching the sense wires before that of the monopole, taking into account all the factors outlined in section 6.4.2.

6.4.4 Consequence of High Energy δ-ray Emission

If δ-rays were to be emitted with the same energy spectrum as from magnetically neutral particles but with a $g^2\beta^2/e^2$ rate factor then we found that there was a negligible effect on detection efficiencies for 'heavy' monopoles of 15 GeV/c^2, where β is low. In the worse case, for $g = 70e$ (the limit of our detection) and masses of 5 – 10 GeV/c^2, our efficiencies were approximately halved. At lower values of g the effects were smaller. At $g = 40e$ for these masses it appeared to be at most a 10% effect.

As already mentioned it is not certain that the same energy spectrum as for magnetically neutral particles would apply, as the transverse direction of the forces may very well lower the probability of high energy δ-rays being emitted. The energy loss would therefore be compensated for by many more low energy δ-rays being produced that would not affect the track finding in any way.

6.5 Cross-Section Limits of Monopole Production

As no candidate events were observed we assume that our distributions are governed by Poisson statistics and therefore assign an upper limit of 2.30 events with a 90% confidence level for each mass – magnetic charge combination. Cross-section upper limits $\sigma\left(e^+e^- \rightarrow M\overline{M}\right)$ for each combination are then calculated as

$$\frac{2.30}{\textit{detection efficiency} \times \textit{trigger efficiency} \times \textit{total luminosity of events analysed}} \tag{6.12}$$

where the total luminosity of the events analysed was 110 pb^{-1} and we assume an overall trigger efficiency of 98%. Using the efficiencies of figure 6.8 we can plot the distributions in the upper limit of R, shown in figure 6.13, where

$$\text{R} = \frac{\sigma\left(e^+e^- \rightarrow M\overline{M}\right)}{\sigma\left(e^+e^- \rightarrow \mu^+\mu^-\right)} \tag{6.13}$$

and

$$\sigma\left(e^+e^- \rightarrow \mu^+\mu^-\right) \quad = \quad \frac{86.9}{s}\ \text{nb} \quad = \quad 0.071\ \text{nb for}\ \sqrt{s} = 35\ \text{GeV}$$

As well as plotting our results in figure 6.13, we also show results of previous experiments for comparison. It can be seen that this analysis has bridged the gap between the CLEO result [15] and the earlier accelerator searches which were insensitive to low values of g. The PEP result [11] was only sensitive to charges greater than $30e$ and relied on a knowledge of the permanent effects of the passage of a monopole through various substances. The similar PETRA result [12] and the ISR result [10] were only sensitive to monopoles of greater than about $50e$.

It should be emphasized that the cross-sections that we find are for the particular model of matter interactions we have chosen to use for our Monte Carlo studies whilst the method of the search itself is generally model independent.

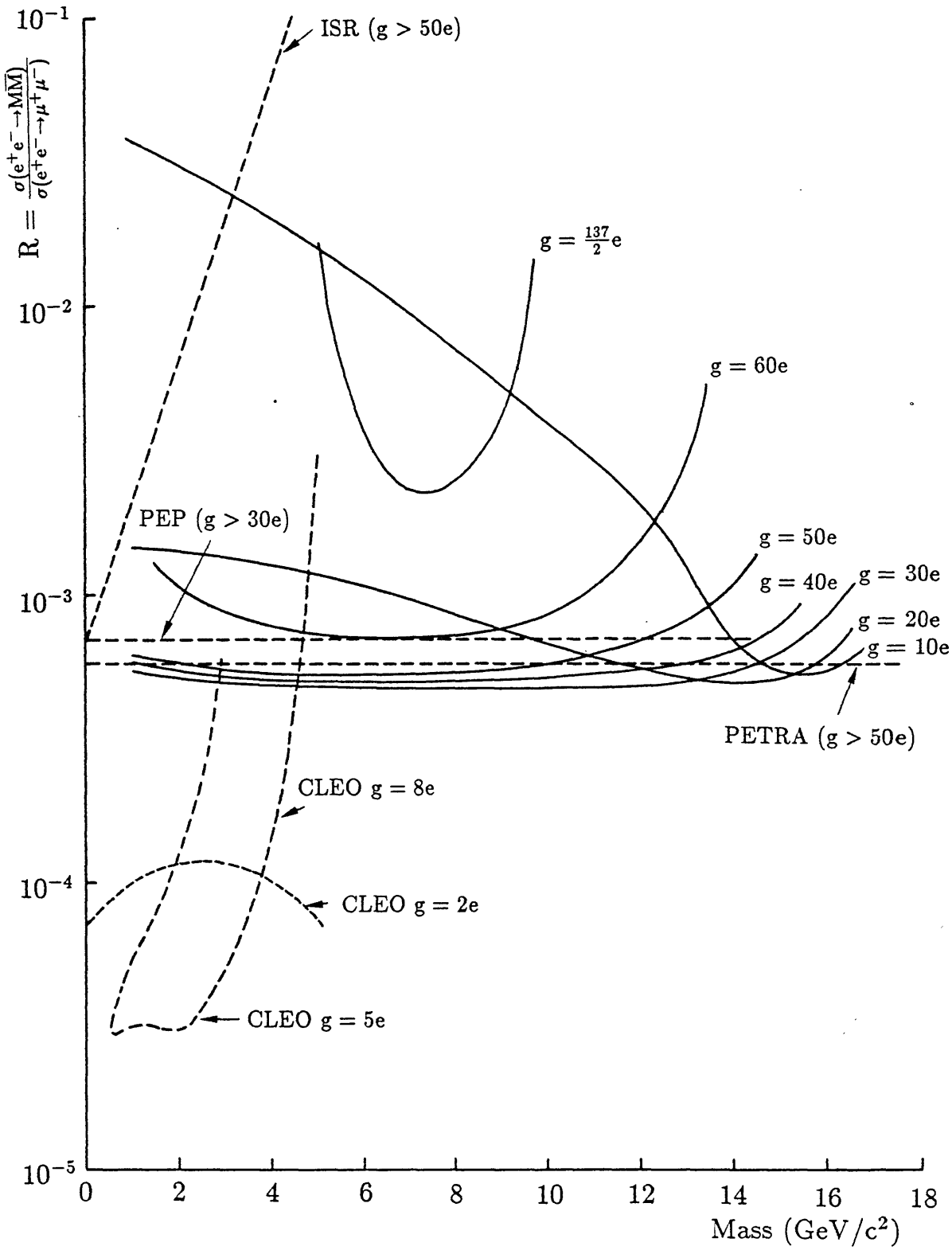


Figure 6.13: *The limits on $M\overline{M}$ production cross section relative to the QED cross-section for the process $e^+e^- \to \mu^+\mu^-$ as a function of monopole mass for various magnetic charges. Results from the ISR [10], PEP [11], PETRA [12] and CLEO [15] experiments are plotted for comparison.*



MONOPOL HOTEL
Reeperbahn 48-52, HH 4
☎ (040) 31 27 60 + 31 35 37
170 beds, BG, elevator, rooms with
tel., all rooms bath, shower, WC
SR. 75,00-89,00 ₰ DR. 108,00-130,00*

Figure 6.14: *Photographic evidence of the only Monopol(e) found in Hamburg*

Part II

Multi-Pulse Performance of a Test Drift Cell for Zeus

Chapter 7

A Test Drift Cell for ZEUS

To investigate the performance to be expected from a cell of the CTD in the ZEUS experiment, a rectangular test drift chamber has been constructed and placed in a 3 GeV electron test beam at DESY. A study of the chamber's multi-pulse performance is described in chapter 8.

7.1 HERA and ZEUS

The Hadron Electron Ring Accelerator, or HERA, situated at DESY, is one of the new generation of particle colliders presently being built around the world. It will be the only $e^{\mp}p$ collider in the world when completed, producing collisions of 30 GeV electrons or positrons with 820 GeV protons at $\sqrt{s} = 314$ GeV and $Q^2_{\rm max} = 10^5$ GeV^2. These energetic collisions between leptons and hadrons will enable investigations to be made into the possible substructures of quarks and leptons to distances $\sim 10^{-18}$ m. Searches will be performed for new mediators of the neutral and charged currents with masses up to 800 GeV/c^2. More exotic physics phenomena such as leptoquarks of masses up to 180 GeV/c^2, excited quarks and leptons of masses up to 250 GeV/c^2 and supersymmetric particles up to masses of 180 GeV/c^2 will also be observable, provided they exist. For further details of the collider and the potential physics to come out of it, see reference [46].

There will be two detectors on the HERA ring, ZEUS [47,48] and H1 [49], with H1

optimized for lepton identification whilst ZEUS will be better suited to charged current interactions.

The British involvement within ZEUS is in the construction, calibration and maintainance of the Central Track Detector (CTD) [47,48]. A segment of the CTD is shown in figure 7.1.

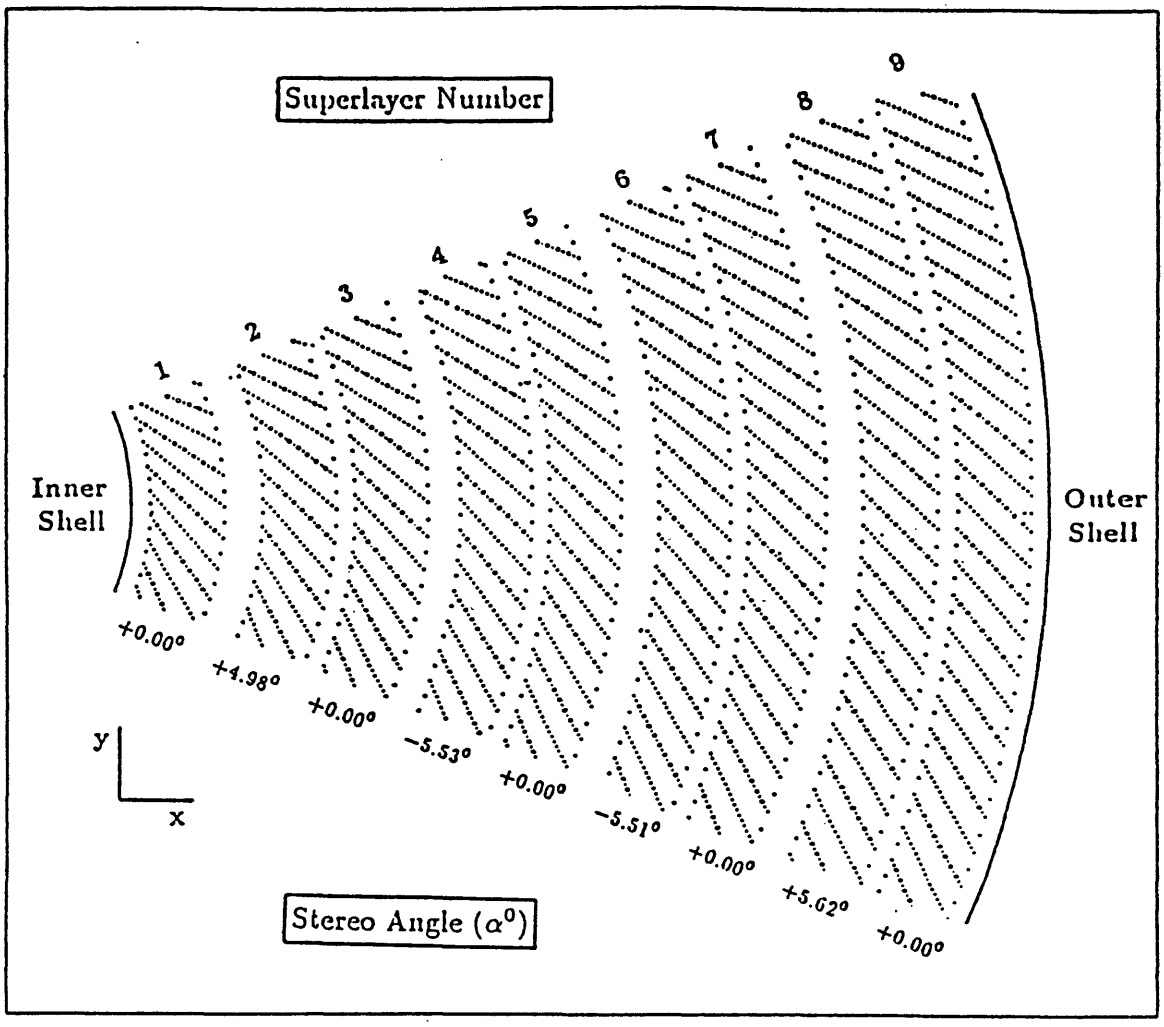


Figure 7.1: *A segment of the ZEUS Central Track Detector.*

The CTD has an outer radius of 85 cm and a length of 240 cm. There are 9 superlayers, each with cells made up of 8 layers of sense wires. The drift cells are tilted so that the combined effect of the 1.8 Tesla magnetic field of the solenoid in ZEUS and the electric drift field within the CTD result in a particle's ionization drifting azimuthally to the sense wires. The maximum drift length is 2.5 cm corresponding to 500 ns drift time in an argon/ethane 50/50 gas mixture at atmospheric pressure. As beam crossings occur every 96 ns in HERA, this maximum drift time corresponds to

five beam crossings. Five of the superlayers have axial wires and four have stereo angles up to 5.6°. There are a total of 4608 sense wires and 19584 field wires.

Up to five events can have occurred before the ionization has drifted to the sense wires and it is expected that events at HERA will have a high density of tracks making up jets. It is therefore important to know how the chamber and its electronics may perform when more than one pulse is picked up by the sense wires. There should be as little effect as possible upon track hits depending on whether it was the first or a subsequent pulse. Owing to the geometry of the CTD, close tracks will exchange their hit order on crossing the line of sense wires within a cell.

A rectangular cell test chamber representing two cells in the CTD, with a 100 MHz FADC (Flash Analogue to Digital Converter) readout has been constructed and from this we have been able to examine the multi-pulse performance of such cells.

7.2 The Rectangular Cell Test Chamber

7.2.1 Chamber Construction

The chamber geometry is shown in figure 7.2. It consists of two drift cells, each containing a plane of 8 sense wires, with the drift in the direction perpendicular to the sense wire plane up to a maximum distance of 20 mm. This distance has been chosen to be typical of the wide end of the CTD tapered cells. Wires are spaced 6 mm apart in the sense wire plane with sense and potential wires alternating. The sense wires are made of 30 μm gold plated tungsten tensioned to 60 gm with a locational accuracy of ± 60 μm r.m.s. The active length of the chamber is 40 cm and it is in a 1 mm thick aluminium alloy gas containment vessel with beam entry and exit windows made out of 0.25 mm mylar.

7.2.2 Chamber Electronics

At the chamber were on-board pre-amplifiers that amplified the sense wire signals by a factor of 12 before transmitting them down 40 m of co-axial cable to the post-amplifiers and FADC system situated in the control room. The post-amplifiers were equipped with a variable gain so as to match the pulse amplitudes to the range of the FADC. Furthermore a pole-zero filter could be included at the input of the post-amplifiers to cancel the $1/t$ tail of the drift chamber signals (see section 7.3). The FADC system consisted of four Struck DL300 [50] modules based on the Siemens SDA5010 100 MHz 6-bit FADC chip, operated in a non-linear fashion [51]. The 16-channel system was controlled and read out by a LSI-11/73 computer via CAMAC, with event data being written to magnetic tape for off-line analysis.

7.2.3 Operating the Chamber

The chamber was operated at atmospheric pressure with a gas mixture of 50% argon and 50% ethane (the same as being considered for the CTD) bubbled through ethanol at 0°C. This mixture gives an electron drift velocity of ~ 50 μm/ns. The 1% admixture

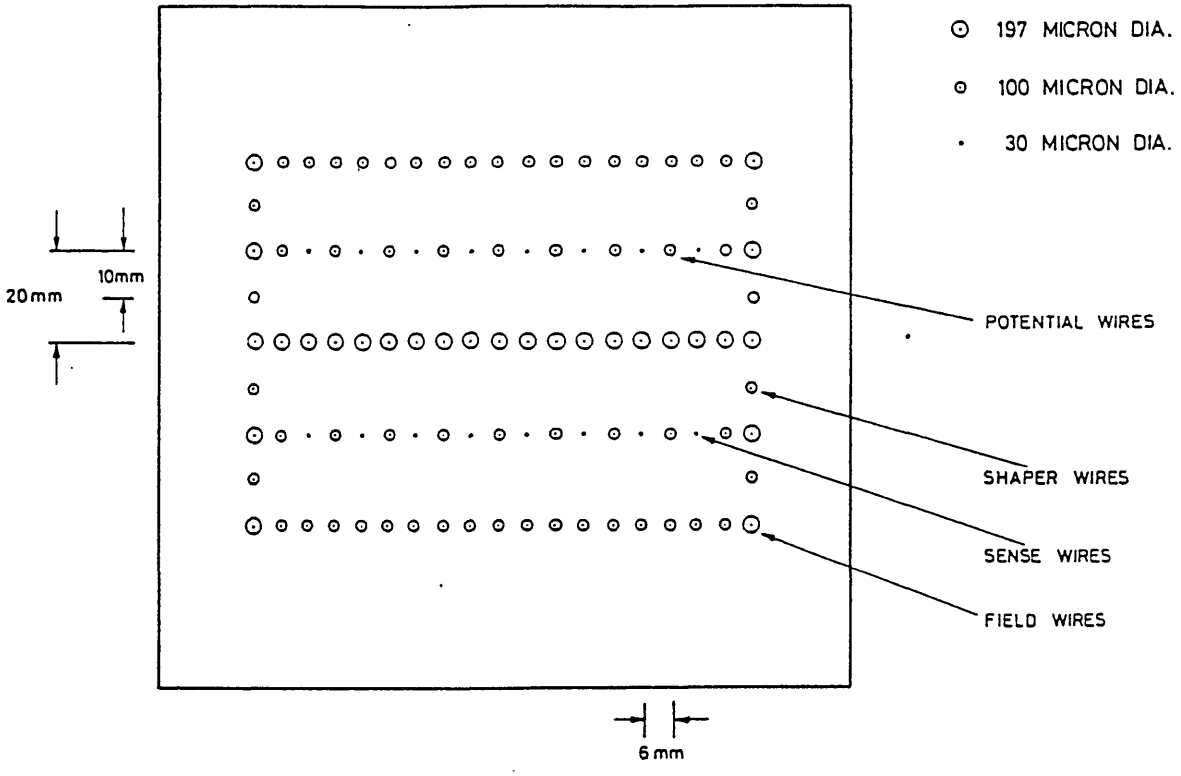


Figure 7.2: *Geometry of chamber.*

of ethanol inhibits the growth of whiskers on the field wires [52]. The chamber was tested in the DESY test beam facility using a 3 GeV electron beam that was fired into just one of the cells during a run. Triggering was provided by coincidences in plastic scintillator counters with the FADCs set in the continuous sampling mode and being stopped by the trigger. The chamber could be rotated in the horizontal plane relative to the beam direction. Track length samples for normally incident tracks were 5.6 mm on each sense wire, comparable to those of the CTD.

7.3 Chamber Pulses and Their Output from FADCs

When an ionizing particle passes through the chamber it liberates electrons, via Coulomb interactions, which drift to a sense wire under the influence of the electrostatic field. Close to the sense wire, avalanche multiplication occurs with the avalanche electrons being collected by the sense wire and the positive ions being repelled away. When any chamber of this sort operates in a particular voltage range the collected charge is proportional to the original charge deposited by the ionizing particle [45], so that ionization loss measurements can be made from the size of the signal picked up. The pulse from a drift chamber such as the one under test is characterized by a fast rising edge as the avalanche from the first electrons occurs, and a long tail that can be described by the function

$$f(t) = \frac{t_0}{t_0 + t} \tag{7.1}$$

where t is the time and t_0 is a constant, usually of the order of a few nanoseconds. This tail is a consequence of the drift of the positive ions away from the sense wire. The length of the tail can be shortened without affecting the rising edge by the use of a pole-zero filter in the post-amplifier, which filters out some of the frequency components not associated with the arrival of the electrons at the sense wire.

The signal from each sense wire was transmitted to the post-amplifiers and then converted to a digital readout by the FADCs. The dynamic range of the FADCs used was insufficient to cope with the large range of ionization picked up in this type of chamber. In order to increase their range the FADCs were driven in a non-linear mode in which 75% of the input signal was fed back to the resistor chain that formed the comparator reference [53], to produce an effective dynamic range of 8-bits at the expense of a loss of resolution of the largest input signals. The output from the FADCs consisted of a sequence of 6-bit amplitude words at intervals of 10 ns for each wire. The corresponding 8-bit amplitude was obtained using the conversion

$$\text{FADC8} = \frac{\text{FADC6}}{1 - 0.75 \times \text{FADC6}/64} \tag{7.2}$$

Prior to data taking, a pedestal was set to a signal level of 10 for each channel. In practice this level is modified by any noise present so later in the analysis it was determined on a channel-by-channel basis (see section 8.1). With the 8-bit conversion the signal range was from 0 to 255, quantized into units of 4 at the high end. Any overflows were identified and the signal was set to 255 for each overflow interval.

The rise times of the pulses, from the FADCs, are found to be typically 20→30 ns whilst the tail length without the filter is in the region of 130→150 ns which drops to about 60→70 ns when filtered. Pulse outputs without and with the pole-zero filter included are shown in figure 7.3. The crosses in the figure show the timing point assigned to each pulse (see section 7.4).

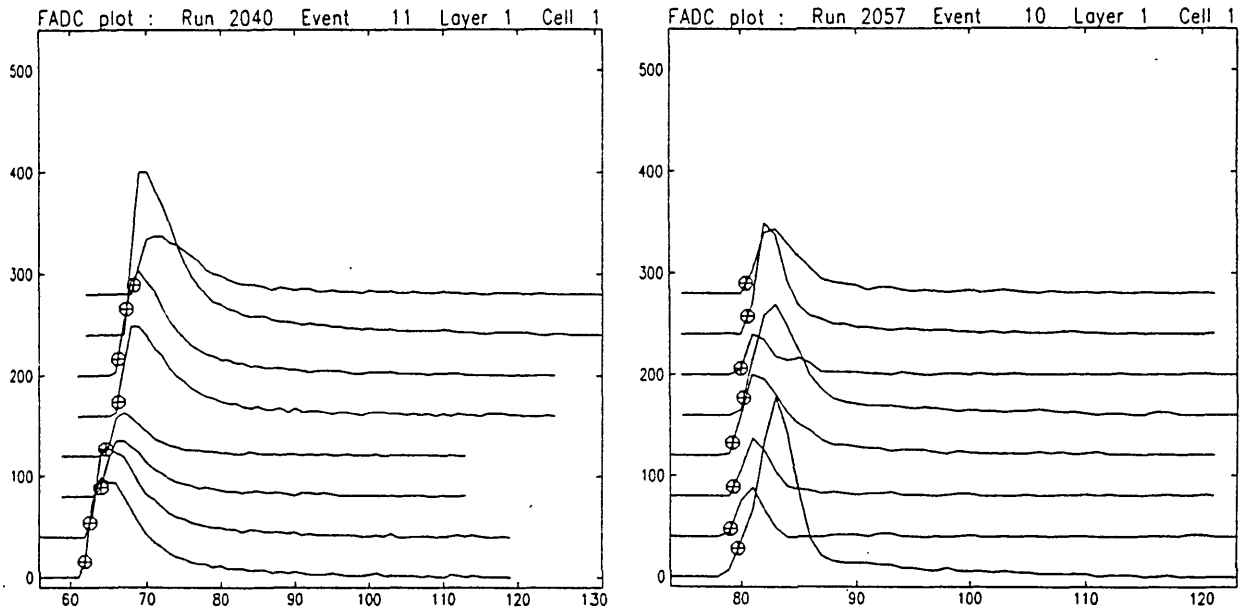


Figure 7.3: *FADC outputs without (run 2040) and with (run 2057) pole-zero filters for single track events. The abscissa shows the FADC interval number and the ordinate the linearized signal.*

7.3.1 Defining pulses in the FADC output

In order to determine whether a FADC channel readout contained one or more pulses, a method of defining a pulse was required, especially to distinguish genuine pulses from fluctuating noise. A pulse was defined as having the FADC signal rise by at least a value YCRIT over at least two FADC intervals (20 ns) and then to fall again by at least YCRIT, irrespective of the number of FADC intervals taken to do so. The minimum value before the pulse started was assigned as PIT with the FADC interval number being assigned as IPIT. The maximum value of the signal before it fell again was assigned as PEAK with the corresponding interval number being IPEAK. For a second pulse to be found on the wire the same criteria as for the first were applied with a second set of (I)PIT and (I)PEAK values. An example of a two-pulse FADC output is shown in

figure 7.4 along with the labelling of the (I)PITs and (I)PEAKs. For two pulses to be identified on a wire it can be seen that it is necessary that the signal from the first pulse has fallen by at least YCRIT before the rising edge of the second pulse affects the signal.

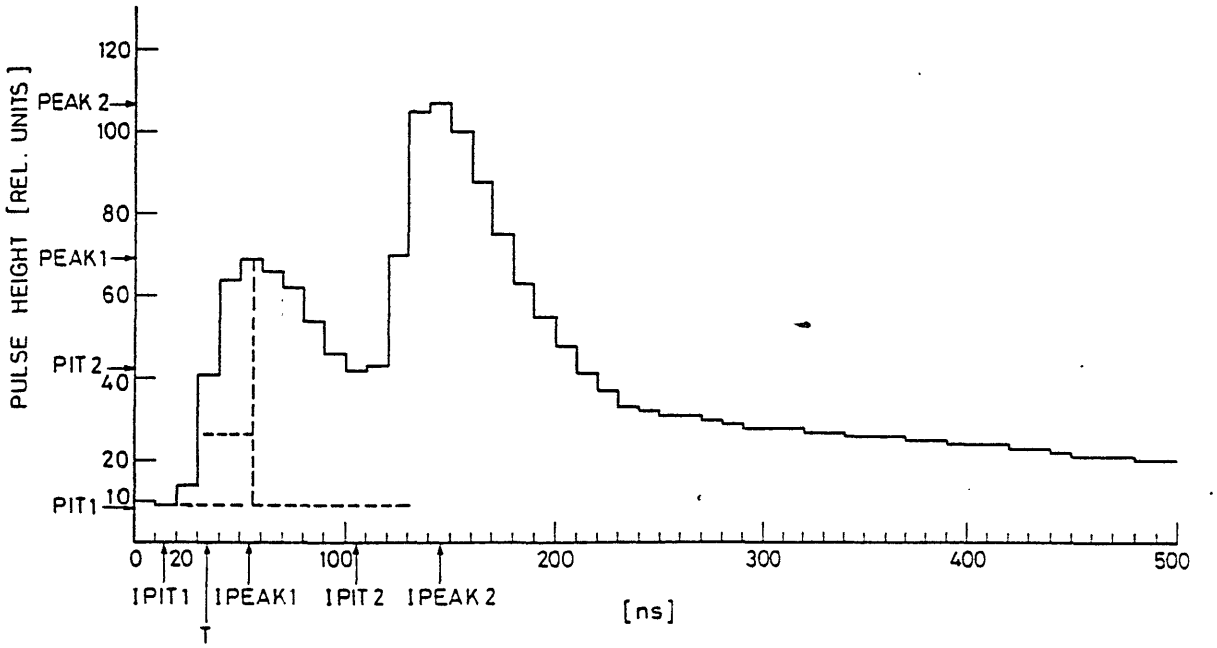


Figure 7.4: *FADC output from a two-pulse event.*

7.4 Determining Hit Positions and Spatial Resolutions

For each pulse, once defined, we can assign a time T from the timing base of the FADC signal. In the units of the FADC intervals a time is found by using an algorithm based in some way on the characteristics of the FADC pulse. From a previous analysis of single pulses in this chamber [54] it was found that the best algorithm to use was the Constant Fraction Discriminator or CFD. For the CFD the pulse time is given as the time value for which the amplitude of the signal is equal to the sum of the PIT value plus a constant fraction FRAC of the difference between the PEAK and PIT values, or if

$$\mathrm{CFD} = \mathrm{PIT} + \mathrm{FRAC} \times (\mathrm{PEAK} - \mathrm{PIT}) \tag{7.3}$$

then the time T is a projection of 'CFD' onto the timing base, given by

$$T = (i-1) + \left(\frac{\mathrm{CFD} - \mathrm{FADC}(i-1)}{\mathrm{FADC}(i) - \mathrm{FADC}(i-1)} \right) \tag{7.4}$$

where i is the FADC interval number and FADC is the signal amplitude for that interval. An investigation of the best value of FRAC to use for multi-pulses as well as studies of some of the other algorithms tested in reference [54] is performed in section 8.3. From a time found as in equation 7.4, a conversion is made to nanoseconds by multiplying by 10. By using the stop time of the FADC when it started reading the pulse, along with the time T_0 that corresponds to when tracks pass through the sense wire plane, a drift time is determined. This drift time corresponds to the time it takes the ionization to drift from the point of its production to the sense wire. This is converted to a drift distance using a field map of drift velocities for the chamber. For most of the chamber this drift velocity was found to be 50 ± 1 μm/ns as expected for the gas mixture used. From this drift distance we can assign two hits to the chamber, one either side of the sense wire as we do not know, without prior knowledge of the test beam position, which side of the sense wire the ionization drifted from.

The best timing algorithm is determined by looking at the spatial resolutions that result from using each particular algorithm and seeing which gives the smallest value. Spatial resolutions are found by fitting straight tracks to the hits (there being no magnetic field to bend our tracks). In each event there should be just one track found on each side of the sense wire plane. As the test beam position was known the real track

is also known and only the hits on this track were looked at. The spatial resolution for each wire was obtained by finding the residual distance, along the drift path, from the found track to the hit associated with the track. The residual was then weighted as a function of the position of that hit on the track in relation to all the hits found on the track. The weighted residuals were then plotted for each wire, a Gaussian was fitted to the distribution and the width of the Gaussian gave us the resolution for that wire. The resolution of the cell was taken as the average of the resolutions for all eight wires. By calculating the resolution for each wire separately we were not affected by any uncertainties in the wire positions as this merely shifted the whole distribution without changing its width.

7.5 Determining the dE/dx Resolution

The size of the signal from the FADC is a measure of the size of the avalanche occurring at the sense wire which in turn is proportional to the amount of ionization produced by the particle as it is 'sampled' by each wire. Knowing this, we can use the pulses to make dE/dx measurements. Also, as we are using a mono-energetic beam of identical particles (3 GeV electrons), we need only consider a dE/dx distribution that is a single Landau function [45], the tail of which is the result of high energy δ-rays (see section 6.4 for an explanation of these).

To determine the best algorithm to measure the dE/dx sample from the pulses we needed to assess the dE/dx resolution performance of the chamber. As the dE/dx losses to a single wire were governed by a Landau distribution, a measure had to be made of the truncated average dE/dx, or $\langle$dE/dx$\rangle$ value over a number of samples. As the CTD will have a maximum of 72 dE/dx samples for a track, the chamber's performance was assessed by using 72 pulse size measurements to find a single $\langle$dE/dx$\rangle$ value. To calculate the dE/dx resolution, 72 measurements of pulse sizes were made with one of the algorithms and the highest 25% or 18 values were discarded to remove the Landau tail and possibly some double pulses resolved as only a single pulse. The average from these 54 values was calculated and stored. As the dE/dx resolution is found as the width of the distribution of $\langle dE/dx \rangle$ / $\langle E \rangle$, the first 50 $\langle$dE/dx$\rangle$ values were stored and then the average of these 50 were used to scale the plotting by $\langle$E$\rangle$. This had the advantage that we did not have to alter the plotting limits for the different dE/dx algorithms being tested which would have different values for their dE/dx measurements. Once all the scaled dE/dx values were plotted, a Gaussian was fitted to the distribution and the resolution was taken to be the width of the Gaussian.

Chapter 8

Multi-Pulse Performance of the Drift Cell

Investigations have been made into the multi-pulse performance of the rectangular test drift chamber. Studies were made upon the two-pulse resolution, spatial and dE/dx resolutions and their behaviour in the situation of two pulses being present on the sense wires, with varying separations between the pulses.

When two particles pass through the same cell the sense wires will pick up two pulses which, providing they are far enough apart, will be seen in the FADC output and resolved by the pulse finding algorithm as two pulses (see figure 7.4 for an example). The ionization picked up by the sense wire at any moment will be an accumulation of the ionization from the separate particles. For three or more particles, each will contribute its own ionization which will again be resolved if each is far enough apart. A study of the multi-pulse performance of the chamber was performed by taking single pulse events and adding together the pulses to simulate double pulses. Using their found timings and dE/dx values before the addition, the effect of the pulses on each other as a function of separation and relative pulse size could be studied. The most serious problem in adding together pulses from separate events was that the simulated double pulse had two noise sources, one from each event, whereas genuine double pulses only have one noise source. This resulted in the second pulse 'seeing' more noise than the first when they were sufficiently separated.

8.1 Adding Together the Pulses

The selection criteria for an event to be used in the simulation of double pulses were that the event was required to have a single pulse on each of the eight wires of the cell through which the beam passed, and that the drift distances for the eight resulting hits were between 5 and 17 mm. This is the region in which the spatial resolution for single pulse events was on a plateau [54]. For distances closer than 5 mm there were not enough events to determine whether resolutions were on the plateau, and for distances further than 17 mm diffusion of the ionization degraded the resolutions.

If these criteria were passed, the output from each channel was stored with the pedestals subtracted. The pedestal for each channel was calculated by finding the average value of the output for the last five FADC intervals for that channel. These pedestals were also stored along with the times and dE/dx values calculated for each single pulse. The times were stored in the units of the FADC intervals where the first FADC interval for each channel was referred to as '1'. The output from all the channels were then added together, channel by channel with the output from the previous event that had passed our criteria and been stored. This was done many times for the two events, each time incrementing the FADC interval number of the new event to which the first FADC interval of the old event would be added. In this way the two sets of pulses became further separated so that the effect of the separation could be studied. Owing to the way the FADC outputs were written, pulses generally occurred in the same FADC intervals so that doing things in this manner resulted in double pulse events apparently consisting of two parallel tracks.

When the two separate signals were added together, one of the pedestals was added back onto the signal so that the level of the signals was as would be for a genuine double pulse, and the value in each interval was transformed into an integer 6-bit word using the conversion

$$\mathrm{FADC6} = \mathrm{NINT}\left(\frac{\mathrm{FADC8}}{1 + 0.75 \times \mathrm{FADC8}/64}\right) \tag{8.1}$$

where NINT gives the nearest integer value. This was then converted back into an 8-bit word using equation 7.2. In this manner, we used only the signal sizes permitted when driving the FADCs non-linearly and feeding back 75% of the input. The pedestal was then once again subtracted.

Each time the pulses from the separate events were added together, the simulated FADC outputs were run through the pulse-finding algorithm to recognise the pulses. When the two pulses are directly on top of each other, only one pulse is expected to be found by the algorithm. So if two pulses were found on any of the wires in this situation then the new event was rejected and a search for the next event to satisfy the selection criteria was performed. This way events with too much noise or extra pulses with heights just below the value of YCRIT were rejected. As with the single pulse events, for each pulse found the time was found in the FADC interval units and then converted to a drift time in nanoseconds, by multiplying by 10. To convert to a drift time, as pulses from separate events were being used, the stop time of the FADCs from the latter of the single pulse events was used. To convert to a drift distance, the average drift velocity of 50 μm/ns was used, as the fieldmap was inappropriate since in reality the separate pulses came from different parts of the chamber. Drift times, drift distances and dE/dx measurements for the one or two pulses found were stored for each channel, along with whether or not two pulses had been found. An analysis of the simulated double pulses was then performed before the pulses were separated further. Once all the separations required had been made, the single pulse information from the latest event overwrote the previous 'old' data and a new event was found that passed the selection criteria.

For the multi-pulse analysis the terms defined in table 8.1 will be used.

Term	Definition
T1REAL	Time found for first pulse as a single pulse
T2REAL	Time found for second pulse as a single pulse
T1MEAS	Time found for first pulse after addition of pulses
T2MEAS	Time found for second pulse after addition of pulses
P1REAL	Pulse size found for first pulse as a single pulse
P2REAL	Pulse size found for second pulse as a single pulse
P1MEAS	Pulse size found for first pulse after addition of pulses
P2MEAS	Pulse size found for second pulse after addition of pulses
TDREAL	T2REAL−T1REAL
TDMEAS	T2MEAS−T1MEAS
DELTT1	T1REAL−T1MEAS
DELTT2	T2REAL−T2MEAS
FACTP1	P1REAL/P1MEAS
FACTP2	P2REAL/P2MEAS

Table 8.1: *Definitions of terms used in multi-pulse analysis*

Figure 8.1 shows the FADC output from two single pulse events before and after they were added together to simulate a double pulse. The upper diagrams show the two separate events whilst the lower left-hand diagram shows the FADC output for when the pulses are between 40 and 50 ns apart. As this diagram clearly shows, at this sort of separation the pulse finding algorithm fails to resolve two pulses for most of the channels. The lower right-hand diagram shows the pulses when they are well separated and have returned to their single pulse shapes.

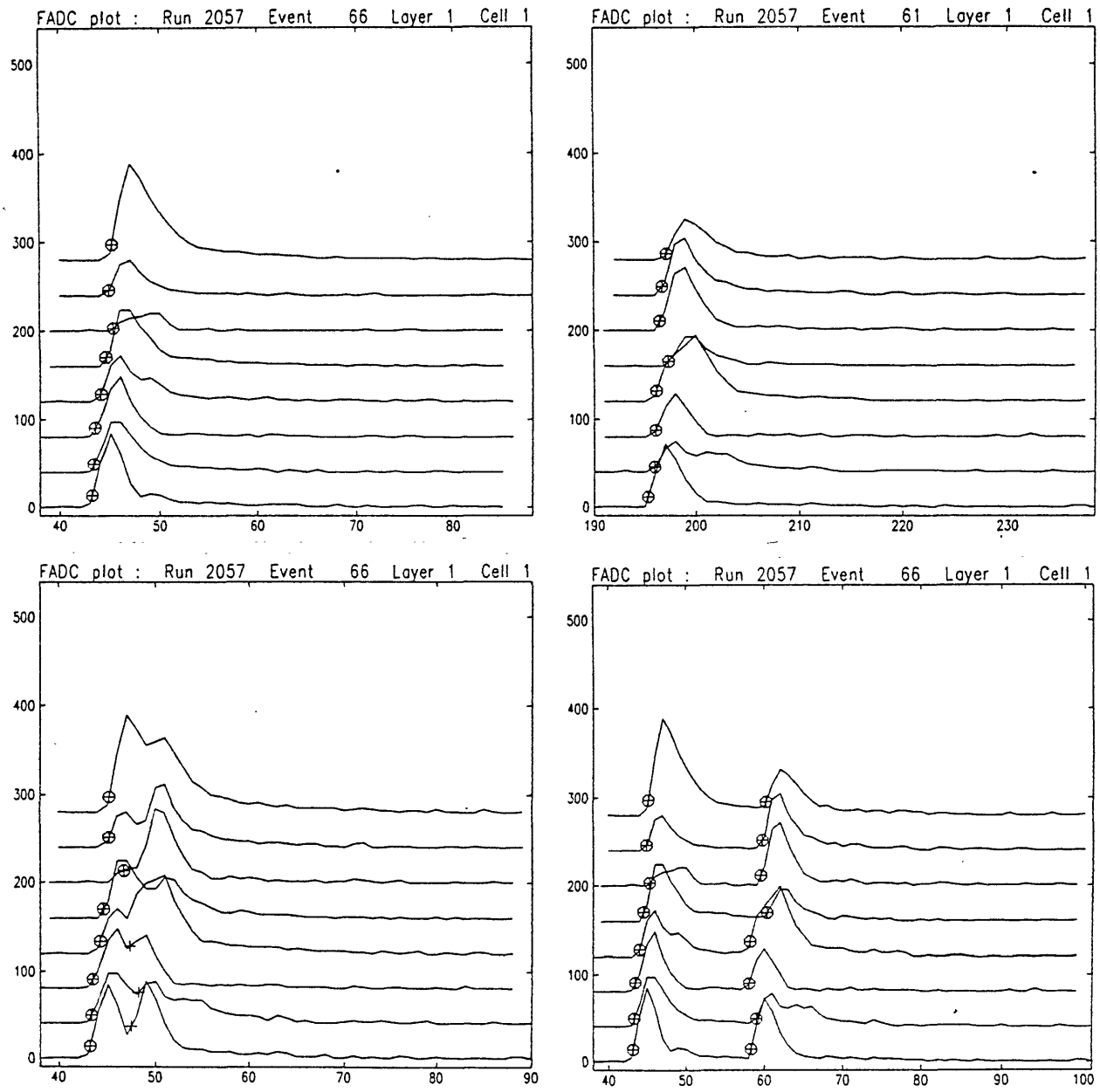


Figure 8.1: *FADC outputs before and after simulating double pulses.*

8.2 Two-Pulse Resolution Efficiency

The efficiency with which the pulse-finding algorithm could resolve the two pulses was found by seeing what fraction of our simulated double pulse events were found with two pulses. This is clearly dependent upon the separation of the two pulses and so the fraction of two-pulse events found was plotted as a function of the pulse separation. Figure 8.2 shows such a plot for pulses with and without the pole-zero filter. As is shown, the use of the pole-zero filter greatly improves the efficiency for finding two pulses when the pulses are close together. We can define the two-pulse resolution as the separation time for which we are 50% efficient at resolving the two pulses as shown in figure 8.2.

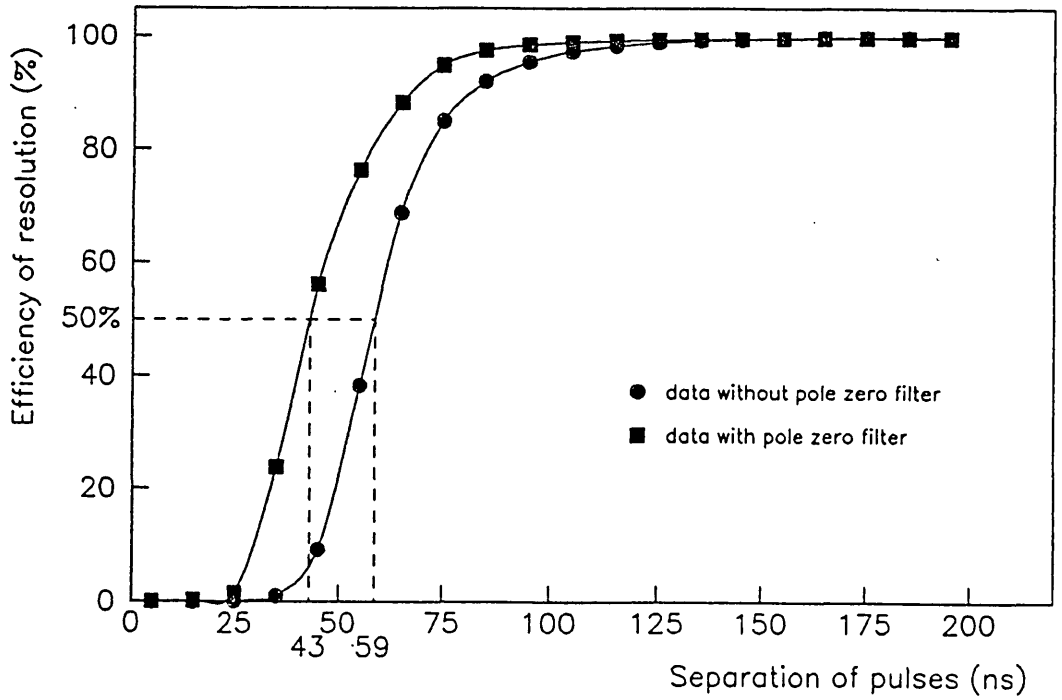


Figure 8.2: *Efficiencies for finding two pulses as a function of pulse separation for pulses with and without pole-zero filtering.*

The two-pulse resolution gives an indication of the performance of the pulse-finding algorithm. In figure 8.3 is plotted the two-pulse resolution as a function of the size of YCRIT used. As we found that for the same value of YCRIT the filtered pulses improved the two-pulse resolution (figure 8.2 shows the results for YCRIT=15), we tried splitting the value of YCRIT, to see whether this might improve the two-pulse

resolution further. Below a FADC output of 50 we used a value YCRIT1, and above 50 another value YCRIT2=INT(YCRIT1/2) was used where INT gives the rounded-down integer value. As can be seen in figure 8.3 the smaller the value of YCRIT, the better the two-pulse resolution. If YCRIT gets too small, however, we will start to introduce spurious hits from noise becoming misidentified and so ultimately the value of YCRIT chosen in a situation will depend upon the extent of the noise. In all cases the filtered pulses give a better two-pulse resolution. For the non-filtered pulses though, we do see that splitting the YCRIT value used does improve the two-pulse resolution, although never as well as the filtered pulses for any value of YCRIT1. For the filtered pulses the effect of splitting the YCRIT values is minimal.

To avoid picking up noise hits, all further multi-pulse investigations were performed using a single YCRIT value of 15 for the filtered pulses and split YCRIT1/YCRIT2 values of 15/7 for the non-filtered pulses, resulting in two-pulse resolutions of 2.15 mm and 2.65 mm respectively when the average drift velocity of 50 μm/ns was applied.

A study was also made of the effect of the relative sizes of the first and second pulses upon the two-pulse resolution. The pulse size was measured using the PIT→PEAK algorithm (see section 8.4). Figure 8.4 shows the resulting two-pulse resolutions. We see that the best two-pulse resolutions occur when the pulses are of roughly equal sizes. As one pulse gets much bigger than the other, the two-pulse resolution worsens. When the first pulse is bigger than the second we get a worse resolution than in the reverse situation. This can be understood by the fact that for the pulse-finding algorithm to distinguish a second pulse, the signal from the first pulse has to have dropped by YCRIT before the signal from the second pulse rises by YCRIT. For a large first pulse, the falling tail signal has to be compensated by a large rising edge for the second pulse, which will not occur if the second pulse is small relative to the first pulse. For large second pulses, the falling tail signal of the first pulse will be swamped by the rising edge of the second pulse so that the FADC signal will not appear to have fallen by YCRIT if the first pulse is relatively small. In this case the second pulse is not found by the pulse-finding algorithm. In both cases the pulses need to be further apart before the signal drop and rise is large enough to distinguish the pulses, resulting in worse two-pulse resolutions.

As using the pole-zero filter greatly improves the multi-pulse resolution and it is expected that it will be used in the CTD, all further analysis will deal with just the data taken with the pole-zero filter included.

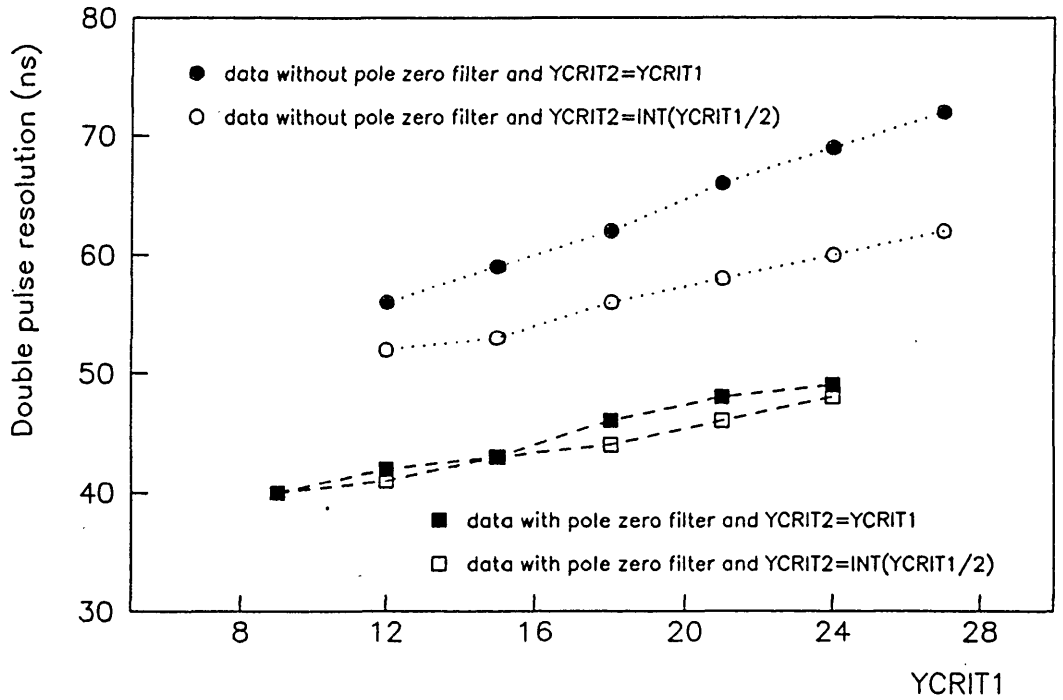


Figure 8.3: *Two-pulse resolutions as a function of YCRITs for pulses with and without pole-zero filtering.*

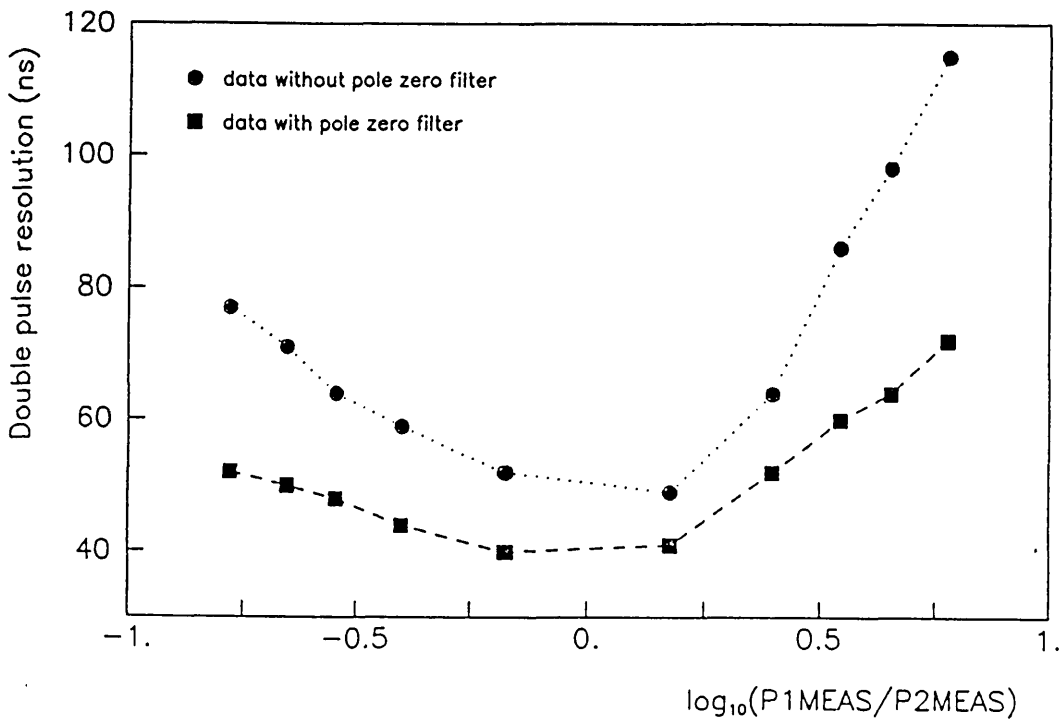


Figure 8.4: *Two-pulse resolutions as a function of relative pulse sizes for pulses with and without pole-zero filtering.*

8.3 Two-Pulse Spatial Resolution

A study was made of how various timing algorithms perform with regard to double pulses. This was done by looking at the spatial resolutions calculated as described in section 7.4. To ensure that each track was fitted to the correct hits, the drift distances associated with the second pulses were shifted a large distance so that there would be no confusion in the track finding. The typical shapes of the distribution of spatial resolution as a function of the separation of the two pulses are shown in figure 8.5 for both the first and second pulse. If only one pulse was resolved on a wire then the residual was treated as belonging to the first pulse. As the pulses were added in such a way that the resulting tracks appeared parallel, the effect of different pulse separations upon the spatial resolutions within an event has been eliminated. This means that the ensuing resolutions for each separation of pulses are just the result of the effect of the first pulse upon the second for that particular separation.

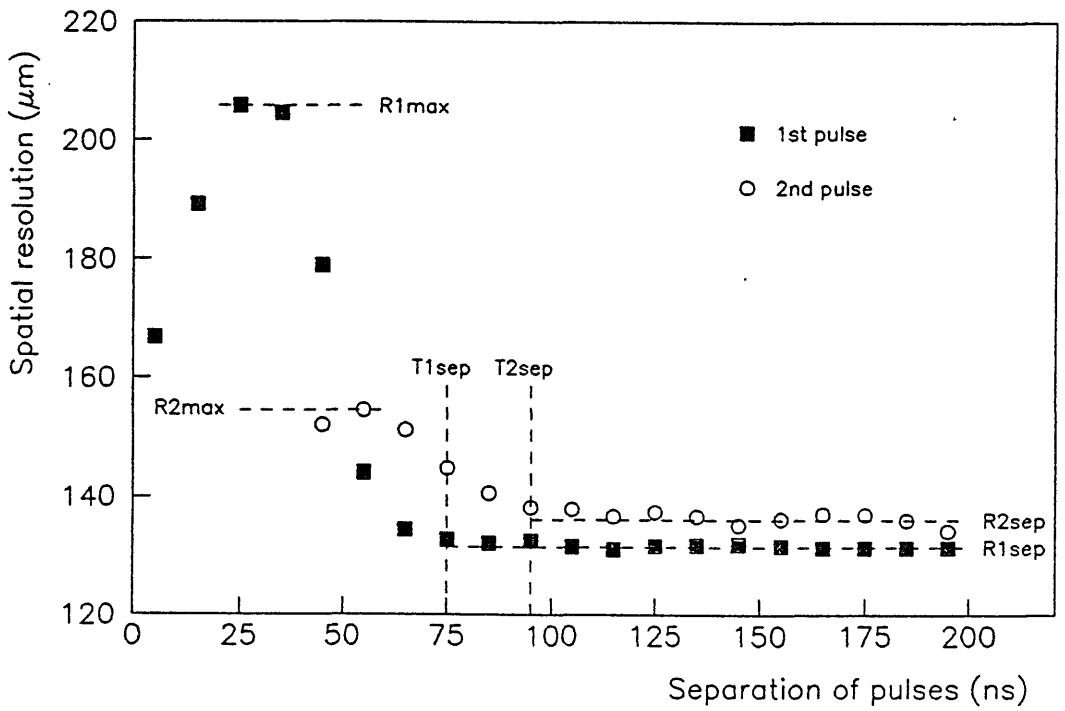


Figure 8.5: *Typical distribution of spatial resolutions as a function of pulse separation for the first and second pulses.*

In order to assess the multi-pulse performance of the chamber and timing algorithms with regard to the spatial resolution we have used the characteristics of the spatial resolution plots described in table 8.2 and shown graphically in figure 8.5. We show in

table 8.3 the resulting two-pulse spatial resolution characteristics for the CFD algorithm (see section 7.4) using various fractions along with other timing algorithms that appeared to perform well in the previous single pulse analysis [54]. It should be noted that the actual resolutions obtained in this and the previous work cannot be compared as the data were taken with different chamber conditions and the calculation of the residuals was performed differently, along with the fact that we have used a generic value for the drift velocity.

Term	Definition
R1max	Largest resolution for first pulse
R1sep	Resolution for first pulse as a single pulse
T1sep	Time for which first pulse resolution reaches that of single pulse
R2max	Largest resolution for second pulse
R2sep	Resolution for second pulse as a single pulse
T2sep	Time for which second pulse resolution reaches that of single pulse

Table 8.2: *Characteristics of spatial and dE/dx resolution plots*

Timing Algorithm	R1sep	R1max	T1sep
Constant fraction 2%	156 μm	180 μm	55 ns
Constant fraction 10%	131 μm	188 μm	75 ns
Constant fraction 16%	131 μm	206 μm	75 ns
Constant fraction 20%	133 μm	218 μm	65 ns
Constant fraction 33%	137 μm	267 μm	65 ns
Difference of samples[55]†	131 μm	188 μm	75 ns
Interpolation on differences	132 μm	215 μm	85 ns
Differentiated constant fraction 50%	148 μm	360 μm	95 ns

Timing Algorithm	R2sep	R2max	T2sep
Constant fraction 2%	187 μm	196 μm	55 ns
Constant fraction 10%	141 μm	162 μm	95 ns
Constant fraction 16%	136 μm	154 μm	95 ns
Constant fraction 20%	136 μm	154 μm	85 ns
Constant fraction 33%	139 μm	149 μm	85 ns
Difference of samples[55]†	141 μm	162 μm	95 ns
Interpolation on differences	141 μm	214 μm	95 ns
Differentiated constant fraction 50%	149 μm	225 μm	85 ns

† different weightings were used from those in reference

Table 8.3: *Multi-pulse spatial resolution performance for various timing algorithms*

We can see by studying table 8.3 that there are conflicting optimizations using the CFD algorithm for the first and second pulse. When considering three or more pulses the first pulse here acts as a preceding pulse and the second as a preceded pulse. In the case of three or more pulses, the second pulse will be affected by both the first and third pulses as a preceded and preceding pulse. When the preceded pulse, or second pulse in this case, is too close to the first to be resolved, it is found that a smaller fraction is necessary to reduce the spatial resolution of the apparent single pulse. The worst spatial resolution occurs for the maximum separation where the majority of events are still seen as single pulses. Here, the rising edge of the apparent single pulse is at its widest, and so the movement in a timing point on this rising edge is at its largest. By having the timing point lower down the rising edge, the second pulse, which is still 30 ns or so behind the first pulse, gives a smaller contribution to the total rising edge at this height. Comparing figure 8.5 with figure 8.2 which shows the efficiency for resolving two pulses, we see that the first pulse spatial resolution reaches the level of that of the single pulse when the efficiency for resolving two pulses is almost 100%. This suggests that any degradation in the first pulse spatial resolution is mainly due to double pulses being resolved as single pulses. For the second pulse, the effect of the tail of the first pulse on the timing point has a greater effect the lower the point is down the rising edge, as the IPIT assignment can be greatly altered which only avoids problems with timings when we are far enough up the rising edge. Also, the gradient of the rising edge increases the further up the pulse we are, thereby minimizing the movement of the timing point when larger fractions were used. So for a better resolution for the first or preceding pulse using the CFD algorithm, the need is for a lower fraction, whilst for the second or preceded pulse a higher fraction is required to improve the spatial resolution. Despite these shortcomings in the CFD algorithm, it still appears to work as well as, if not better than, the other algorithms looked at. The separation of pulses required before the spatial resolutions reach the values obtained by single pulses is at least as short as for the other algorithms.

The discrepancy in the single pulse spatial resolutions between the first and second pulses, measured when the separation of the pulses is sufficiently large, is due to the additional noise source that exists beyond the end of the first pulse. This noise would not exist in genuine multi-pulse events. This difference, however, does give an indication of the performance of the algorithm when a certain noise level is present and we see that the CFD algorithm becomes less sensitive to noise as the fraction is increased, as

would be expected in the same way that the second pulse is affected by the tail of the first.

As a compromise all further timings were taken using the CFD algorithm with the fraction of 16%.

8.4 Two-Pulse dE/dx Resolution

Various algorithms used to measure the pulse size and thereby the dE/dx loss of the particle passing through the chamber were studied with the view to minimizing both the dE/dx resolution and the effect of the pulses upon each other. The dE/dx resolutions for the algorithms studied were calculated as explained in section 7.5. The typical shape of the distribution of dE/dx resolution as a function of the separation of the two pulses is shown in figure 8.6 for both the first and second pulse. As with the spatial resolution when only one pulse was resolved, the pulse size measured was taken as belonging to the first pulse. What should be remembered for such a case is that in the real situation to be encountered by the CTD, the tracks are unlikely to be parallel and so for double pulses resolved as single pulses their measured pulse size, if included as one of the track samples, is going to shift the $\langle dE/dx \rangle$ found for the track it gets associated with. To avoid this, the pulse can be excluded as a dE/dx sample by intercepting the two tracks to find any hits on either track which might be an unresolved double pulse. If the unresolved double pulse is due to different beam crossings then a problem occurs when the two pulses are directly on top of each other, as the only way to have the sample excluded from the $\langle dE/dx \rangle$ calculation for the track would be if it became included in the top 25% of the dE/dx samples and so be cut. If the two pulses are just unresolved then the pulse can be identified by its unusually large width and therefore removed from the dE/dx samples on this criteria.

The dE/dx resolution is dependent upon the value of $\langle E \rangle$ which in turn is dependent upon the 'contamination' of the measurement by the other pulse. So by plotting the value of $\langle E \rangle$ found for each pulse separation divided by the average value of E when the two pulses are sufficiently separated, $\langle E_{sep} \rangle$, as a function of pulse separation, we can see the extent of the 'contamination' for each algorithm. An example of this plot is shown in figure 8.7. As with the spatial resolutions, in order to assess the multi-pulse performance of the chamber and pulse size algorithms with respect to the dE/dx resolution we have used the same terms shown in table 8.2 to describe the characteristics shown graphically in figures 8.6 and 8.7. The single pulse dE/dx resolutions, R1sep and R2sep, were found by using five dE/dx resolutions for separations greater than 200 ns and finding the mean of these. As there were large fluctuations in the dE/dx resolutions due to limited statistics we also calculated a standard deviation from these five measurements to get a measure of the statistical fluctuation.

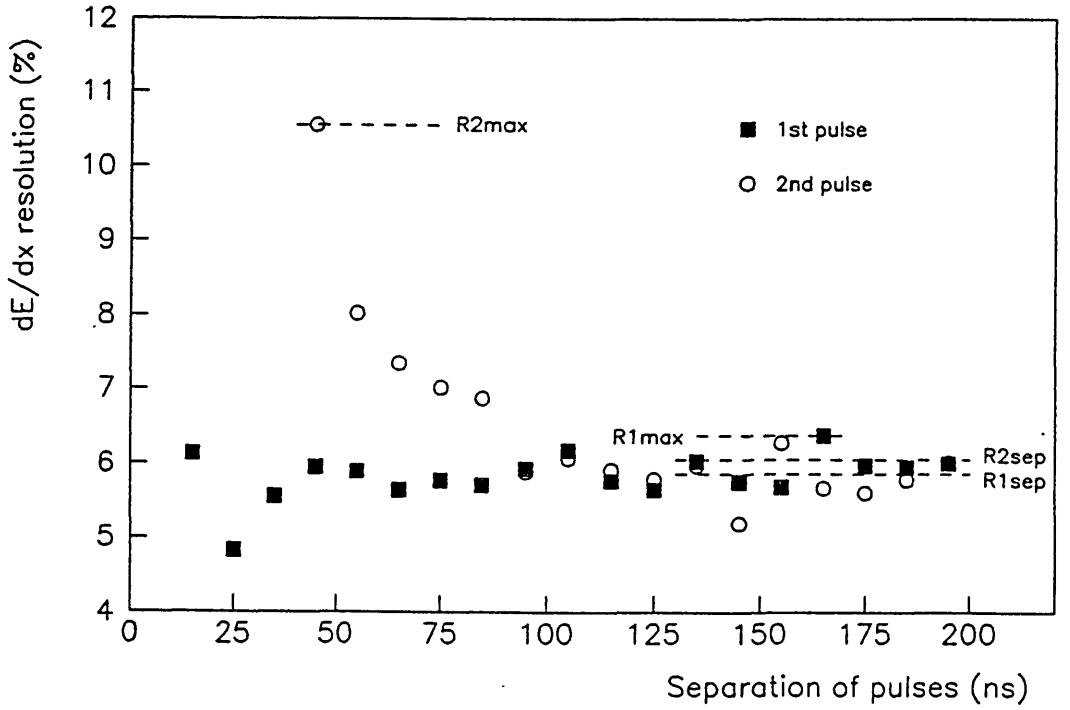


Figure 8.6: *Typical distribution of dE/dx resolutions as a function of pulse separation between the first and second pulses.*

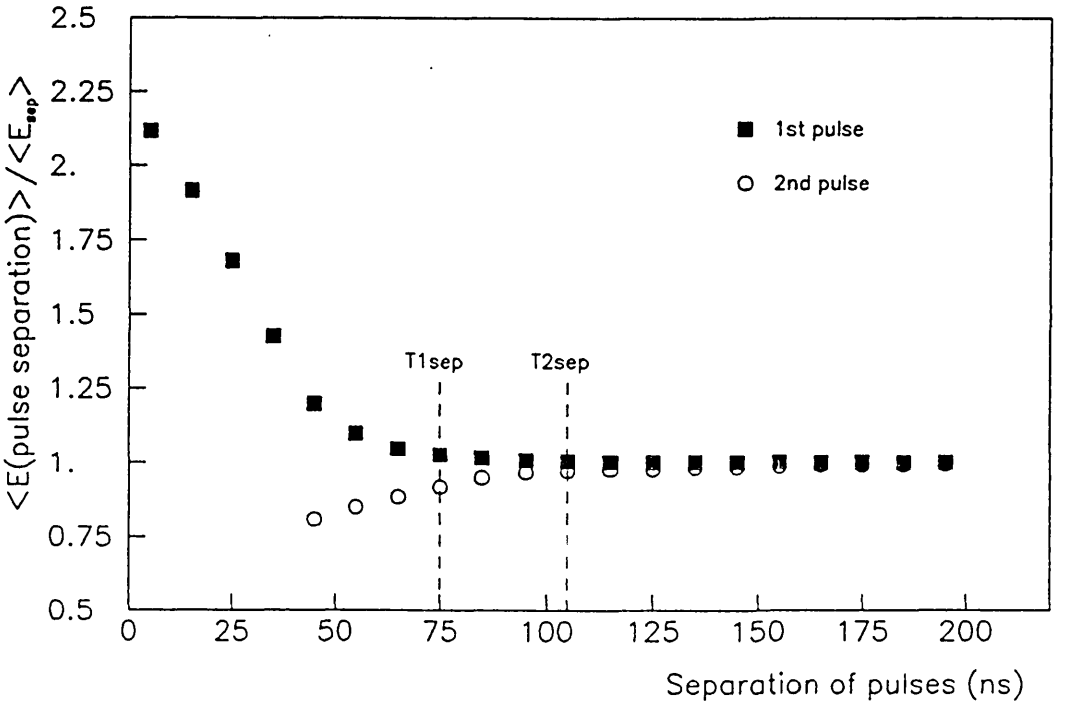


Figure 8.7: *Scaling factors used in dE/dx resolutions as a function of pulse separation between the first and second pulses.*

Pulse Size Algorithm	R1sep	R1max	T1sep
Area under rising edge	6.2%±0.2%	7.4%	85 ns
Area under rising edge > CFD	6.2%±0.3%	8.0%	85 ns
Area of pulse > CFD	5.7%±0.3%	8.4%	115 ns
PIT→PEAK	5.9%±0.1%	6.2%	75 ns
PIT→PEAK + 4 bins in tail	5.9%±0.2%	6.3%	85 ns
PIT→PEAK + 9 bins in tail	6.0%±0.3%	6.4%	125 ns
BASELINE→PEAK	5.9%±0.2%	6.4%	75 ns
BASELINE→PEAK + 4 bins in tail	5.9%±0.1%	6.5%	85 ns
BASELINE→PEAK + 9 bins in tail	5.8%±0.2%	6.6%	125 ns

Pulse Size Algorithm	R2sep	R2max	T2sep
Area under rising edge	6.3%±0.3%	10.0%	125 ns
Area under rising edge > CFD	6.3%±0.1%	11.2%	125 ns
Area of pulse > CFD	5.7%±0.2%	13.6%	175 ns
PIT→PEAK	6.1%±0.2%	10.6%	105 ns
PIT→PEAK + 4 bins in tail	6.0%±0.2%	12.9%	165 ns
PIT→PEAK + 9 bins in tail	6.1%±0.2%	12.8%	>200 ns
BASELINE→PEAK	5.9%±0.4%	6.9%	175 ns
BASELINE→PEAK + 4 bins in tail	5.8%±0.3%	6.6%	>200 ns
BASELINE→PEAK + 9 bins in tail	5.7%±0.2%	6.6%	>200 ns

Table 8.4: *Multi-pulse dE/dx resolution performance for various pulse size algorithms*

Table 8.4 shows the dE/dx resolutions for various pulse size measuring algorithms. The BASELINE is the zero level of the FADC output after subtraction of the pedestal. For the first pulse the PIT and BASELINE algorithms are essentially the same. For the single pulse dE/dx resolutions we find that within the statistics of our results there is little to choose from between any of the algorithms. It should be noted that due to the limited statistics the graphs are not as well behaved as for the spatial resolutions. This can be seen by comparing figure 8.6 with figure 8.5.

R1max does not seem to be a significant characteristic of the distribution, occurring at different pulse separations for different algorithms, and appearing to be no more than an indication of the statistical fluctuation in our results. The encouraging indication of these results is that dE/dx measurements can be made from single FADC interval readings of the peak value of the signal. This means that for the single bin algorithms we have a minimal pulse separation effect as shown by T1sep and T2sep. It appears that sufficient dE/dx information is contained in just the pulse height measurement.

This could be because the tail of the preceding pulse is not as well behaved as would be required to see an improvement in the outcome of the dE/dx resolution. It was expected that the inclusion of the tail of the pulse would improve the resolution as the relative precision of the measurement of any single dE/dx value would be improved. Any improvement though, is likely to have been swamped by the limited statistics being used to determine the dE/dx resolutions. This arises from the fact that 72 pulses are required for a single point in the plot used to determine the dE/dx resolution, compared with the single pulse required to determine the spatial resolutions. Averaging over 72 samples may have also removed effects such as noise, as can be seen by comparing R1sep and R2sep, the latter having the additional noise source contained in its calculation.

Although R2max is a measure of the effect of the first pulse upon the second pulse, in contrast to R1max which appears to be nothing more than the maximum of a statistical fluctuation, we are not really able to compare the algorithms by their R2max values as $\langle E \rangle$ used in calculating the dE/dx resolutions is affected by the first pulse. For instance, $\langle E \rangle$ appears to be a lot smaller for the PIT→PEAK algorithm than for the BASELINE→PEAK algorithm for a given pulse separation when the pulses are overlapping although it would be the same when the pulses are well separated. This means that $\langle E \rangle$ is artifically lower for the PIT→PEAK algorithm and artifically higher for the BASELINE→PEAK algorithm, thereby raising the calculated dE/dx resolution for the former and lowering it for the latter.

One problem that the BASELINE→PEAK algorithm encounters in the artificial situation of this analysis is that by summing signals we are including the extra noise source the simulation introduces. The effect of this manifests itself by making the values of T2sep for all the BASELINE algorithms much larger than for the corresponding PIT algorithms, as the value of $\langle E \rangle$ takes longer to approach its single pulse value *from above*, due to the additional noise source added to it. With regard to the second pulse performance, comparisons should not really be made between these particular algorithms until corrections have been made to the pulse sizes.

8.5 Correcting the Timings and Pulse Sizes

Corrections to the second pulses based on the separation of the pulses is very desirable, as in reality the general situation will be that tracks will not be parallel, so that from hit to hit the shift in time will vary. This worsens the resolution of the hits affected by a far greater amount than is shown in figure 8.5. The purpose of the pulse size measurements is to identify particles by the average dE/dx value of their tracks. Therefore a correction to a pulse size measurement is also desirable so that we do not shift this average value.

As well as being dependent upon the separation of the two pulses, where the further the pulses are apart the smaller is the effect of the first pulse upon the second, the corrections to be made could also possibly be dependent upon the relative sizes of the two pulses. We have shown this to be the case with double pulse resolutions in section 8.2. The question is whether including the additional dependence of relative pulse size will improve the spatial and dE/dx resolutions over those achieved using just the pulse separation dependent corrections.

8.5.1 Finding the Corrections

To find the corrections to be applied to the second pulse we plotted for pulse separations quantized into the FADC interval units of 10 ns, DELTT2 and FACTP2 as functions of $\log_{10}$(P1MEAS/P2MEAS). For all these quantities the measured values were used, as opposed to the 'real' single pulse values, as in real multi-pulse events these would be the only quantities we would have access to. For each $\log_{10}$(P1MEAS/P2MEAS) interval the average values $\langle$DELTT2$\rangle$ and $\langle$FACTP2$\rangle$ were used as the corrections to be made on the measured time and pulse size so that:

$$\mathrm{T2}_{corrected} = \mathrm{T2MEAS} + \langle \mathrm{DELTT2} \rangle \tag{8.2}$$

$$\mathrm{P2}_{corrected} = \mathrm{P2MEAS} \times \langle \mathrm{FACTP2} \rangle \tag{8.3}$$

In this way we were to some extent cancelling T2MEAS and P2MEAS as:

$$\mathrm{DELTT2} = \mathrm{T2REAL} - \mathrm{T2MEAS}$$

$$\mathrm{FACTP2} = \mathrm{P2REAL/P2MEAS}$$

An indication of how well the correction may work is given by the r.m.s. of the distribution which gives a value for the width σ for each $\log_{10}$(P1MEAS/P2MEAS) interval. Figures 8.8 and 8.9 show the distributions of ⟨DELTT2⟩ and σ(DELTT2) using the PIT→PEAK and BASELINE→PEAK algorithms respectively to measure the pulse sizes. The corresponding distributions for the FACTP2 corrections are shown in figures 8.10 and 8.11. In all the figures the corrections are for measured separations of pulses between 40 and 50 ns.

Also shown on all these plots are the values found for all pulse sizes, or in other words, the pulse size independent corrections and their widths calculated as functions of only the pulse separations. Studying the width plots for FACTP2 and comparing them to figure 8.12 which shows the frequency distributions of the measured relative pulse sizes using the two pulse size algorithms for the same pulse separations, we see that the corrections using the PIT→PEAK algorithm work well. This can be seen from the fact that the vast majority of pulse size combinations have σ(FACTP2) smaller than the pulse size independent correction. For the BASELINE→PEAK algorithm the fraction of combinations with σ(FACTP2) smaller than for all pulse sizes is less than for the PIT→PEAK algorithm but still forms the majority of pulses. Looking at the effect of pulse size corrections upon the time of the second pulse, we find by comparing the σ(DELTT2) distribution with figure 8.12 that although for the majority of pulse combinations σ(DELTT2) is smaller than for the pulse size independent corrections, it is not much more than half of the total number of pulse combinations examined for this particular pulse separation. This suggests that including the dependence of relative pulse sizes when correcting the timings of the second pulses is not effective.

8.5.2 Effect of Corrections upon Timings

Once all the corrections ⟨DELTT2⟩ and ⟨FACTP2⟩ as functions of TDMEAS and $\log_{10}$(P1MEAS/P2MEAS) have been found, they can be put back into the data and compared with the pulse size independent corrections which are in fact nothing more than shifts in DELTT2 and FACTP2. Figures 8.13 show the effect of the corrections to the timings of the second pulses for measured separations between 40 and 50 ns. The corrections are implicitly included within T2MEAS. One very clear characteristic of these distributions is the long tail for the negative values of T2REAL−T2MEAS

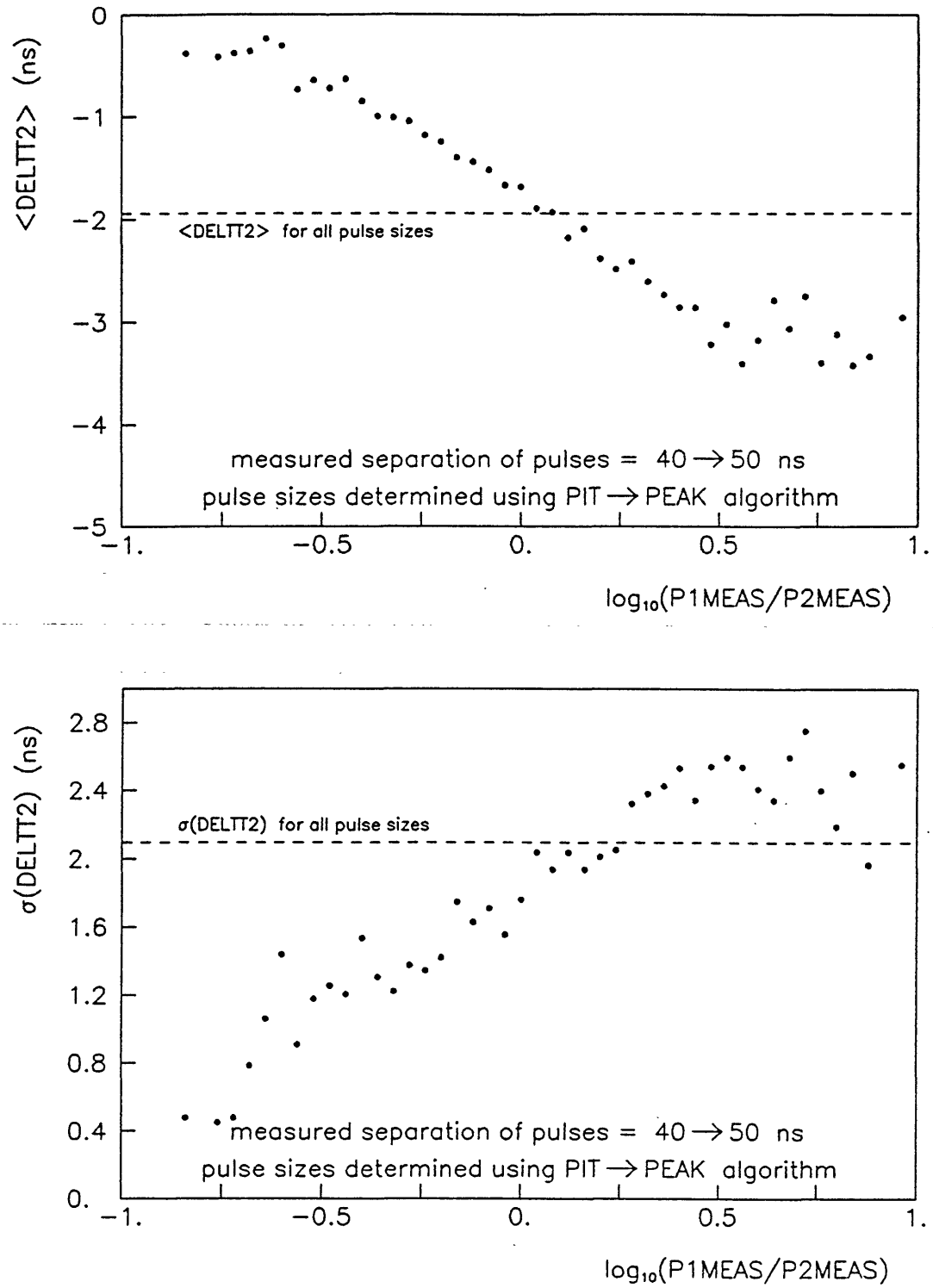


Figure 8.8: *Distributions in ⟨DELTT2⟩ and σ(DELTT2) as a function of log_{10}(P1MEAS/P2MEAS) for measured pulse separations between 40 and 50 ns using the PIT→PEAK algorithm to measure pulse sizes.*

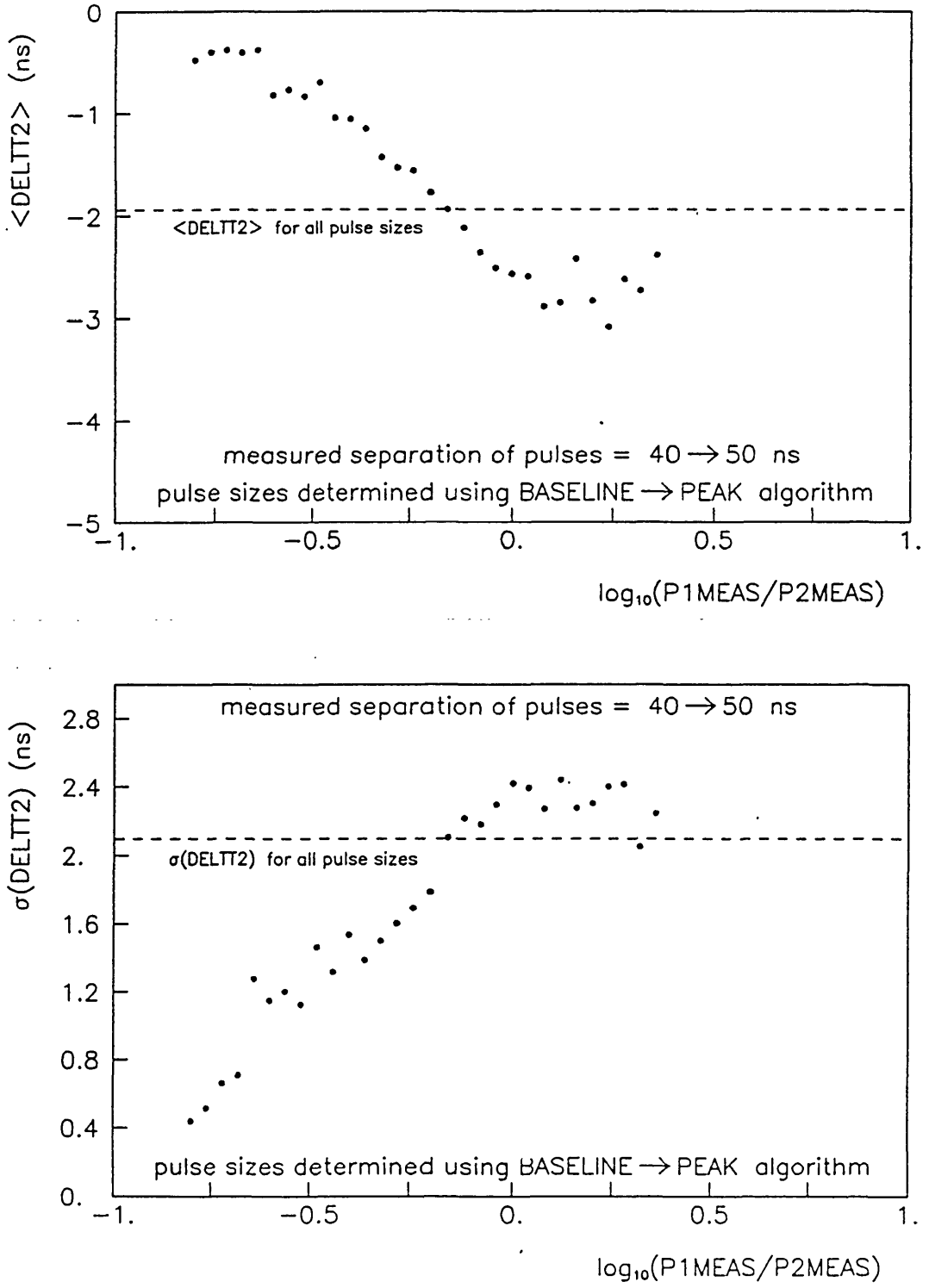


Figure 8.9: *Distributions in ⟨DELTT2⟩ and σ(DELTT2) as a function of log_{10}(P1MEAS/P2MEAS) for measured pulse separations between 40 and 50 ns using the BASELINE→PEAK algorithm to measure pulse sizes.*

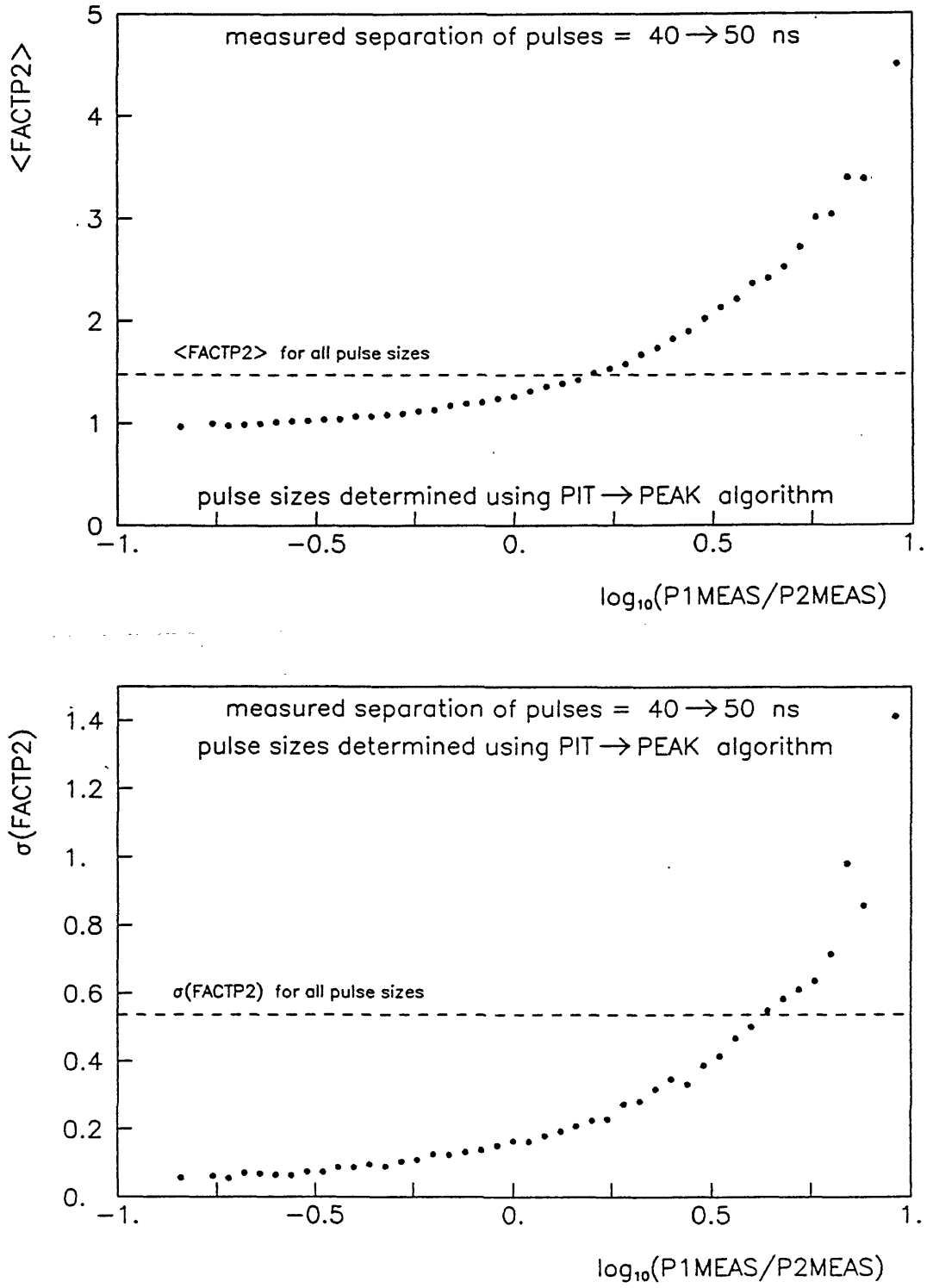


Figure 8.10: *Distributions in ⟨FACTP2⟩ and σ(FACTP2) as a function of log_{10}(P1MEAS/P2MEAS) for measured pulse separations between 40 and 50 ns using the PIT→PEAK algorithm to measure pulse sizes.*

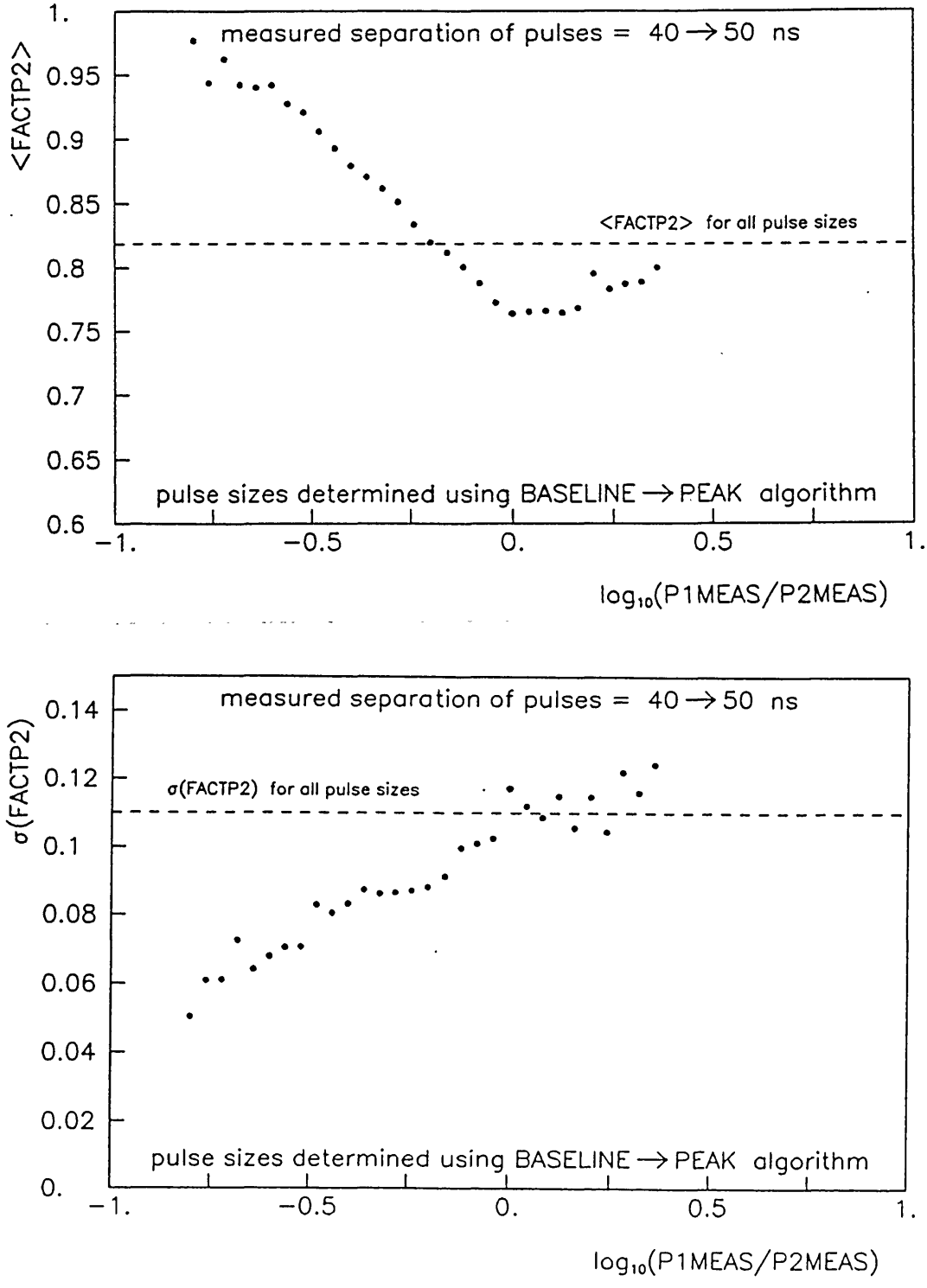


Figure 8.11: *Distributions in ⟨FACTP2⟩ and σ(FACTP2) as a function of log_{10}(P1MEAS/P2MEAS) for measured pulse separations between 40 and 50 ns using the BASELINE→PEAK algorithm to measure pulse sizes.*

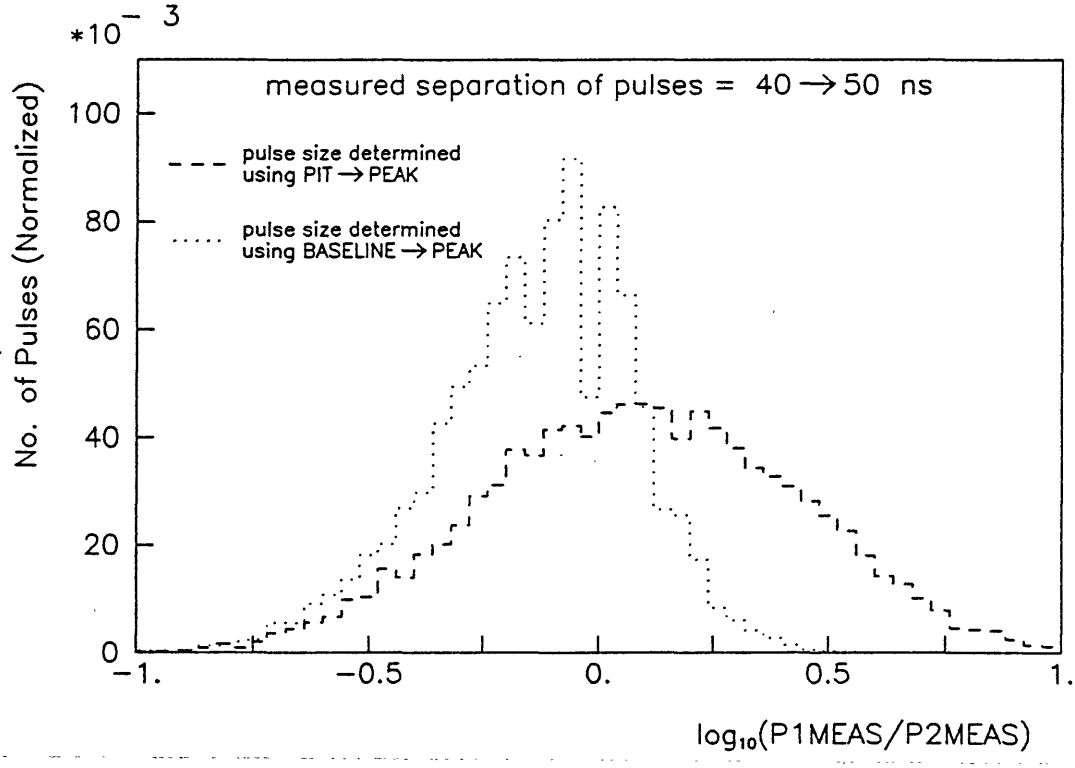


Figure 8.12: *Frequency distributions in the measured relative pulse sizes for the PIT→PEAK and BASELINE→PEAK pulse size algorithms for pulse separations of between 40 and 50 ns.*

which the pulse size dependent corrections have not been able to remove. Also it can be seen that the pulse size dependent corrections have had almost no effect in reducing the overall width of this distribution. This tail gets less prominent the larger the pulse separations become but for each series of pulse separations the pulse size dependent corrections had no effect in reducing the size of the tail. This suggests that the inclusion of the relative pulse sizes in the corrections to the timings is of no benefit.

This is shown to be the case in figure 8.14 where the widths of T2REAL−T2MEAS or DELTT2 are plotted, as a function of the measured pulse separations, for the data without corrections and with the pulse size dependent corrections using the PIT→PEAK and BASELINE→PEAK algorithms. From this we can see that the corrections have indeed had almost no effect in reducing the widths in the distribution of DELTT2, the difference in the times of the second pulse when a single pulse and when affected by the first pulse. This is finally shown by finding the spatial resolutions from the hit positions whose timings we have corrected. The resulting spatial resolutions as a function of the real pulse separation is shown in figure 8.15 which appears to follow the overall shape of figure 8.14. This is not unexpected as the spatial resolution of the second pulse should

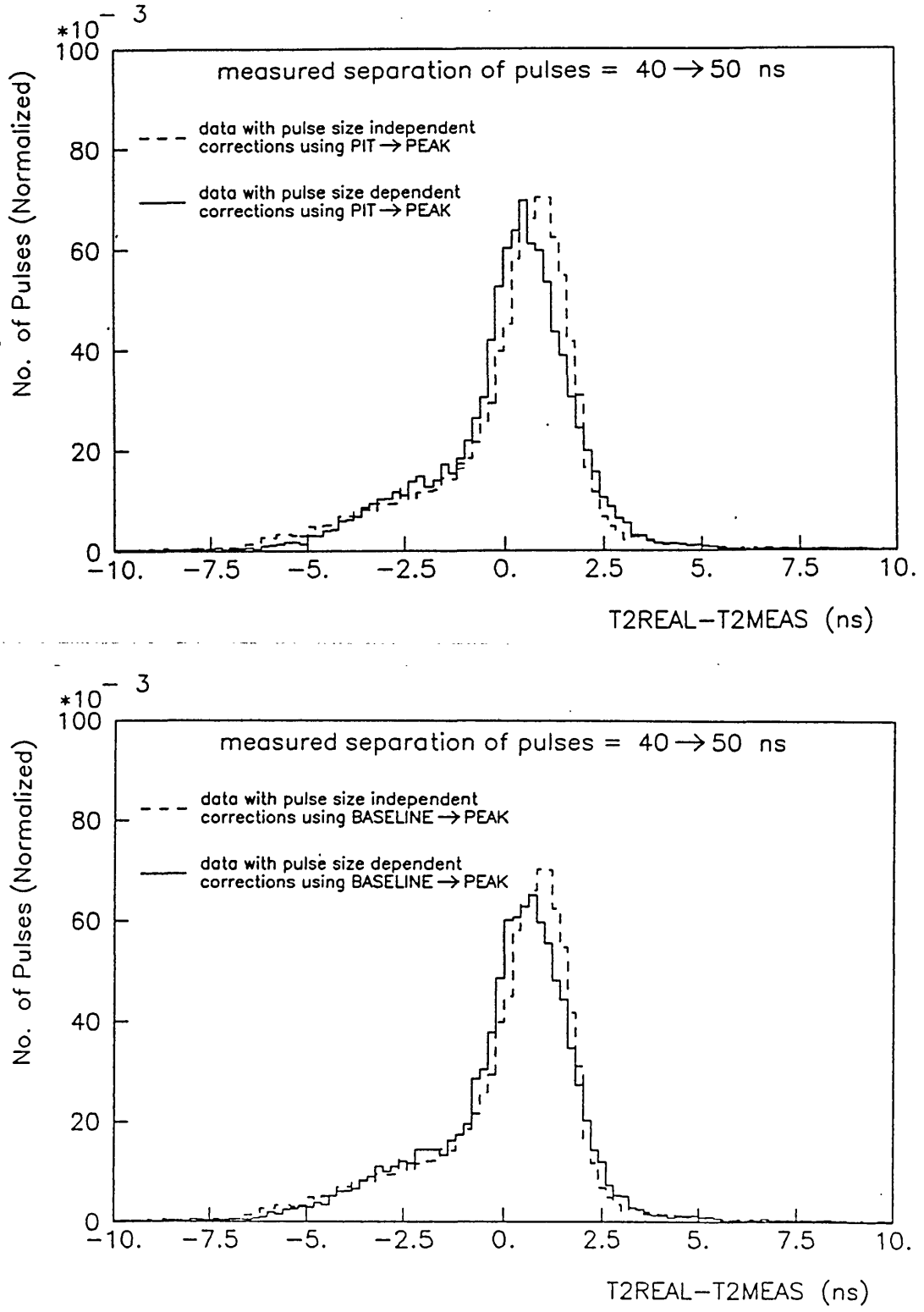


Figure 8.13: *Distributions in T2REAL−T2MEAS with corrections using the PIT→PEAK and BASELINE→PEAK algorithms to determine pulse sizes for measured pulse separations between 40 and 50 ns.*

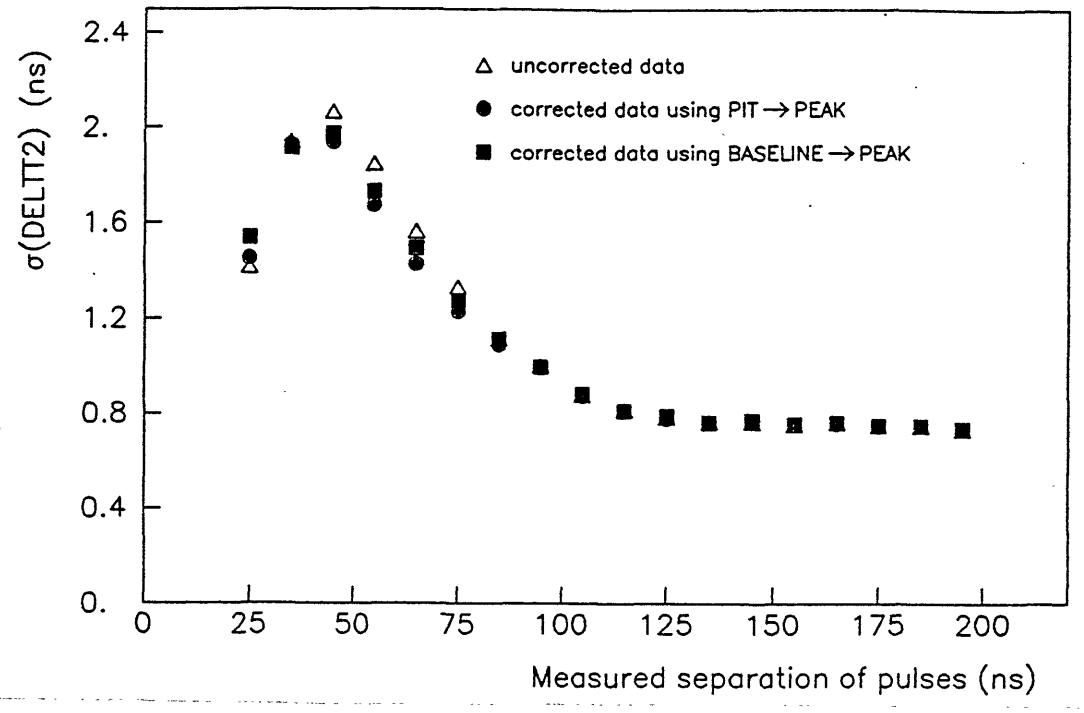


Figure 8.14: *Distribution of σ(DELTT2) as a function of measured pulse separation for both uncorrected and corrected data.*

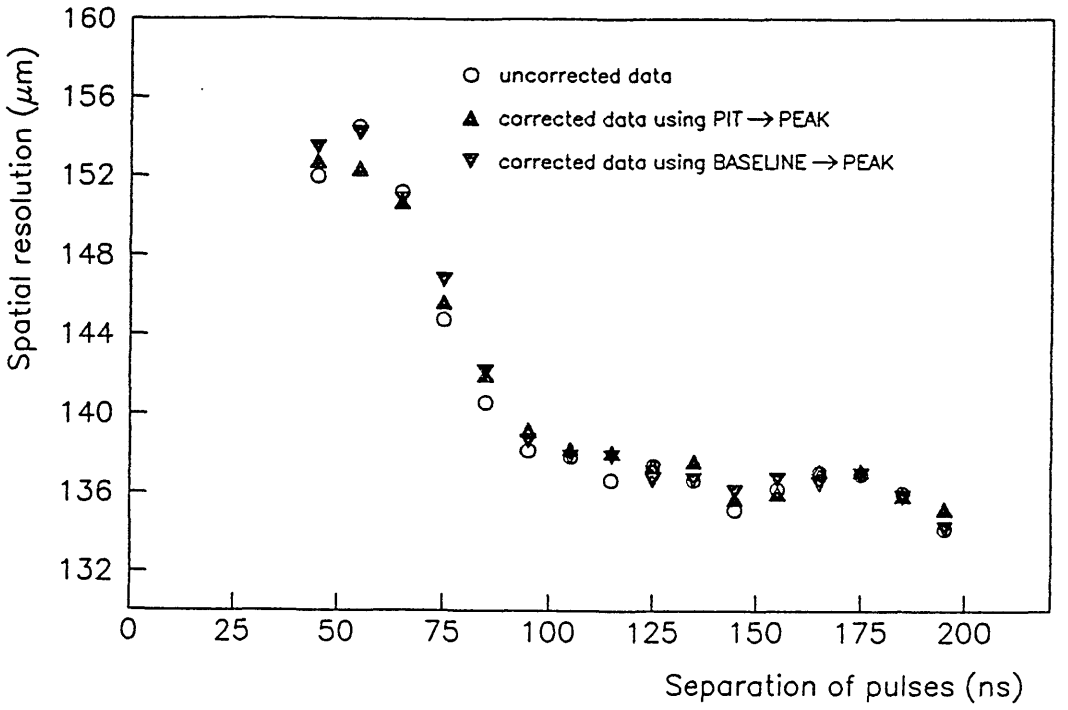


Figure 8.15: *Effect of corrections upon the second pulse spatial resolution.*

follow the underlying pattern of uncertainty in the measurement of its time.

To see whether it was the overall behaviour of the pulses that caused the pulse size dependent corrections to be ineffective or whether it was a wrong choice in the parameterization of the pulse size corrections, the analysis was repeated using the pulse size correction ⟨DELTP2⟩ where

$$\text{DELTP2} = \text{P2REAL} - \text{P2MEAS} \tag{8.4}$$

with both ⟨DELTT2⟩ and ⟨DELTP2⟩ becoming functions of P1MEAS−P2MEAS. After finding the new corrections and including them in the data, we found that the distribution of σ(DELTT2) was almost the same regardless of whether FACTP2 or DELTP2 had been used to determine the corrections. This is shown in figure 8.16. The conclusion to be made from this is that pulse size dependent corrections do not appear to reduce the error in the timings of the second pulses when they are affected by the first pulses.

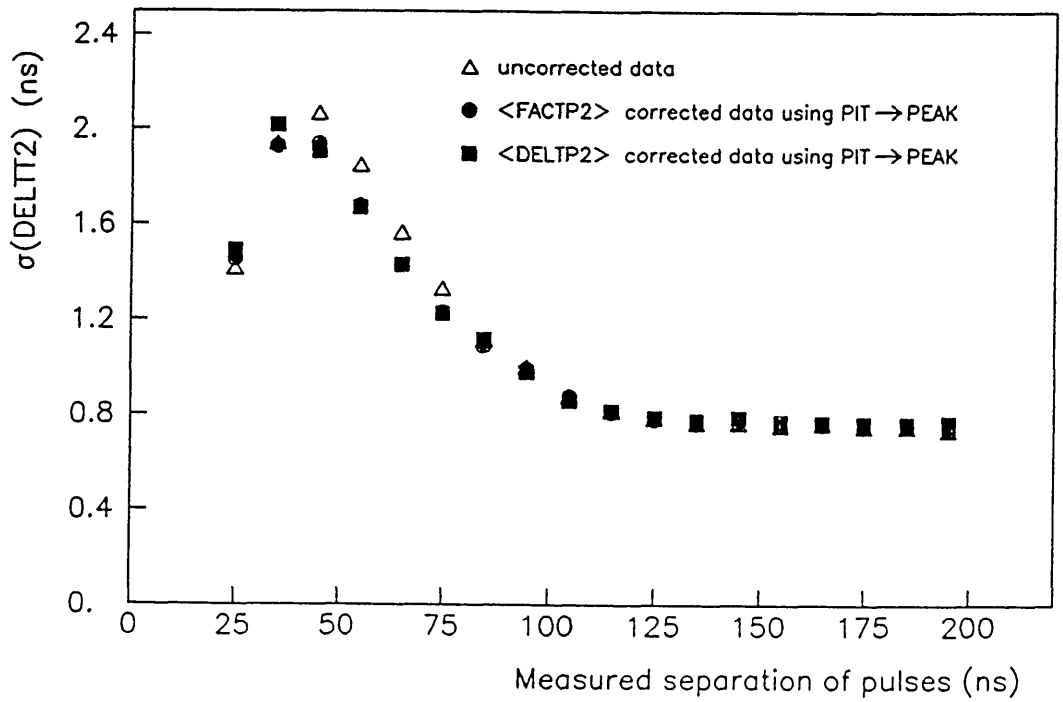


Figure 8.16: *Distribution of σ(DELTT2) with corrections using FACTP2 and DELTP2 parameterizations.*

8.5.3 Effect of Corrections upon Pulse Sizes

Figures 8.17 show the effect of including in the corrections on the sizes of pulses in the data, with measured separations between 40 and 50 ns. With the PIT→PEAK algorithm we find a vast improvement with the distribution becoming symmetrical and much narrower whilst for the BASELINE→PEAK algorithm it merely appears to remove the quantization effect that is caused by the 6-bit to 8-bit conversion. Plotting the σ(FACTP2) distribution as a function of the measured pulse separation as shown in figure 8.18, we can see the improvement made by the corrections when using the PIT→PEAK algorithm. Any improvement for the BASELINE→PEAK algorithm is not so pronounced. It appears, however, that for nearly all of the pulse separation range where the second pulse is clearly affected by the first, both the uncorrected and corrected BASELINE→PEAK data appear to perform better than the corrected PIT→PEAK data as the σ(FACTP2) values are smaller. This suggests that the BASELINE→PEAK algorithm could be the better one to use when determining pulse sizes. Once again due to the limited statistics available in finding the dE/dx resolution, it is difficult to ascertain which algorithm performs better for the second pulse when referring to the dE/dx resolution distribution. This is shown in figure 8.19 where both the corrected and uncorrected data are plotted.

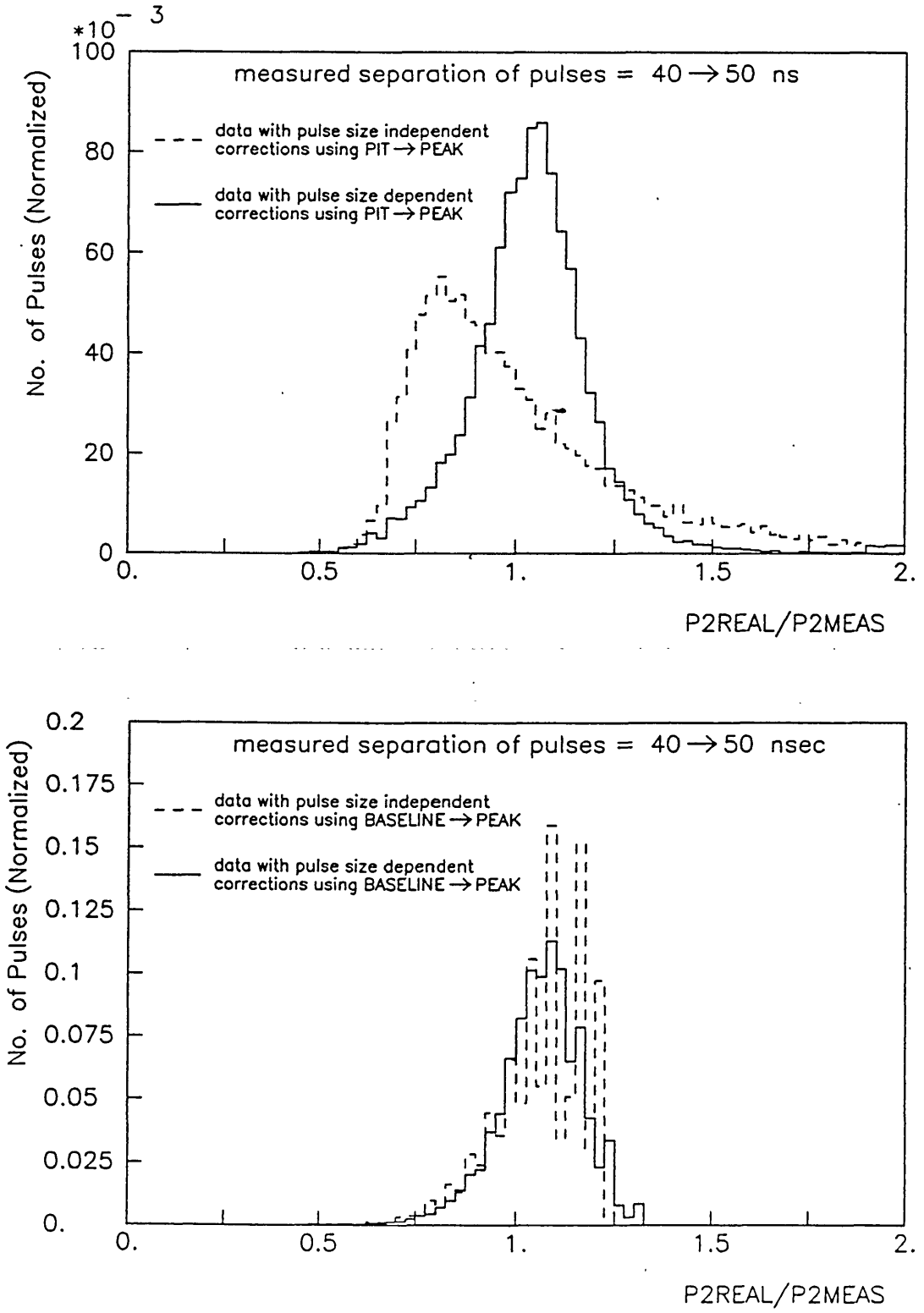


Figure 8.17: *Distributions in P2REAL/P2MEAS with corrections using the PIT→PEAK and BASELINE→PEAK algorithms to determine pulse sizes for measured pulse separations between 40 and 50 ns.*

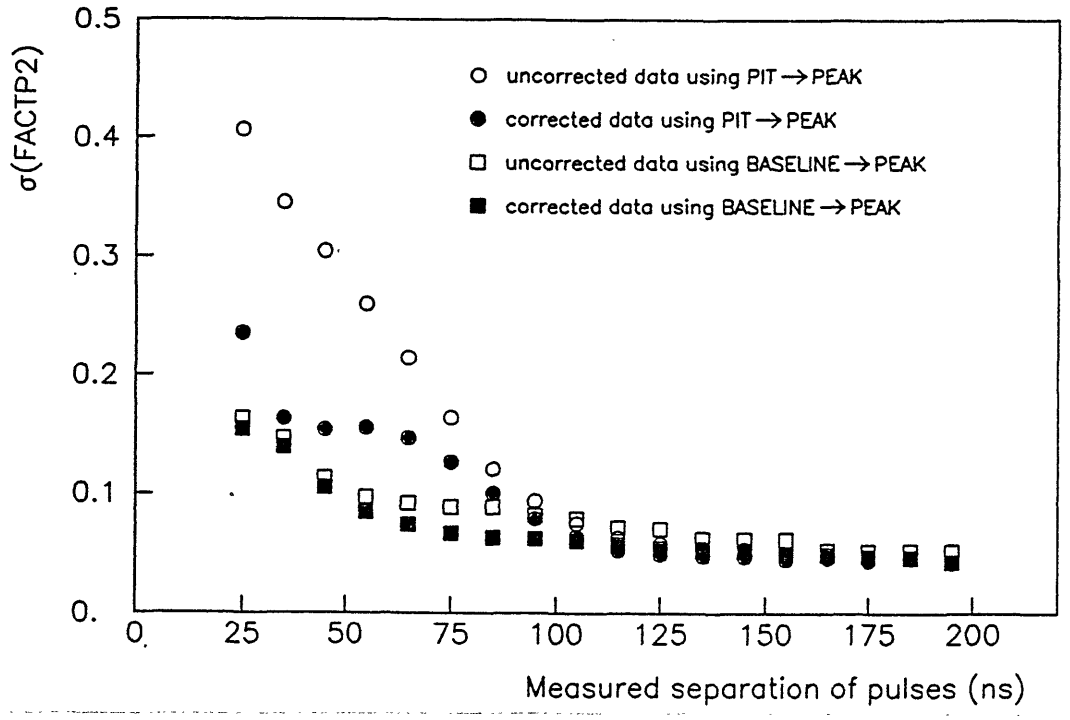


Figure 8.18: *Distribution of σ(FACTP2) as a function of measured pulse separation for both uncorrected and corrected data.*

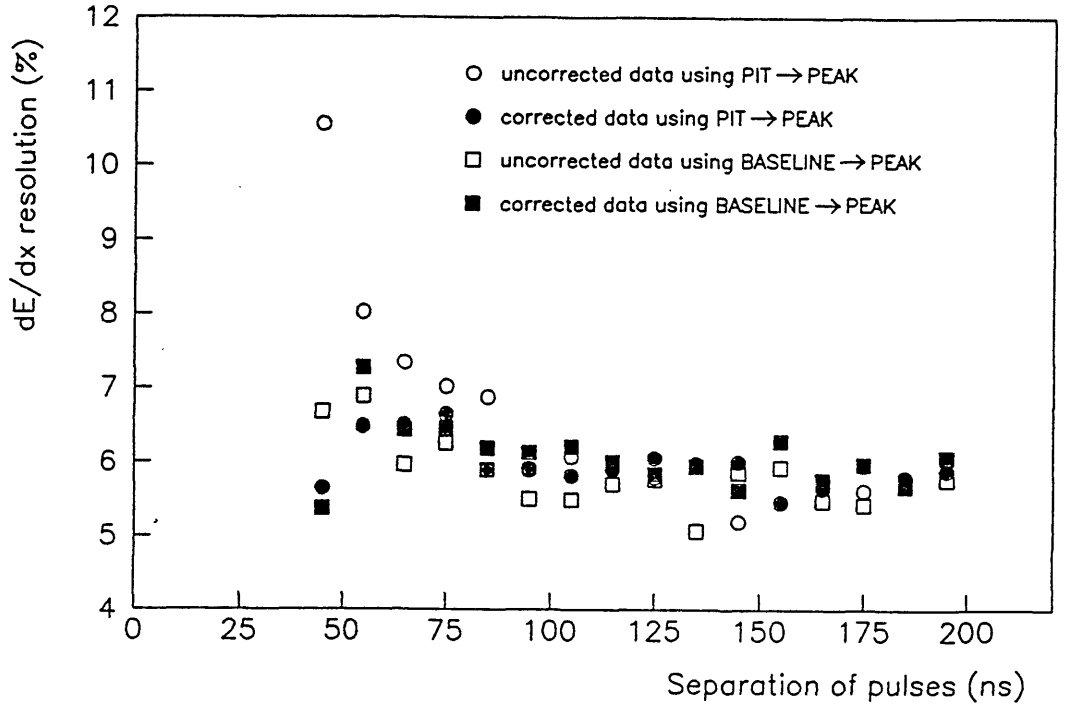


Figure 8.19: *Effect of corrections upon the second pulse dE/dx resolution.*

8.6 Conclusions to Multi-Pulse Analysis

From the study made on the multi-pulse performance of the chamber we find that by using pole-zero filters we can obtain a two-pulse resolution of 2.15 mm. We also find that the first or preceding pulse is not seriously affected by the second or preceded pulse for pulse separations greater than 75 ns or 3.75 mm. Any effect of the first pulse upon the second was negligible for pulse separations larger than 105 ns or 5.25 mm. These results are with respect to both timings and pulse size measurements if a single bin measurement of the pulse height is used to determine the pulse size. The worse spatial resolution found for the first or preceding pulse is about 60% larger than the single pulse resolution and for the second or preceded pulse it is only 15% above that of the single pulse. After correcting the pulse size, the dE/dx resolution for the second pulse does not rise above 7%, and remains around 6% for most of the pulse separation range where the second pulse is affected by the first. This 6% dE/dx resolution is the value found for the first pulse regardless of the pulse separation and is better than the 7.5% requirement for the CTD stated in reference [47].

Appendix A

TASSO Track Parameters

The TASSO co-ordinate system was defined as having the origin at the centre of the drift chamber. The x axis was in the horizontal direction pointing towards the centre of PETRA, the y axis was vertically upwards and the z axis was along the direction of the positron beam. In a cylindrical co-ordinate system the $r-\phi$ plane was perpendicular to the beam. The path length along a track in $r-\phi$ was defined as s so that the $s-z$ plane contained both the track straightened out in $r-\phi$ and the z axis.

The definitions of the main track parameters shown in fig A.1 were:

R	Track radius in the $r-\phi$ plane.
x_0, y_0	Co-ordinates of the point in $r-\phi$ plane where track was closest to the origin.
x_c, y_c	Co-ordinates of the point in $r-\phi$ plane that corresponds to the centre of the track circle.
ϕ_0	Angle of track in the $r-\phi$ plane at (x_0, y_0).
d_0	Distance of closest approach of track to origin in the $r-\phi$ plane. For tracks that enclosed the origin $d_0 \geq 0$ else $d_0 < 0$.
z_0	Intercept of track with z axis in the $s-z$ plane.
θ	Angle of track to z axis in the $s-z$ plane.
λ	Angle of track to $r-\phi$ plane in the $s-z$ plane.

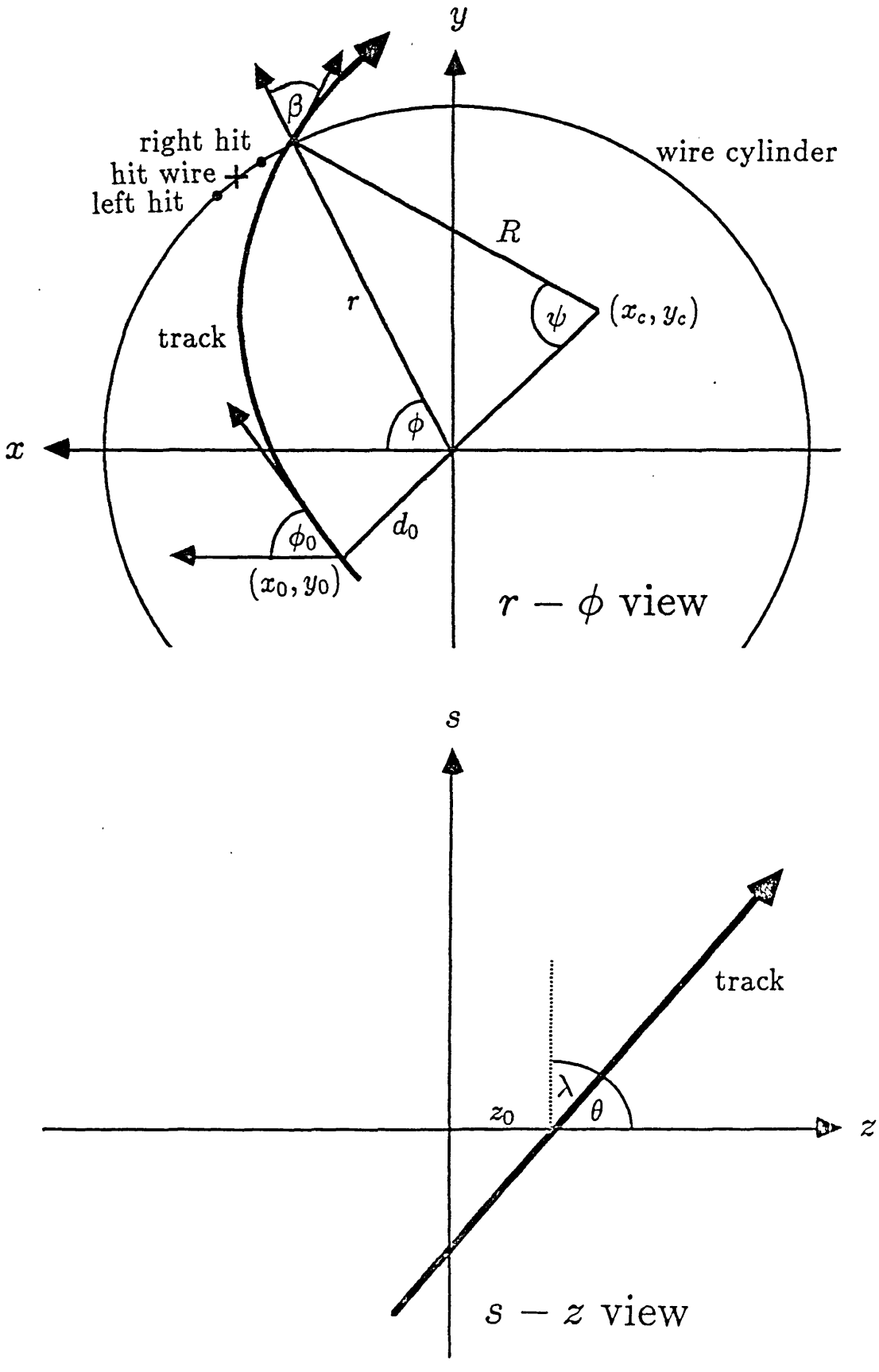


Figure A.1: *TASSO track parameters*

Appendix B

Calculating Hits for Track Finding

Hits are initially input into track finders as addresses and measured drift times for hit wires. Each time is converted to a drift distance, by multiplying by the drift velocity. This drift distance is assumed to be an arc length on the wire circle, the circle being at $z = 0$ for stereo wires, and the angles ϕ_l and ϕ_r are calculated for the two possible hit positions either side of the wire.

B.1 Hits in the $r - \phi$ Plane

The first stage of track finding uses only the DC0 hits, resulting in the projection of the track onto the $r - \phi$ plane. The magnetic field was uniform enough to assume the projected track is a circle.

In terms of the track parameters described in appendix A, ϕ is given by

$$\phi = \phi_0 + Q \arcsin\left(\frac{2Rd_0 - d_0^2 - r^2}{2r\,(R - d_0)}\right) \tag{B.1}$$

where Q is the charge of the track. The drift distance calculated using just the drift velocity is only approximate, the real drift distance depending on the angle β between the normal to the wire cylinder and track direction at that point, as well as the drift time. β is given by

$$\beta = \arcsin\left(\frac{r^2 + 2Rd_0 - d_0^2}{2rR}\right) \tag{B.2}$$

After a track has been found with the DC0 wires, the drift distances are corrected using polynomials determined in an iterative procedure. A best fit track is then calculated from hits with the corrected drift distances.

B.2 Hits in the $s - z$ Plane

Once the track in the $r - \phi$ projection has been found, hits in the $s - z$ plane can be searched for. The projection of the track on the $r - \phi$ plane defines a cylinder and the $s - z$ hit, if it belongs to this track, lies on this cylinder. The angle β for the track in the stereo layer is calculated from the layer radius at $z = 0$. The fully corrected drift distance for each hit wire is used to determine ϕ_s for the left and right hits at $z = 0$. For a layer with stereo angle α to the z axis and radius r_s at $z = 0$ the hit at (x_s, y_s) has to lie on the line

$$\begin{aligned} x &= x_s - \tan\alpha \sin\phi_s z \\ y &= y_s + \tan\alpha \cos\phi_s z \end{aligned} \tag{B.3}$$

The position of the hit in space, if belonging to the track, has to be the intersection of the line given by equations B.3 with the cylinder given by

$$(x - x_c)^2 + (y - y_c)^2 - R^2 = 0 \tag{B.4}$$

The z co-ordinate of the intersection is

$$z = \frac{-2c}{b + \sqrt{b^2 - 4ac}} \tag{B.5}$$

where

$$\begin{aligned} a &= \tan^2\alpha \\ b &= 2x_c \tan\alpha \sin\phi_s - 2y_c \tan\alpha \cos\phi_s \\ c &= (x_s - x_c)^2 + (y_s - y_c)^2 - R^2 \end{aligned} \tag{B.6}$$

and the s co-ordinate is

$$s = 2R \arcsin\left(\sqrt{\frac{r^2 - d_0^2}{4R(R - d_0)}}\right) \tag{B.7}$$

where r is determined using equations B.5 and B.3. This is repeated for all hits on all stereo wires that intersect the track cylinder, giving a set of hits in the $s - z$ plane. A search for the $s - z$ projection of the track is then made using either a linear fit to the hits, as in the case of non-magnetic particles or, as in our case, a parabolic fit.

Bibliography

[1] TASSO Collaboration, W. Braunschweig *et al.*, Z. Phys. **C38**, (1988) 543

[2] P. A. M. Dirac, Proc. Roy. Soc. **A133**, (1931) 60

[3] P. A. M. Dirac, Phys. Rev. **74**, (1948) 817

[4] J. Schwinger, Science **165**, (1969) 757

[5] H. Georgi and S. L. Glashow, Phys. Rev. Lett. **32**, (1974) 438
For a summary see J. Preskill, Ann. Rev. Nucl. Part. Sci. **34**, (1984) 461

[6] W. Troost and P. Vinciarelli, CERN Th. 2195 (1976) (unpublished)

[7] B. Cabrera, Phys. Rev. Lett. **48**, (1982) 1378

[8] A. D. Caplin *et al.*, Nature **321**, (1986) 402

[9] B. Cabrera *et al.*, Phys. Rev. Lett. **51**, (1983) 1933

[10] G. Giacomelli *et al.*, Nuovo Cim. **A28**, (1975) 21

[11] D. Fryberger, K. Kinoshita and P. B. Price, Phys. Rev. **D29**, (1984) 1524

[12] P. Musset, M. Price and E. Lohrmann, Phys. Lett. **128B**, (1983) 333

[13] P. B. Price and M. H. Salamon, Phys. Rev. Lett. **56**, (1986) 1226

[14] E. Amaldi *et al.*, Nuovo Cim. **A28**, (1963) 773

[15] CLEO Collaboration, T. Gentile *et al.*, Phys. Rev. **D35**, (1987) 1081

[16] G. Barbiellini *et al.*, DESY 80-42, (1980)

[17] S. P. Ahlen, Phys. Rev. **D17**, (1978) 229; Rev. Mod. Phys. **52**, (1980) 121

[18] TASSO Collaboration, M. Altoff *et al.*, Phys. Lett. **138B**, (1984) 441

[19] A. Jocksch *et al.*, Internal TASSO Note 298 (1984) (unpublished)

[20] TASSO Collaboration, R. Brandelik *et al.*, Phys. Lett. **83B**, (1979) 261

[21] H. Burkhardt *et al.*, Nucl. Inst. & Meth. **184**, (1981) 319

[22] K. W. Bell *et al.*, Nucl. Inst. & Meth. **179**, (1981) 27

[23] TASSO Collaboration, R. Brandelik *et al.*, Phys. Lett. **92B**, (1980) 199

[24] TASSO Collaboration, R. Brandelik *et al.*, Phys. Lett. **94B**, (1980) 259

[25] D. M. Binnie *et al.*, Nucl. Inst. & Meth. **228**, (1985) 267

[26] C. Youngman, Ph.D. Thesis, Imperial College **HEP/T/82**, (1980)

[27] A. J. Campbell, Ph.D. Thesis, Imperial College **HEP/T/117**, (1983)

[28] H. Boerner *et al.*, Nucl. Inst. & Meth. **176**, (1980) 151

[29] J. K. Sedgbeer, Ph.D. Thesis, Imperial College **HEP/T/116**, (1983)

[30] TASSO Collaboration, R. Brandelik *et al.*, Phys. Lett. **94B**, (1980) 444

[31] H. M. Fischer and N. Wermes, DESY Internal Report F12-80/01, (1980)

[32] C. M. Hawkes, Ph.D. Thesis, Oxford University **RAL/T/011**, (1985)

[33] D. G. Cassel and H. Kowalski, Nucl. Instr. & Meth. **185**, (1981) 235

[34] T. Gilead *et al.*, Internal TASSO Note 60 (1978) (unpublished)

[35] U. Fano, Ann. Rev. Nucl. Sci. **13**, (1963) 1

[36] Review of Particle Properties, Phys. Lett. **B170**, (1986)

[37] B. Naroska, DESY 86-113, (1986)

[38] D.H. Perkins, Introduction to High Energy Physics, Addison Wesley (1982)

[39] Y. Kazama, C. N. Yang and A. S. Goldhaber, Phys Rev. **D15**, (1977) 2287

[40] Original technical drawings of CPC (not published)

[41] X. S. Tsai, Rev. Mod. Phys. **46**, (1974) 815

[42] TASSO Collaboration, W. Braunschweig *et al.*, DESY 88-034, (1988)

[43] T. Bowcock and D. Xiao, Private communication.

[44] Nijenhuis and Wilf, Combinatorial Algorithms, Acedemic Press (1978)

[45] F. Sauli, CERN 77-09, (1977)

[46] G. Wolf, DESY 86-089, (1986)

[47] The ZEUS detector, Technical Proposal, ZEUS collaboration, (1986)

[48] The ZEUS detector, Status Report 1987, ZEUS collaboration, PRC 87-02, (1987)

[49] Technical Proposal for the H1 Detector, H1 collaboration, (1986)

[50] SYSTEM DL300 (Heidelberg), B Struck, Tangstedt/Hamburg (unpublished)

[51] G. Eckerlin *et al.*, IEEE Trans. Nucl. Sci. **NS-33**, (1986) 1066

[52] M. Atac, LBL-21170, (1986) 55

[53] B. I. Hallgren and M. Verweij, IEEE Trans. Nucl. Sci. **NS-27**, (1980) 253

[54] S. M. Tkaczyk *et al.*, RAL-87-094, (1987)

[55] D. Schaile *et al.*, Nucl. Instr. Meth. **A242**, (1986) 247